

LeMMINGs. VI. Connecting nuclear activity to bulge properties of active and inactive galaxies: radio scaling relations and galaxy environment

B. T. Dullo¹,^{1*} J. H. Knapen,^{2,3} R. J. Beswick,⁴ R. D. Baldi^{5,6}, D. R. A. Williams^{7,4}, I. M. McHardy,⁶ D. A. Green⁷, A. Gil de Paz^{8,1}, S. Aalto,⁸ A. Alberdi,⁹ M. K. Argo¹⁰, H.-R. Klöckner,¹¹ I. M. Mutie^{12,4,12}, D. J. Saikia,¹³ P. Saikia¹⁴ and I. R. Stevens¹⁵

¹Departamento de Física de la Tierra y Astrofísica, IPARCOS, Universidad Complutense de Madrid, E-28040 Madrid, Spain

²Instituto de Astrofísica de Canarias, Vía Láctea S/N, E-38205 La Laguna, Tenerife, Spain

³Departamento de Astrofísica, Universidad de La Laguna, E-38206 La Laguna, Tenerife, Spain

⁴Jodrell Bank Centre for Astrophysics, School of Physics and Astronomy, The University of Manchester, Alan Turing Building, Oxford Road, Manchester M13 9PL, UK

⁵Istituto di Radioastronomia – INAF, Via P. Gobetti 101, I-40129 Bologna, Italy

⁶School of Physics and Astronomy, University of Southampton, Southampton SO17 1BJ, UK

⁷Astrophysics Group, Cavendish Laboratory, 19 J. J. Thomson Avenue, Cambridge CB3 0HE, UK

⁸Department of Space, Earth and Environment, Chalmers University of Technology, SE-412 96 Göteborg, Sweden

⁹Instituto de Astrofísica de Andalucía, IAA-CSIC, Glorieta de la Astronomía s/n, E-18008 Granada, Spain

¹⁰Jeremiah Horrocks Institute, University of Central Lancashire, Preston, Lancashire PR1 2HE, UK

¹¹Max-Planck-Institut für Radioastronomie, Auf dem Hügel 69, D-53121 Bonn, Germany

¹²Technical University of Kenya, P.O. box 52428-00200 Nairobi, Kenya

¹³Inter-University Centre for Astronomy and Astrophysics (IUCAA), P.O., Post Bag 4, Ganeshkhind, Pune 411 007, India

¹⁴Center for Astro, Particle and Planetary Physics, New York University Abu Dhabi, PO Box 129188 Abu Dhabi, UAE

¹⁵School of Physics and Astronomy, University of Birmingham, Birmingham B15 2TT, UK

Accepted 2023 April 12. Received 2023 April 12; in original form 2022 August 3

ABSTRACT

Multiwavelength studies indicate that nuclear activity and bulge properties are closely related, but the details remain unclear. To study this further, we combine *Hubble Space Telescope* bulge structural and photometric properties with 1.5 GHz, *e*-MERLIN nuclear radio continuum data from the LeMMINGs survey for a large sample of 173 ‘active’ galaxies (LINERs and Seyferts) and ‘inactive’ galaxies (H II s and absorption line galaxies, ALGs). Dividing our sample into active and inactive, they define distinct (radio core luminosity)–(bulge mass), $L_{R,\text{core}} - M_{*,\text{bulge}}$, relations, with a mass turnover at $M_{*,\text{bulge}} \sim 10^{9.8 \pm 0.3} M_{\odot}$ (supermassive blackhole mass $M_{\text{BH}} \sim 10^{6.8 \pm 0.3} M_{\odot}$), which marks the transition from AGN-dominated nuclear radio emission in more massive bulges to that mainly driven by stellar processes in low-mass bulges. None of our 10/173 bulge-less galaxies host an AGN. The AGN fraction increases with increasing $M_{*,\text{bulge}}$ such that $f_{\text{optical_AGN}} \propto M_{*,\text{bulge}}^{0.24 \pm 0.06}$ and $f_{\text{radio_AGN}} \propto M_{*,\text{bulge}}^{0.24 \pm 0.05}$. Between $M_{*,\text{bulge}} \sim 10^{8.5}$ and $10^{11.3} M_{\odot}$, $f_{\text{optical_AGN}}$ steadily rises from 15 ± 4 to 80 ± 5 per cent. We find that at fixed bulge mass, the radio loudness, nuclear radio activity, and the (optical and radio) AGN fraction exhibit no dependence on environment. Radio-loud hosts preferentially possess an early-type morphology than radio-quiet hosts, the two types are however indistinguishable in terms of bulge Sérsic index and ellipticity, while results on the bulge inner logarithmic profile slope are inconclusive. We finally discuss the importance of bulge mass in determining the AGN triggering processes, including potential implications for the nuclear radio emission in nearby galaxies.

Key words: galaxies: active – galaxies: elliptical and lenticular, cD – galaxies: nuclei – galaxies: photometry – galaxies: structure – radio continuum: galaxies.

1 INTRODUCTION

All present-day massive galaxies host a supermassive blackhole (SMBH) at their centre (Magorrian et al. 1998; Richstone et al. 1998; Ferrarese & Ford 2005). Theoretical models predict that feedback

from an accreting SMBH (i.e. active galactic nucleus, AGN), through mechanisms such as radiation pressure or radio jets (e.g. Heckman & Best 2014), injects energy and momentum, which heat or expel the surrounding gas and suppress star formation in the galaxy bulge¹

¹Traditionally the term ‘bulge’ is associated with the spheroidal component of disc galaxies but it is used here to refer to the underlying host spheroid in

* E-mail: bdullo@ucm.es

component (Silk & Rees 1998; Croton et al. 2006; Hopkins et al. 2006; King & Pounds 2015; Weinberger et al. 2017). This AGN self-regulated mechanism, where the gas removal by the feedback shuts off the AGN itself, leads to the concurrent growth of the SMBH and its host bulge and thus naturally explains the tight correlations observed between SMBH mass (M_{BH}) and the velocity dispersion of bulges (Ferrarese & Merritt 2000; Gebhardt et al. 2000) and the luminosity and stellar and dynamical masses of bulges (Kormendy & Richstone 1995; Magorrian et al. 1998; McLure & Dunlop 2002; Marconi & Hunt 2003; Häring & Rix 2004). AGN feedback is also believed to rapidly drive galaxy colour evolution from blue to red (e.g. Cattaneo et al. 2006; Faber et al. 2007; Schawinski et al. 2010; Dullo et al. 2020). While the evolution of the SMBH and its host bulge appear intertwined (e.g. Silk & Rees 1998; Kauffmann & Haehnelt 2000), the details of the regulatory role of the AGN in building up the bulge stellar mass and in shaping the stellar distributions of local bulges are unclear.

Models of galaxy formation based on Λ cold dark matter (Λ CDM) predict that massive local bulges have assembled hierarchically through galaxy mergers (e.g. Toomre & Toomre 1972; White & Rees 1978; Blumenthal et al. 1984; White & Frenk 1991). Gravitational torques from the mergers convert discs into bulges and funnel large amounts of gas into galaxy centres (Hernquist 1989; Barnes & Hernquist 1991, 1996). This process is hypothesized to result in growth of the SMBH, AGN activity, and nuclear starburst events, and thus a centrally concentrated bulge. On the other hand, low mass bulges, which are commonly associated with spiral and irregular galaxies, may be consequences of dissipational collapse of accreted gas within dark matter haloes (Fall & Efstathiou 1980). This initial assembly is accompanied by redistribution of their disc material through secular evolution (e.g. Kormendy 1982, 1993), which feeds the central SMBH and triggers AGN activity (e.g. Shlosman, Frank & Begelman 1989; Knapen et al. 1995; Hopkins & Quataert 2011; Galloway et al. 2015; Lin et al. 2020; Anglés-Alcázar et al. 2021).

Galaxy mergers, episodes of vigorous star formation, and SMBH growth are thought to be common at higher redshift ($z \sim 2.0 \pm 0.5$; Förster Schreiber et al. 2014; Madau & Dickinson 2014). The scaled-down analogies of these processes which are observed in nearby galaxies may hold crucial clues into the build up of the bulge's stellar mass and AGN triggering mechanisms: i.e. gas-rich or gas-poor mergers (e.g. Urrutia, Lacy & Becker 2008; Gao et al. 2020) and secular evolution (e.g. Cisternas et al. 2011; Kormendy & Ho 2013). Nearby galaxies commonly possess low-luminosity AGN (LLAGN), defined to have $H\alpha$ luminosity $L_{H\alpha} \lesssim 10^{40} \text{ erg s}^{-1}$ (Ho, Filippenko & Sargent 1997a, b, c). These are weaker than the powerful AGN which manifest themselves as bright Seyfert galaxies (Seyfert 1943) and quasars (Merloni & Heinz 2008). LLAGN include low-luminosity Seyferts and Low-Ionization Nuclear Emission Line regions (LINERs; Heckman 1980), which generally display AGN-driven nuclear activity (Ferland & Netzer 1983), but the latter could be powered by shocks (Dopita & Sutherland 1995) and photoionization from hot stars (Sarzi et al. 2010; Singh et al. 2013). Aside from LINERs and Seyferts, galaxies may either harbour $H\text{II}$ nuclei or be an absorption-line galaxy (ALG). $H\text{II}$ nuclei are swamped with star formation events, which dominate the nuclear ionization processes, whereas the ALG nuclei lack distinctive emission lines, none the less both spectral classes may contain LLAGN nuclei in the form of a weakly accreting SMBH (Ho 2008; Heckman & Best 2014). While LLAGN

represent the most common type of AGN in the local Universe (Filho, Barthel & Ho 2006; Ho 2008), they have largely been overlooked in previous radio studies due in part to the weak radio emission from the SMBHs, which is particularly true for those hosted by late-type galaxies. Radio continuum emission provides a dust extinction-free constraint on the star formation and AGN activity in LLAGNs (e.g. Ulvestad & Ho 2001b; Nagar, Falcke & Wilson 2005; Nyland et al. 2016; Baldi et al. 2018; Saikia et al. 2018).

In this work, our primary objective is to utilize multiwavelength observations, optimized for studying relations between the AGN, host bulge properties and environment, for a comprehensive view of the different evolution scenarios for the host galaxies. How well we understand the feedback from the AGN and supernova explosions and stellar winds (e.g. Kaviraj et al. 2011) and the low-level SMBH accretion activities in nearby galaxies (and by extension LLAGNs) depends on how far down the radio and optical luminosity function the data trace (e.g. Heckman & Best 2014; Baldi et al. 2021b). Observations indicate that AGN feedback is a strong function of the bulge mass and morphology for nearby galaxies (e.g. Kauffmann et al. 2003a; Best et al. 2005; Kauffmann, Heckman & Best 2008; Heckman & Best 2014). Radio AGNs are commonly associated with massive early-type galaxies, while they are relatively rare in less massive late-type galaxies (Sandage 1965; Sadler et al. 1995; Nagar et al. 2002; Dunlop et al. 2003; Nagar et al. 2005; Barišić et al. 2017; Baldi et al. 2018, 2021a, b). Saikia, Körding & Falcke (2015) and Baldi et al. (2021b) constructed a scaling relation between the optical [O III] and radio emission for local galaxies, and revealed distinct radio production mechanisms for the different optical classes and SMBH masses; AGN-driven sources dominate above $M_{\text{BH}} \sim 10^{6.5} M_{\odot}$, whereas below this nominal M_{BH} threshold the nuclear radio emission is predominantly from stellar processes associated with non-jetted $H\text{II}$ galaxies.

1.1 Bulge structure, environment, and AGN activity

Past observational studies typically tie radio loudness to the presence of two types of early-type bulges, namely ‘core-Sérsic’ and ‘Sérsic’ (e.g. Faber et al. 1997; Graham et al. 2003; Dullo & Graham 2013, 2014; Dullo 2019; Dullo et al. 2019), with structurally distinct central regions (e.g. Capetti & Balmaverde 2005; de Ruiter et al. 2005; Balmaverde & Capetti 2006; Capetti & Balmaverde 2007; Kormendy et al. 2009; Baldi et al. 2010; Richings, Uttley & Körding 2011; Dullo et al. 2018). Separating core-Sérsic and Sérsic galaxies in the radio scaling relations is important, as depleted cores are thought to be carved out by binary SMBHs during the violent ‘dry’ phase of the galaxy assembly (Begelman, Blandford & Rees 1980; Ebisuzaki, Makino & Okumura 1991; Rantala et al. 2018; Nasim et al. 2020; Dosopoulou, Greene & Ma 2021; Nasim et al. 2021) and the AGN feedback is posited to play a role in the central structural dichotomy of early-type galaxies (e.g. Hopkins et al. 2009a, b). Furthermore, observations on the link between environment and AGN show heating by episodic radio AGN which injects jets from central galaxies into the intracluster medium. This can act to quench a cooling flow in galaxy groups and clusters (McNamara et al. 2009; McNamara, Rohanizadegan & Nulsen 2011; Fabian 2012), reconciling well with the ubiquity of depleted cores in massive galaxies residing in such environments (Laine et al. 2003; Dullo 2019).

Whether AGN activity is environmentally driven is, however, currently under debate. Tidal interactions and mergers of galaxies can trigger the onset of nuclear activity and/or enhance it by funnelling gas to innermost regions of galaxies and subsequently onto the central SMBH (e.g. Sanders et al. 1988; Hernquist 1989; Barnes & Hernquist

case of elliptical galaxies and the spheroidal component for lenticular galaxies (S0s), spiral, and irregular galaxies.

1991; Shlosman 1994). In the nearby Universe, the incidence of AGN has been reported to increase with the local density of the host galaxy (Kauffmann et al. 2004), while others reported a high incidence of AGN in lower density environments (Sabater, Best & Argudo-Fernández 2013; Mishra & Dai 2020) or a lack of significant environmental dependence for the AGN (Miller et al. 2003; Pimbblet et al. 2013; Amiri, Tavasoli & De Zotti 2019; Man et al. 2019). For further evidence in favour of the ‘AGN-density’ relation see Best et al. (2007); Mandelbaum et al. (2009); Gendre et al. (2013); Sabater et al. (2013); Miraghaei & Best (2017); Sabater et al. (2019).

In this work, we combine the results from an *HST* imaging analysis with 1.5 GHz *e*-MERLIN radio data, allowing for a homogenous study of the link between nuclear activity and host bulge properties and environment in a representative sample of 173 active and inactive nearby galaxies. The sample covers a wide range in bulge mass, nuclear activity, morphology, and environment. The Legacy *e*-MERLIN Multi-band Imaging of Nearby Galaxies Survey (LeMMINGs; Beswick et al. 2014; Baldi et al. 2021a, b; Williams et al. 2022) is designed to exploit synergies from a large sample of high-resolution, multiwavelength data (*e*-MERLIN radio, *HST*: optical plus IR and *Chandra*: X-ray). As part of LeMMINGs, we have recently published *e*-MERLIN 1.5 GHz observations of all 280 galaxies above declination, $\delta > +20^\circ$ from the Palomar bright spectroscopic sample of nearby galaxies (Baldi et al. 2018, 2021a, b). In Williams et al. (2022), we presented the *Chandra* X-ray properties for the nuclei of a statistically complete sample of 213 LeMMINGs galaxies. *Spitzer* and *Herschel* data for the full sample of LeMMINGs galaxies are currently being analysed (Bendo et al., in preparation). High-resolution optical and near-infrared observations are desirable to derive accurate central and global galaxy structural properties. In Dullo et al. (2023), we performed multicomponent decompositions of optical/near-IR surface brightness profiles from *HST*, separating bulges, discs, bars, spiral-arm, and nuclear components.

The structure of this paper is as follows. In Section 2, we describe the LeMMINGs sample and the associated radio and optical emission-line data, the bulge properties characterized, and quantified using *HST* imaging data and the ancillary (*GALEX* UV and *Spitzer* 3.6 μm) data used in the paper. In Section 3, we examine how nuclear radio emissions separated based on optical emission-line types relate to bulge properties and environment. Section 4 presents scaling relations between the radio core luminosity and host bulge properties. Section 5 discusses our results in the context of models of galaxy formation and evolution to provide insights into the AGN triggering processes and their implications for the nuclear radio activity. Finally, in Section 6 we summarize our main results and conclude. There are two appendices. Appendix A1 gives details of our local density calculations, as a measure of the galaxy environment. The global and central properties of the sample galaxies are presented in Appendix A2.

We use $H_0 = 70 \text{ km s}^{-1} \text{ Mpc}^{-1}$, $\Omega_m = 0.3$, and $\Omega_\Lambda = 0.7$ (e.g. Freedman et al. 2019), which is the average of the Planck 2018 Cosmology $H_0 = 67.4 \pm 0.5 \text{ km s}^{-1} \text{ Mpc}^{-1}$ (Planck Collaboration VI 2020) and the LMC $H_0 = 74.22 \pm 1.82 \text{ km s}^{-1} \text{ Mpc}^{-1}$ (Riess et al. 2019). While *GALEX* UV and *Spitzer* 3.6 μm data are in AB magnitude system, other quoted magnitudes in the paper are in the Vega system, unless specified otherwise.

2 DATA

All the data used in this work are published elsewhere (Baldi et al. 2018, 2021a, b; Bouquin et al. 2018; Dullo et al. 2023; see Table 1).

Table 1. Multiwavelength data.

Data	<i>N</i> (parent sample/this work)
(1)	(2)
1.5 GHz <i>e</i> -MERLIN radio data ^[1r]	280/173
Optical spectral classification ^[1r]	280/173
<i>HST</i> data ^[2r]	173/173
<i>GALEX</i> UV band and <i>Spitzer</i> 3.6 μm data ^[3r]	1931/140

Note. Col (1): multiwavelength data used in this work. Col (2): number of galaxies (*N*) in the parent sample and in the subsample used in this work. References. 1r = Baldi et al. (2018, 2021a, b); 2r = Dullo et al. (2023); 3r = Bouquin et al. (2018).

2.1 The LeMMINGs

In this work, we use a sample drawn from the full LeMMINGs (Beswick et al. 2014; Baldi et al. 2018, 2021a, b) sample of 280 nearby galaxies, which in turn is a subset of the magnitude-limited ($B_T \leq 12.5 \text{ mag}$ and declinations $\delta > 0^\circ$) Palomar spectroscopic sample of 486 bright galaxies (Ho, Filippenko & Sargent 1995, 1997a). By design, all LeMMINGs galaxies have $\delta > +20^\circ$, ensuring reliable radio visibility coverage for the *e*-MERLIN array. The LeMMINGs capitalizes on the sub-mJy sensitivity ($\sigma \sim 0.08 \text{ mJy beam}^{-1}$) and high angular resolution ($\sim 0''.15$) radio continuum observations of the full LeMMINGs sample taken with *e*-MERLIN at 1.5 GHz for a total of 810 h (Baldi et al. 2018, 2021a). This legacy survey constitutes the deepest high-resolution radio study of the local Universe and aims to investigate AGN accretion and star formation events for a large sample of nearby galaxies. The full LeMMINGs sample, which encompasses all the Palomar galaxies with $\delta > 20^\circ$, is statistically complete akin to its parent Palomar sample.

Full details of the goals, radio data reduction technique, radio detection, and flux measurements of the LeMMINGs can be found in Baldi et al. (2018, 2021a). Here, we use the radio core properties of the LeMMINGs galaxies including radio detection, sub-kpc radio structures, and radio core luminosities which span six orders of magnitude ($L_{R, \text{core}} \sim 10^{34} - 10^{40} \text{ erg s}^{-1}$) (Baldi et al. 2018, 2021a), as listed in Tables 2 and A1. For the sub-kpc radio structures, we adopt the classification scheme used in Baldi et al. (2018) namely class A = core/core jet, class B = one-sided jet, class C = triple sources, class D = doubled-lobed, and class E = jet + complex shapes.

Our optical spectral classifications are taken from Baldi et al. (2018, 2021a). In their spectroscopic study of the nuclear ionization mechanisms of the Palomar galaxies, Ho et al. (1997a, their table 5) applied optical emission-line ratios along with spectral classification criteria to divide the sample into Seyferts, LINERs, H II, and Transition galaxies. In order to revise the spectral classification for the LeMMINGs galaxies, Baldi et al. (2018, 2021a) used emission-line ratios taken mainly from Ho et al. (1997a, see also Filippenko & Sargent 1985; Ho et al. 1995, 1997a, b, c) and applied the emission-categorized diagnostic diagrams by Kewley et al. (2006) and Buttiglione et al. (2010), see Dullo et al. (2023). In this revised classification adopted here, the LeMMINGs galaxies with emission lines were categorized as Seyfert, LINER, and H II galaxies, whereas those which lack emission lines were dubbed ‘absorption-line galaxies (ALGs)’, see Table A1.

2.2 Sample and detailed structural analysis with *HST*

Our sample consists of 173 LeMMINGs galaxies (23 Es, 42 S0s, 102 Ss, and 6 Irrs), for which we were able to obtain decent *HST*

Table 2. LeMMINGs optical and radio properties.

Galaxies	Number (our/full sample)	Undetected (our/full sample)	core-Sérsic (our sample)
(1)	(2)	(3)	(4)
E	23 (13.2 per cent)/26(9.3 per cent)	52.2 per cent/50.0 per cent	65.2 per cent
S0	42 (24.3 per cent)/55(19.6 per cent)	40.5 per cent/41.8 per cent	11.9 per cent
S	102 (59.0 per cent)/189(67.1 per cent)	54.0 per cent/60.3 per cent	0 per cent
Irr	6 (3.5 per cent)/10(3.6 per cent)	66.7 per cent/70.0 per cent	0 per cent
Seyfert	10 (5.8 per cent)/18 (6.4 per cent)	20.0 per cent/27.8 per cent	0 per cent
ALG	23 (13.3 per cent)/28 (10.0 per cent)	78.3 per cent/75.0 per cent	34.5 per cent
LINER	71 (41 per cent)/94 (33.6 per cent)	30.1 per cent/38.3 per cent	15.5 per cent
H II	69 (39.9 per cent)/140 (50.0 per cent)	67.6 per cent/66.4 per cent	1.7 per cent
Total	173 (100 per cent)/280 (100 per cent)	52.0 per cent/56.1 per cent	20/173 (11.6 per cent)

Note. The sample galaxies are first separated based on the galaxy morphological and optical spectral classes (cols (1) and (2)) and then further divided based on their radio non-detection and core-Sérsic type central structure (cols (3) and (4)). The term ‘full sample’ refers to the total LeMMINGs sample of 280 galaxies, whereas the term ‘our sample’ refers to the sub-sample of 173 LeMMINGs galaxies studied in this paper.

imaging in the Hubble Legacy Archive (HLA²) at the start of this project (Dullo et al. 2023, their table 1). The aim of this paper is to investigate how the nuclear activity depends on bulge structural properties utilizing sub-arcsec resolution ($\sim 5\text{--}10$ pc at the mean distance for our sample of ~ 22 Mpc) optical and radio properties derived from *HST* and 1.5 GHz *e*-MERLIN radio observations. To achieve this, the bulge must first be isolated from the rest of the galaxy through detailed photometric decompositions. Dullo et al. (2023) used *HST* (ACS, WFPC2, WFC3, and NICMOS) imaging to extract surface brightness profiles which cover a large radial extent of $R \gtrsim 80 - 100$ arcsec ($\gtrsim 2R_{e,\text{bulge}}$). This enabled our fitted galaxy models to accurately constrain the shape of the stellar light distributions associated with the bulges and the outer stellar galaxy components including bars, discs, rings, haloes, and spiral arms.

We performed accurate, multicomponent decompositions of the surface brightness profiles and fitted up to six galaxy components (i.e. bulge, disc, partially depleted core, AGN, nuclear star cluster (NSC), bar, spiral arm, and stellar halo and ring), simultaneously, using Sérsic and core-Sérsic models. The galaxy decompositions constitute the largest, most detailed structural analysis of nearby galaxies with *HST* to date. Uncertainties on the fitted bulge and other galaxy parameters were derived by decomposing simulated surface brightness profiles generated via a Monte Carlo (MC) technique. The bulge and galaxy structural data used here ($M_{V,\text{bulge}}$, $M_{V,\text{glxy}}$, $M_{*,\text{bulge}}$, $M_{*,\text{glxy}}$, ϵ_{bulge} , $B_{4,\text{bulge}}$ and γ , Tables 2 and A1) are tabulated in Dullo et al. (2023, Tables A1–A4). We note that the sample covers over six orders of magnitude in bulge stellar mass ($6 \lesssim \log M_{*,\text{bulge}} \lesssim 12.5$) and contains all Hubble types from Im to E (Hubble 1926; de Vaucouleurs 1959).

In order to study the scaling relations between the radio core luminosity and the optical properties of galaxies, it is crucial to examine the parameter space coverage afforded by our sample of 173 LeMMINGs galaxies. Motivated by this, in Dullo et al. (2023, Section 2) we revealed that our sample, despite being statistically incomplete, is representative of the statistically complete, full LeMMINGs sample. We went on to show that the entire ranges of radio core luminosity and galaxy luminosity probed

by the full LeMMINGs sample are also well traced by our sample.

2.3 GALEX NUV, FUV band, and *Spitzer* 3.6 μm data

AGN-driven feedback is postulated to be one of the main mechanisms for the cessation of star formation in galaxies (Silk & Rees 1998; Croton et al. 2006; King & Pounds 2015). The investigation of AGN activity therefore benefits from locating active and inactive LeMMINGs hosts on colour–colour and colour–mass diagrams. We make use of the Bouquin et al. (2018) UV and *Spitzer* 3.6 μm magnitudes to construct colour–mass diagrams for 140 LeMMINGs galaxies (see Section 3.5). Bouquin et al. (2018) published total *GALEX* NUV, FUV, and *Spitzer* 3.6 μm asymptotic, AB magnitudes for 1931 nearby galaxies. There are 140 (85) galaxies in common between their sample and the full (our *HST*) sample of 280 (173) LeMMINGs galaxies. Following Bouquin et al. (2018, their equations 1–3), we separate these 140 overlapping LeMMINGs galaxies into ‘red sequence’ (RS), ‘blue sequence’ (BS), and ‘green valley’ (GV) based on the (FUV–NUV)–(NUV – [3.6]) colour–colour diagram (see Table A1). The FUV and *Spitzer* 3.6 μm magnitudes were corrected for Galactic extinction but no internal dust attenuation correction was applied (Bouquin et al. 2018).

For the 55 (=140 – 85) galaxies which are in the full LeMMINGs sample but not in our *HST* sample, we compute 3.6 μm bulge stellar masses ($M_{\text{bulge},3.6}$) to create the colour–mass diagram (Section 3.5). To do so, we first calculate total galaxy stellar masses using the 3.6 μm asymptotic AB magnitudes (Bouquin et al. 2018), distances from NED, AB absolute magnitude for the Sun from Willmer (2018) of 6.0 and a 3.6 μm mass-to-light ratio of 0.6 (Meidt et al. 2014). The total galaxy masses were then converted into bulge stellar masses using the equations listed in Dullo et al. (2023, their table 5). Because we did not separate the bulge component using photometric decompositions the errors on $M_{\text{bulge},3.6}$ are large, typically of ~ 60 per cent.

3 NUCLEAR RADIO EMISSION, OPTICAL LINE EMISSIONS, AND THE CONNECTION WITH BULGE PROPERTIES AND ENVIRONMENT

In this section, we examine how the nuclear, radio, and emission-line properties for the LeMMINGs sample (Baldi et al. 2018, 2021a, b) vary as a function of host bulge properties and environment. We

²<https://hla.stsci.edu>.

Table 3. Scaling relations between radio core luminosity and galaxy properties.

Relation	OLS bisector fit	r_s/P -value	r_p/P -value	Sample
Active galaxies (LINERs+ Seyferts)				
$L_{R, \text{core}} - M_{*, \text{bulge}}$	$\log\left(\frac{L_{R, \text{core}}}{\text{erg s}^{-1}}\right) = (1.42 \pm 0.18)\log\left(\frac{M_{*, \text{bulge}}}{5 \times 10^{10} M_{\odot}}\right) + (36.22 \pm 0.15)$	$0.56/4.5 \times 10^{-8}$	$0.54/2.5 \times 10^{-7}$	81
$L_{R, \text{core}} - M_{V, \text{bulge}}$	$\log\left(\frac{L_{R, \text{core}}}{\text{erg s}^{-1}}\right) = (-0.74 \pm 0.09)(M_{V, \text{bulge}} + 20.5) + (36.43 \pm 0.16)$	$-0.53/3.06 \times 10^{-7}$	$-0.53/2.95 \times 10^{-7}$	81
$L_{R, \text{core}} - \sigma$	$\log\left(\frac{L_{R, \text{core}}}{\text{erg s}^{-1}}\right) = (4.85 \pm 0.58)\log\left(\frac{\sigma}{170 \text{ km s}^{-1}}\right) + (36.27 \pm 0.11)$	$0.72/7.9 \times 10^{-19}$	$0.66/2.8 \times 10^{-15}$	112
Inactive galaxies (ALG+ H II)				
$L_{R, \text{core}} - M_{*, \text{bulge}}$	$\log\left(\frac{L_{R, \text{core}}}{\text{erg s}^{-1}}\right) = (0.68 \pm 0.08)\log\left(\frac{M_{*, \text{bulge}}}{2 \times 10^9 M_{\odot}}\right) + (34.92 \pm 0.10)$	$0.73/7.1 \times 10^{-15}$	$0.64/6.4 \times 10^{-11}$	82
$L_{R, \text{core}} - M_{V, \text{bulge}}$	$\log\left(\frac{L_{R, \text{core}}}{\text{erg s}^{-1}}\right) = (-0.35 \pm 0.05)(M_{V, \text{bulge}} + 18.5) + (35.21 \pm 0.08)$	$-0.70/3.3 \times 10^{-13}$	$-0.64/1.1 \times 10^{-10}$	82
$L_{R, \text{core}} - \sigma$	$\log\left(\frac{L_{R, \text{core}}}{\text{erg s}^{-1}}\right) = (3.06 \pm 0.23)\log\left(\frac{\sigma}{65 \text{ km s}^{-1}}\right) + (34.91 \pm 0.07)$	$0.58/7.9 \times 10^{-16}$	$0.56/1.2 \times 10^{-14}$	164
All galaxies				
$L_{R, \text{core}} - M_{\text{BH}}$	$\log\left(\frac{L_{R, \text{core}}}{\text{erg s}^{-1}}\right) = (1.45 \pm 0.20)\log\left(\frac{M_{\text{BH}}}{3 \times 10^7 M_{\odot}}\right) + (35.80 \pm 0.19)$	$0.52/2.6 \times 10^{-5}$	$0.57/2.3 \times 10^{-6}$	59
$L_{R, \text{core}} - \sigma$	$\log\left(\frac{L_{R, \text{core}}}{\text{erg s}^{-1}}\right) = (3.61 \pm 0.24)\log\left(\frac{\sigma}{100 \text{ km s}^{-1}}\right) + (35.46 \pm 0.06)$	$0.65/7.2 \times 10^{-35}$	$0.64/2.9 \times 10^{-33}$	276
Censored analysis				
Relation	Linear regression from ASURV	r_s/P -value	r_p/P -value	Sample
Active galaxies (LINERs+ Seyferts)				
$L_{R, \text{core}} - M_{*, \text{bulge}}$	$\log\left(\frac{L_{R, \text{core}}}{\text{erg s}^{-1}}\right) = (1.19 \pm 0.22)\log\left(\frac{M_{*, \text{bulge}}}{5 \times 10^{10} M_{\odot}}\right) + (35.9 \pm 1.8)$	–	–	81
$L_{R, \text{core}} - M_{V, \text{bulge}}$	$\log\left(\frac{L_{R, \text{core}}}{\text{erg s}^{-1}}\right) = (-0.53 \pm 0.12)(M_{V, \text{bulge}} + 20.5) + (36.0 \pm 1.7)$	–	–	81
$L_{R, \text{core}} - \sigma$	$\log\left(\frac{L_{R, \text{core}}}{\text{erg s}^{-1}}\right) = (5.10 \pm 0.60)\log\left(\frac{\sigma}{170 \text{ km s}^{-1}}\right) + (35.9 \pm 0.9)$	–	–	112
Inactive galaxies (ALG+ H II)				
$L_{R, \text{core}} - M_{*, \text{bulge}}$	$\log\left(\frac{L_{R, \text{core}}}{\text{erg s}^{-1}}\right) = (0.74 \pm 0.16)\log\left(\frac{M_{*, \text{bulge}}}{2 \times 10^9 M_{\odot}}\right) + (33.7 \pm 1.6)$	–	–	82
$L_{R, \text{core}} - M_{V, \text{bulge}}$	$\log\left(\frac{L_{R, \text{core}}}{\text{erg s}^{-1}}\right) = (-0.36 \pm 0.08)(M_{V, \text{bulge}} + 18.5) + (34.0 \pm 1.6)$	–	–	82
$L_{R, \text{core}} - \sigma$	$\log\left(\frac{L_{R, \text{core}}}{\text{erg s}^{-1}}\right) = (2.70 \pm 0.48)\log\left(\frac{\sigma}{65 \text{ km s}^{-1}}\right) + (33.9 \pm 0.8)$	–	–	164
All galaxies				
$L_{R, \text{core}} - \sigma$	$\log\left(\frac{L_{R, \text{core}}}{\text{erg s}^{-1}}\right) = (3.97 \pm 0.34)\log\left(\frac{\sigma}{100 \text{ km s}^{-1}}\right) + (34.7 \pm 0.6)$	–	–	276

Note. Radio core luminosity ($L_{R, \text{core}}$) as a function of bulge stellar mass ($M_{*, \text{bulge}}$), absolute magnitude ($M_{V, \text{bulge}}$), central velocity dispersion (σ) and measured blackhole mass (M_{BH}) for active and inactive galaxies. The different columns represent: the OLS bisector fits to the data, the Spearman and Pearson correlation coefficients (r_s and r_p , respectively) and the associated probabilities for a serendipitous correlation. We also show censored linear regressions using ASURV, accounting for upper limits, see Section 4.1 for details.

make use of sets of bulge structural properties over large stellar mass and morphology³ ranges obtained from accurate modelling of *HST* surface brightness profiles for a sample of 173 LeMMINGs galaxies. While the study of the dependence of bulge structural properties on galaxy properties such as morphology is not new (e.g. Laurikainen, Salo & Buta 2005; Graham & Worley 2008; Kormendy & Bender 2012; Salo et al. 2015; Méndez-Abreu et al. 2017), a robust characterization of galaxy structures using homogeneously measured high-resolution optical and radio data for a large sample of galaxies

³To analyse the galaxies properties, we divided the sample into two morphological classes, early-type galaxies (Es and S0s) and late-type galaxies (Ss and Irrs).

was not possible to date. In particular, our analysis focuses on the bulge component as it is known to correlate better with the mass of the SMBH and other central galaxy properties than the galaxy disc at large radius.

3.1 The relations between radio detection, radio morphology, and bulge properties

Fig. 1 shows the relation between the Sérsic index and bulge mass ($n - M_{*, \text{bulge}}$) colour-coded by galaxy radio morphology. Of the 173 sample galaxies, we detect radio emission $\gtrsim 0.2$ mJy from 83 galaxies (filled circles) with *e*-MERLIN at 1.5 GHz. This gives a detection rate of 48 per cent, in fair agreement with that from the full sample (44 per cent). Of the 83 galaxies, five (NGC 3034,

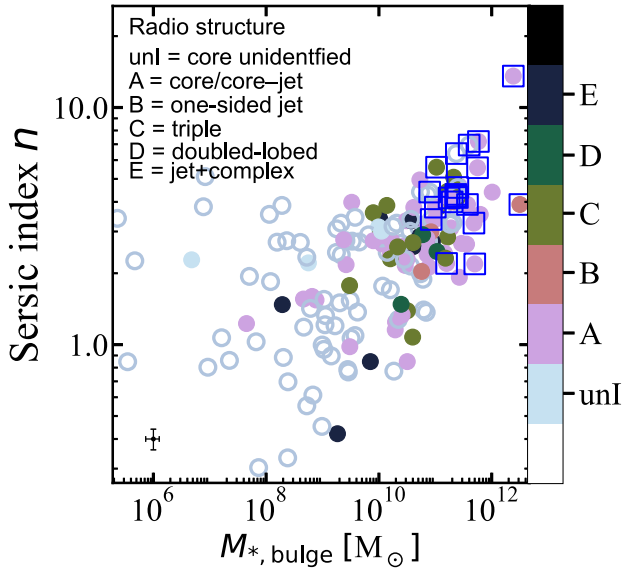


Figure 1. Dependence of radio morphological class (Baldi et al. 2018) on the Sérsic index (n) and the stellar mass of the bulge ($M_{*,\text{bulge}}$), see Table A1. Filled circles show the galaxies in our sample that are radio detected with e -MERLIN at 1.5 GHz, whereas open circles are for undetected galaxies. The radio morphological types of B (‘one-sided jet’), C (‘triple’), and D (‘doubled-lobed’) are indicative of the presence of a jet (see the text for details). While radio detection and presence of jets strongly depend on both n and $M_{*,\text{bulge}}$, the latter is a better predictor. Core-Sérsic galaxies (enclosed in blue squares) can assume morphologies A, B, C, D and unI, and 7/20 (35 per cent) of them are undetected with e -MERLIN at 1.5 GHz.

NGC 3838, NGC 4242, NGC 5273, and NGC 5907) are radio-detected but core-unidentified; they have low Sérsic indices ($n \lesssim 3$), faint bulge magnitudes ($M_{V,\text{bulge}} \gtrsim -18.9$ mag), and low stellar bulge masses ($M_{*,\text{bulge}} \lesssim 10^{10} M_{\odot}$). The remaining 90 undetected sources are denoted by open circles. The radio detection fraction increases with bulge mass, n and bulge-to-total flux ratio (B/T). At $M_{*,\text{bulge}} \gtrsim 10^{11} M_{\odot}$, this fraction is 77 per cent, but it declines to 24 per cent for $M_{*,\text{bulge}} < 10^{10} M_{\odot}$. For $M_{*,\text{bulge}} \gtrsim 10^{11} M_{\odot}$ the mean values of n and B/T are $n = 4.00 \pm 1.50$, $B/T = 0.79 \pm 0.24$, while we measure mean values of $n = 1.52 \pm 1.06$, $B/T = 0.10 \pm 0.10$ for $M_{*,\text{bulge}} < 10^{10} M_{\odot}$. Large $M_{*,\text{bulge}}$ and high n values however are not strictly associated with radio detection at e -MERLIN sensitivity. Most massive undetected sources are ALGs, the second most common type being LINERs.

The radio morphological types of B (‘one-sided jet’), C (‘triple’), and D (‘doubled-lobed’) are indicative of the presence of a radio jet (Baldi et al. 2018). It is evident that radio jetted sources are among the more massive galaxies with a mass range of $M_{*,\text{bulge}} \sim 3.0 \times 10^9 - 3.2 \times 10^{12} M_{\odot}$ and a median mass of $\log M_{*,\text{bulge}}/M_{\odot} = 10.8 \pm 0.6$. Radio morphology type A (‘core/core-jet’) galaxies tend to be massive⁴ (i.e. a median mass of $\log M_{*,\text{bulge}}/M_{\odot} = 10.7 \pm 1.0$) but they trace a wide range of n (~ 1 – 13) and mass ($M_{*,\text{bulge}} \sim 10^7 - 3 \times 10^{12} M_{\odot}$). While radio morphology types A and E (Baldi et al. 2018) do not guarantee a jet with e -MERLIN at 1.5 GHz, the most massive ‘core/core-jet’ galaxies are probably jetted (see Table A1). Core-Sérsic galaxies (enclosed in blue squares) can assume all radio

⁴Note that over the mass range of $M_{*,\text{bulge}} \sim 3.0 \times 10^9 - 3.2 \times 10^{12} M_{\odot}$ traced by our jetted galaxies, we find a median mass for type A galaxies of $\log M_{*,\text{bulge}}/M_{\odot} = 10.9 \pm 0.7$.

morphologies except E, and 7/20 (35 per cent) of them are undetected with e -MERLIN at 1.5 GHz.

3.2 The incidence of optical (emission-line) and radio AGN as a function of stellar mass, luminosity, and Hubble type

The motivation here is to see how the AGN fraction varies with the host galaxy photometric properties. Due to the high radio detection and radio jet incidence for more massive bulges (Section 3.1), a correlation is expected also between the AGN fraction and the bulge mass, bulge magnitude, and other related galaxy properties. Fig. 2 shows the distributions of bulge luminosity ($M_{V,\text{bulge}}$), total galaxy luminosity ($M_{V,\text{glxy}}$), bulge stellar mass ($M_{*,\text{bulge}}$), galaxy stellar mass ($M_{*,\text{glxy}}$), and Hubble type for AGN and non-AGN hosts. Galaxies with LINERs and Seyferts nuclei are active and simply referred to as ‘optical AGN’ (orange curve), while ALGs and H II, which are considered inactive, constitute the non-AGN subsample. Galaxies which are dubbed as ‘radio AGN’ (green curve) are limited to those with radio morphologies B (‘one-sided jet’), C (‘triple’) and D (‘doubled-lobed’) and radio detected LINERs and Seyferts, see Table A1. We note that the bulk (87 per cent) of the sample galaxies with radio morphologies B, C, and D are radio detected LINERs and Seyferts. All the ‘Radio AGN’ galaxies in the sample have AGN-like spectral emission except for three inactive galaxies (NGC 3348, NGC 3665, and NGC 4217).

Having defined the AGN fraction as the ratio between the number of galaxies with an AGN and the total number of galaxies under consideration, there is strong evidence for correlation between the optical AGN fraction and bulge stellar mass and luminosity (Fig. 2). Using the symmetrical ordinary least-squares (OLS) bisector regression (Feigelson & Babu 1992), we find the fraction of optical AGN galaxies is such that $f_{\text{optical-AGN}} \propto M_{*,\text{bulge}}^{0.24 \pm 0.06}$ and $f_{\text{optical-AGN}} \propto M_{*,\text{glxy}}^{0.30 \pm 0.05}$. The majority of optical AGN (80 per cent) and radio AGN (90 per cent) hosts have bulges more massive than $M_{\text{bulge}} \sim 10^{10} M_{\odot}$ ($M_{\text{glxy}} \sim 10^{10.5} M_{\odot}$) and brighter than $M_{V,\text{bulge}} \sim -18.2$ mag ($M_{V,\text{glxy}} \sim -20.0$ mag) (see Fig. 2). From a bulge magnitude of -15.5 to -18 mag, the optical AGN fraction increases dramatically from 22 ± 5 to 50 ± 4 per cent, before rising gently to 77 ± 3 per cent from $M_{V,\text{bulge}} \sim -18$ to -22.5 mag. Between bulge mass of $M_{*,\text{bulge}} \sim 10^{8.5}$ and $10^{11.3} M_{\odot}$, the optical AGN fraction steadily rises from 15 ± 4 to 80 ± 5 per cent. In general, the trend of the optical AGN fraction for the bulge mirrors that of the host galaxy. We note that of the 32 galaxies in the sample having $M_{*,\text{glxy}} \lesssim 5 \times 10^9 M_{\odot}$ and thus defined to be low-mass by Penny et al. (2018) only three (NGC 404, NGC 1058, and NGC 3982) host an active AGN, yielding an optical AGN fraction for this low-mass domain of 9.4 per cent, which is comparable to the 10 per cent reported by Penny et al. (2018, see also Kaviraj, Martin & Silk 2019; Mezcuca, Suh & Civano 2019) at the same stellar mass range.

As with the optical AGN fraction, the ‘radio AGN’ fraction appears to be a function of stellar mass and luminosity. The fraction of radio AGN galaxies is such that $f_{\text{radio-AGN}} \propto M_{*,\text{bulge}}^{0.24 \pm 0.05}$ and $f_{\text{radio-AGN}} \propto M_{*,\text{glxy}}^{0.41 \pm 0.06}$. From a bulge magnitude of -17 to -19.5 mag, the ‘radio AGN’ fraction increases strongly from 17 ± 5 to 50 ± 4 per cent and then rising gently to 60 ± 5 per cent from $M_{V,\text{bulge}} \sim -19.5$ to -23.0 mag. From $M_{*,\text{bulge}} \sim 10^{10}$ to $10^{11.7} M_{\odot}$, the ‘radio AGN’ fraction increases from of 32 ± 7 to 68 ± 5 per cent, whereas when $M_{*,\text{glxy}}$ is considered over a similar mass range the ‘radio AGN’ fraction rises from 3 ± 3 to 25 ± 5 per cent.

We also checked the ‘radio AGN’ fraction by restricting the ‘radio AGN’ subsample to contain only jetted galaxies with radio

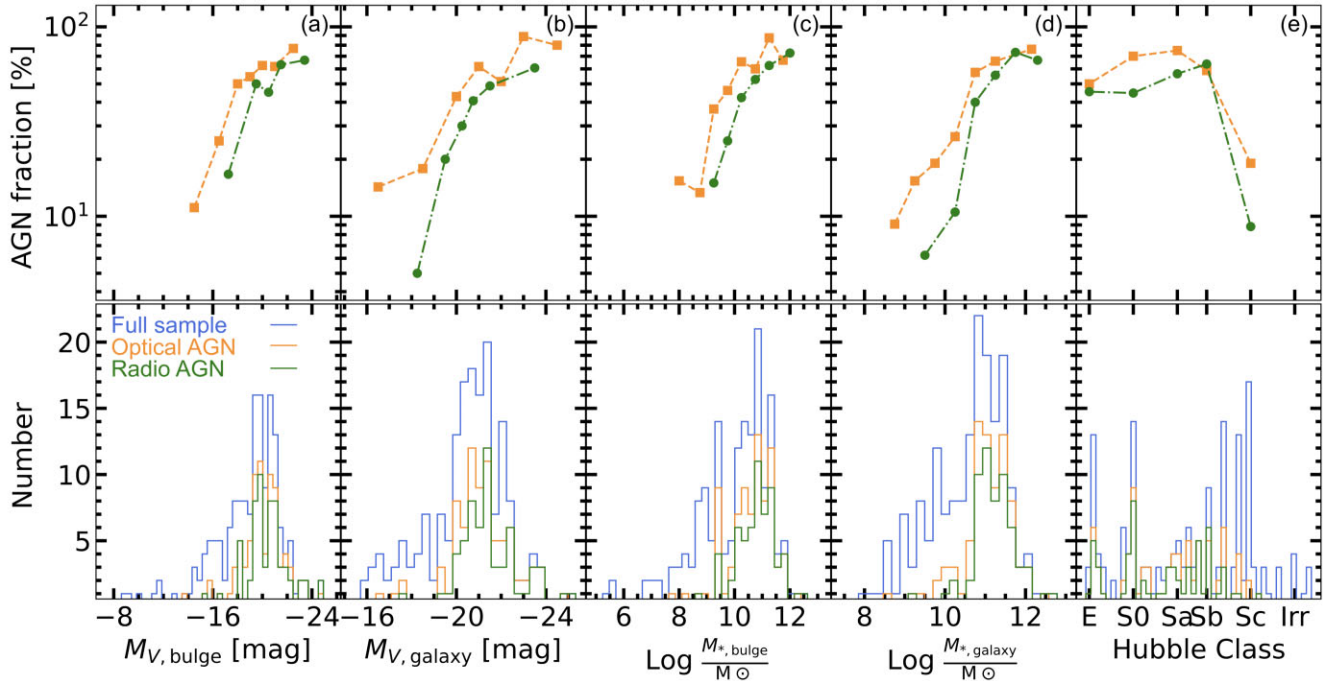


Figure 2. The relations between the AGN fraction and host galaxy properties. Top row: (a) AGN fraction as a function of bulge luminosity $M_{V, \text{bulge}}$, (b) total galaxy luminosity $M_{V, \text{galaxy}}$, (c) bulge stellar mass $M_{*, \text{bulge}}$, (d) galaxy stellar mass $M_{*, \text{galaxy}}$, and (e) morphology. Bottom row: distributions of $M_{V, \text{bulge}}$, $M_{V, \text{galaxy}}$, $M_{*, \text{bulge}}$, $M_{*, \text{galaxy}}$, and morphology for AGN and non-AGN hosts. The galaxies referred here to as ‘optical AGN’ (orange curve) are LINERs and Seyferts and those referred to as ‘radio AGN’ (green curve) are jetted objects with radio morphologies B (‘one-sided jet’), C (‘triple’), and D (‘doubled-lobed’) and radio detected LINERs and Seyferts.

morphologies B, C, and D. We find that the ‘jetted’ radio AGN fraction is a function of stellar mass and luminosity such that $f_{\text{jetted_radio_AGN}} \propto M_{*, \text{bulge}}^{0.17 \pm 0.05}$ and $f_{\text{jetted_radio_AGN}} \propto M_{*, \text{galaxy}}^{0.18 \pm 0.06}$. From $M_{*, \text{bulge}} \sim 10^{10}$ to $10^{11.3} M_{\odot}$, the jetted radio AGN fraction increases from 10 ± 5 to 30 ± 5 per cent, while for $M_{*, \text{galaxy}}$ considered over a similar mass range the jetted radio AGN fraction rises from 3 ± 3 to 25 ± 5 per cent. Owing to the low number statistics associated with the jetted radio AGN galaxies, we remind the need for caution when interpreting the aforementioned results. Furthermore, the quoted jetted radio AGN fractions are probably a lower limit, since massive galaxies with radio morphologies A and E might host a radio jet and inactive galaxies might have a weak AGN cloaked at their centres.

Although the trend of increasing radio AGN activity with increasing stellar mass has been previously reported (e.g. Kauffmann et al. 2003a; Best et al. 2005; Kauffmann et al. 2008; Heckman & Best 2014), our relation ($f_{\text{radio_AGN}} \propto M_{*, \text{galaxy}}^{0.41 \pm 0.06}$) is significantly shallower than the (radio-loud AGN fraction)–(galaxy stellar mass) relation found by Best et al. (2005, $f_{\text{Radio-loud_AGN}} \propto M_{*, \text{galaxy}}^{2.5}$). The discrepancy between the slopes from our work and Best et al. (2005) may be due to the higher sensitivity and higher angular resolution of our *e*-MERLIN radio data which allow for the identification of jetted, radio-quiet AGN. Note that the bulk of the outflows of ionized matter in a jet can be either relativistic, giving rise to a radio-loud AGN, or sub-relativistic, resulting in a radio-quiet AGN. Also shown in Fig. 2 are trends with optical morphological classes; we notice a variation in the AGN fraction across the Hubble sequence: 47.8 per cent of elliptical galaxies, 64.3 per cent of S0s, and 42.2 per cent of spiral galaxies (75 per cent of Sa, 54.6 per cent of Sb, and 20.5 per cent Sc) are optical AGN.

3.3 Dependence of nuclear radio emission and AGN fraction on environment

There are conflicting reports in the literature about the role of galaxy environment in triggering AGN activities and nuclear radio emissions (e.g. Man et al. 2019). This motivates us to investigate the environmental dependence of nuclear activities for the LeMMINGs galaxies. We apply two methods to measure the galaxy environments: local densities based on the nearest neighbour method and dark matter halo mass. Measures of the environment based on the nearest neighbours method are shown to approximate well the internal properties of the dark matter halo (Muldrew et al. 2012). For each galaxy in the sample, we derive local surface densities (ρ) and luminosity surface densities (ν) inside a cylinder containing the 3rd and 10th nearest neighbours with $M_B \lesssim -18.0$ mag and a velocity cut of $\Delta V_{\text{hel}} < 300$ km s⁻¹ (denoted by ρ_3 , ν_3 and ρ_{10} , ν_{10} , respectively, see Table A1, also Cappellari et al. 2011). A detailed discussion of the derivations of these environmental measures and their comparison with those from Cappellari et al. (2011) are available online. Given the strong correlations we find between ρ and ν (Spearman’s correlation coefficient $r_s \sim 0.93 - 0.96$, $P \sim 0$), throughout this paper we only consider the luminosity surface densities ν_{10} and ν_3 (see Table A1). We determine that the typical uncertainty on $\log \nu_{10}$ and $\log \nu_3$ is 0.60 dex.

For the halo mass (M_{halo}), we follow Veale et al. (2017b) and use the halo mass based on the projected mass estimator (Heisler, Tremaine & Bahcall 1985) from the Crook et al. (2007) high density contrast (HDC) group catalogue which provides halo mass estimates quantified based on the two different methods for groups with at least three members (see Table A1).

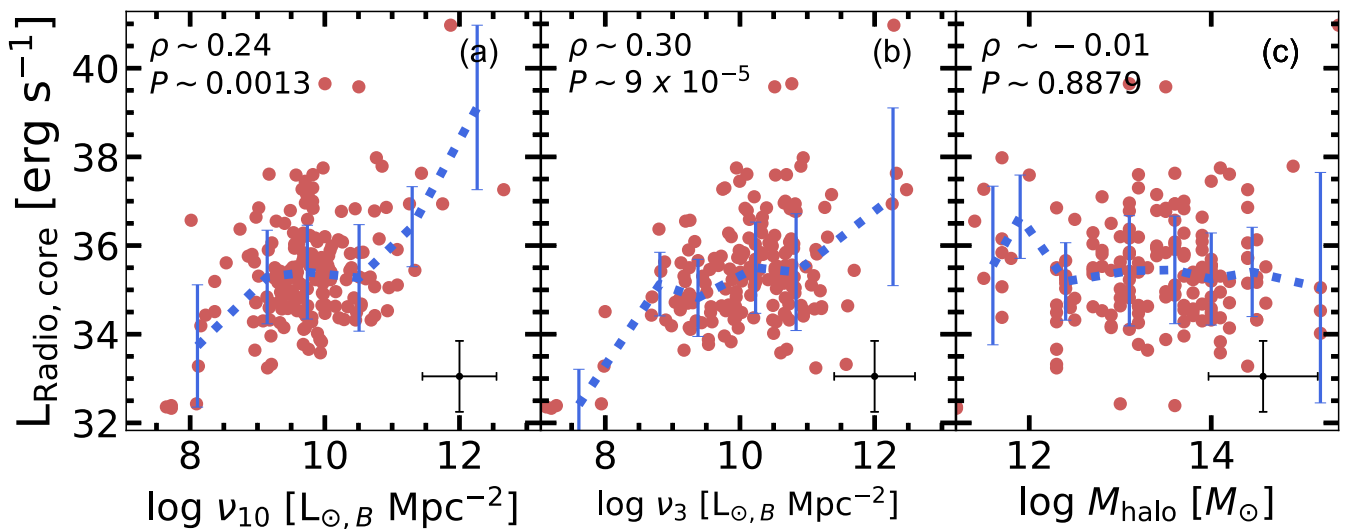


Figure 3. Radio core luminosity for our sample of 173 galaxies ($L_{R, \text{core}}$) plotted as a function of B -band luminosity surface density inside a cylinder enclosing the 10th nearest galaxy neighbour ν_{10} (a), B -band luminosity surface density for a cylinder containing three nearest neighbour ν_3 (b), and halo mass M_{halo} (c). The blue curve indicates the median $L_{R, \text{core}}$ values for the corresponding local density and halo mass bins. The error bars show the 1σ error on the measurements. Overall there is a mild tendency of the median $L_{R, \text{core}}$ values to increase with ν_{10} and ν_3 but no relation of $L_{R, \text{core}}$ with halo mass. However, removing the six outlying sample data points with high ν_3 ($> 10^{12} L_{\odot, B} \text{ Mpc}^{-2}$) and low ν_3 ($< 10^8 L_{\odot, B} \text{ Mpc}^{-2}$), the mild tendency disappears and the correlations between $L_{R, \text{core}}$ and ν become very weak and no correlation is seen between $L_{R, \text{core}}$ and M_{halo} : Spearman’s correlation coefficients and probabilities for the full sample are (a) $\rho \sim 0.13$, $P \sim 0.0924$, (b) $\rho \sim 0.20$, $P \sim 0.01231$, and (c) $\rho \sim -0.07$, $P \sim 0.3811$.

3.3.1 Radio core luminosity against local environment density and halo mass

We examine here whether the radio core luminosities ($L_{R, \text{core}}$) for our sample galaxies correlate with the local environment measures and halo masses. Fig. 3 shows $L_{R, \text{core}}$ plotted against (i) the B -band luminosity surface density inside a cylinder enclosing the 10th nearest neighbour ν_{10} , (ii) the same density but now inside a cylinder including the 3rd nearest neighbour ν_3 , and (iii) the halo mass M_{halo} . Note that a galaxy that inhabits a dense region, i.e. a galaxy located close to its neighbours, has high values of ν_3 and ν_{10} . Overall, we find the median radio core luminosities for our sample appear to increase slightly as a function of ν , but our galaxies reside in all environments, regardless of their radio core luminosities.

There is a weak correlation between $L_{R, \text{core}}$ and ν_{10} ($r_s \sim 0.24$, $P \sim 0.0013$), a marginally significant correlation between $L_{R, \text{core}}$ and ν_3 ($r_s \sim 0.30$, $P \sim 9 \times 10^{-5}$) and no correlation between $L_{R, \text{core}}$ and M_{halo} ($r_s \sim -0.01$, $P \sim 0.8879$). Excluding the six outlying sample data points, i.e. three with high ν_3 ($> 10^{12} L_{\odot, B} \text{ Mpc}^{-2}$) and three low ν_3 ($< 10^8 L_{\odot, B} \text{ Mpc}^{-2}$), see the middle panel, which seem to be driving the relations in Figs 3(a) and (b), we rerun the analysis, finding only weak correlations between $L_{R, \text{core}}$ and ν ($r_s \sim 0.13 - 0.20$, $P \sim 0.01231 - 0.0924$). For $L_{R, \text{core}}$ and M_{halo} the relation is consistent with the null hypothesis of no correlation ($r_s \sim -0.07$, $P \sim 0.3811$).

3.3.2 (Radio detection)-density and AGN-density relations in bins of fixed bulge stellar mass

The incidence of radio activity and AGN are strong functions of bulge mass M_{bulge} (Figs 1 and 2). Studies have also shown that bulge stellar mass depends on the host galaxy environment, with large numbers of massive, early-type (non-star forming) galaxies preferentially in higher density local environments (Dressler 1984; Gómez et al. 2003; Kauffmann et al. 2003b, 2004; Baldry et al. 2006; Peng et al. 2010),

see also Appendix A1. As such (radio detection)-density and AGN-density relations may be driven by M_{bulge} . Therefore in Fig. 4 we separate our sample into three (high-, intermediate-, and low-bulge) mass bins and examine how the radio detection, optical, and radio AGN fractions vary as a function of environment as measured by ν_{10} , ν_3 , and M_{halo} . Within each fixed M_{bulge} bin, we find no obvious dependence of the radio detection and AGN fraction on environment across the sample, regardless of the method we apply to define galaxy environment. For most of the cases in Fig. 4, the radio detection and (both optical and radio) AGN fraction remain unchanged over the five (four) orders of magnitude in ν_{10} and ν_3 (M_{halo}) probed by our sample. In general, the environments of the active galaxies in the sample are indistinguishable from those of inactive ones. Our results are in agreement with some past work (Miller et al. 2003; Pimblet et al. 2013; Amiri et al. 2019; Man et al. 2019), albeit see conflicting claims in the literature (e.g. Kauffmann et al. 2004).

3.4 Radio loudness

In order to gain further insight into the nuclear radio emissions in our galaxies, we divide them into radio-loud (RL) and radio-quiet (RQ) galaxies. Following Baldi et al. (2021b), in Dullo et al. (2023) we classified galaxies as RL when $\log(L_{\text{core}}/L_{\text{[O III]}}) > -2$ and $\log(M_{\text{BH}}/M_{\odot}) > 7.7$. This yielded 155 RQ and 18 RL galaxies in our sample; 17 of the 18 RL galaxies are LINERs and one is a (jetted) H II galaxy NGC 3665 (Table A1).

In Fig. 5, we present comparisons of the distributions of the properties of RQ and RL galaxies: Sérsic index (n), ellipticity, isophote shape parameter B_4 , negative, inner logarithmic slope (γ), Hubble type, ν_{10} , ν_3 , and M_{halo} . We run several two-sample Kolmogorov–Smirnov (KS) tests on the cumulative distributions of the RQ and RL data sets. When compared to RQ galaxies, we find that RL galaxies tend to possess an early-type morphology and inhabit a denser environment as defined by ν_3 . For the Hubble type and ν_3 , we can reject the null hypothesis that the RQ and RL data sets

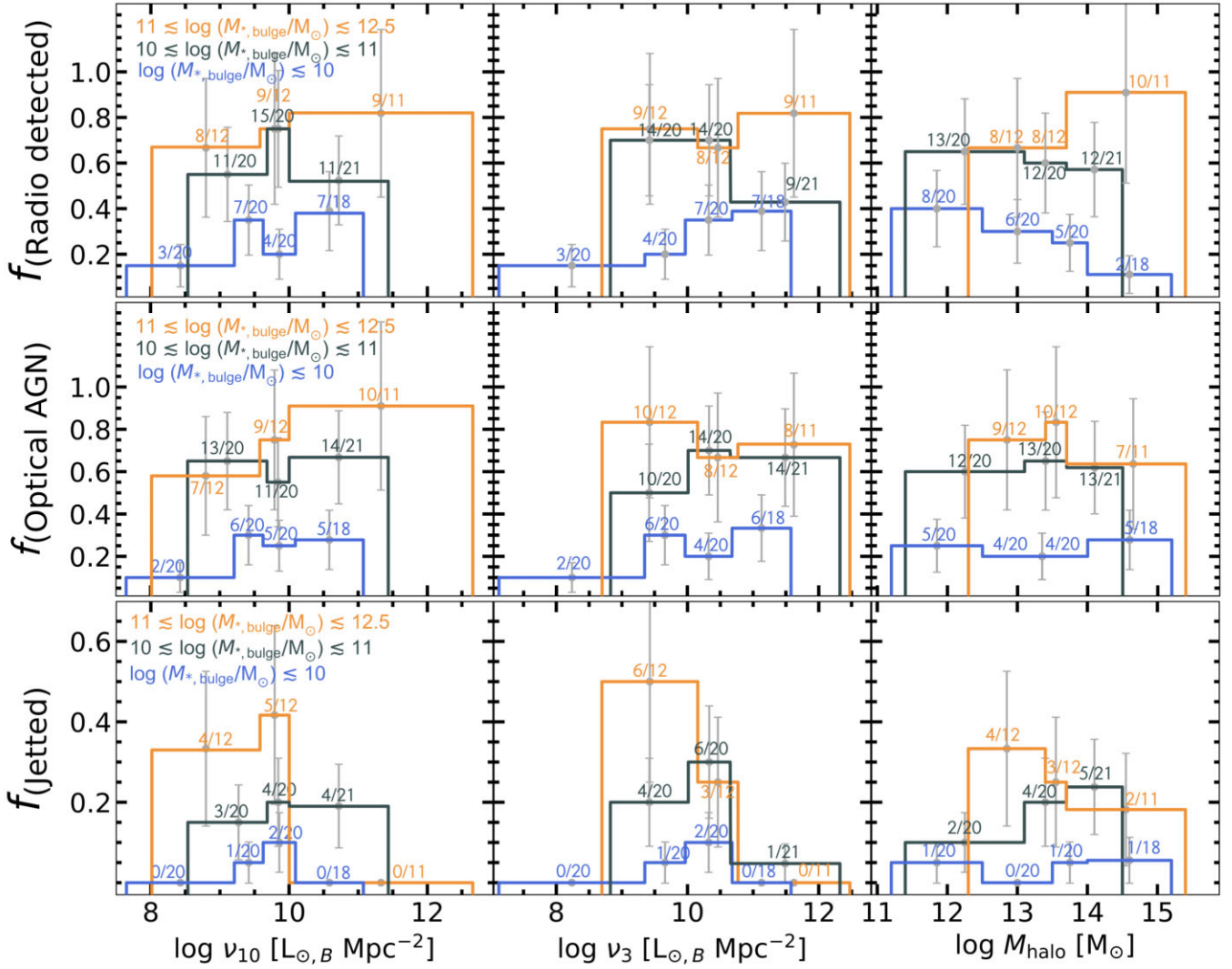


Figure 4. Radio detection, optical emission-line AGN and radio AGN fractions ($f_{\text{Radio detection}}$, $f_{\text{Optical AGN}}$, and $f_{\text{Radio AGN(Jetted)}}$, respectively) are plotted as a function of luminosity surface densities (ν_{10} and ν_3) and halo mass M_{halo} colour-coded by three (high-, intermediate-, and low-) bulge mass ($M_{*,\text{bulge}}$) bins. The error bars denote the Poisson errors. Within each $M_{*,\text{bulge}}$ bin considered, the radio detection and optical AGN fractions vary only mildly with ν_{10} , ν_3 , and M_{halo} . The only notable exception is the decrease in f_{Jetted} with increasing ν_3 for the massive bin (bottom row, middle panel).

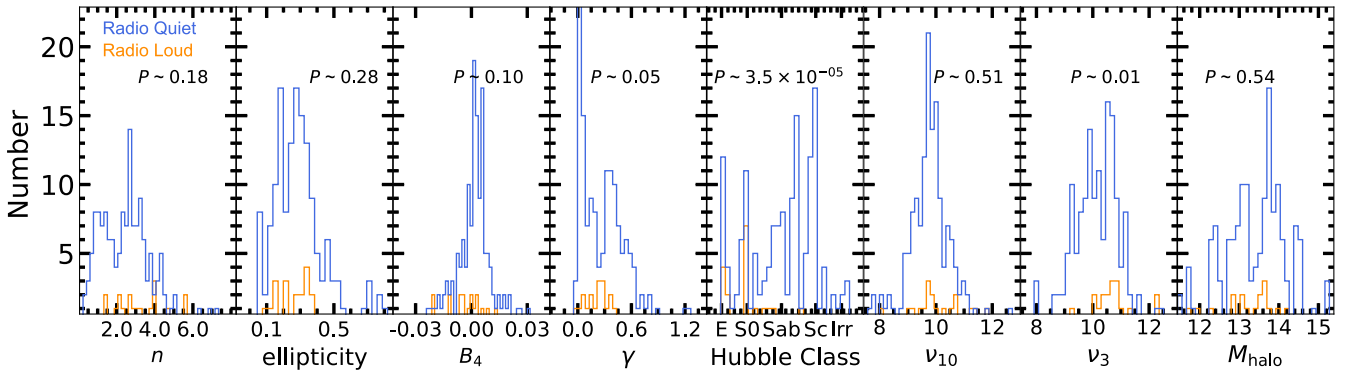


Figure 5. Properties of radio-quiet (RQ, blue curve) and radio-loud (RL, orange curve) sample galaxies. We show the distributions of the Sérsic index (n), ellipticity, isophote shape parameter B_4 , negative, inner logarithmic slope (γ), Hubble type, luminosity surface densities within cylinders enclosing the 10th and 3rd nearest neighbours (ν_{10} and ν_3) and halo mass (M_{halo}). We run two-sample Kolmogorov–Smirnov (KS) tests on the cumulative distributions of the RQ and RL data sets and show the corresponding P -values. For the galaxies’ Hubble type and ν_3 , we can reject the null hypothesis that the RQ and RL data sets are drawn from the same distributions as the P -values are < 0.05 . While the comparison of the γ distributions for RQ and RL galaxies yields a borderline case with $P \sim 0.05$, the null hypothesis cannot be rejected ($P > 0.05$) when KS tests are performed on the remaining properties of RQ and RL galaxies (n , ellipticity, B_4 , ν_3 , and M_{halo}).

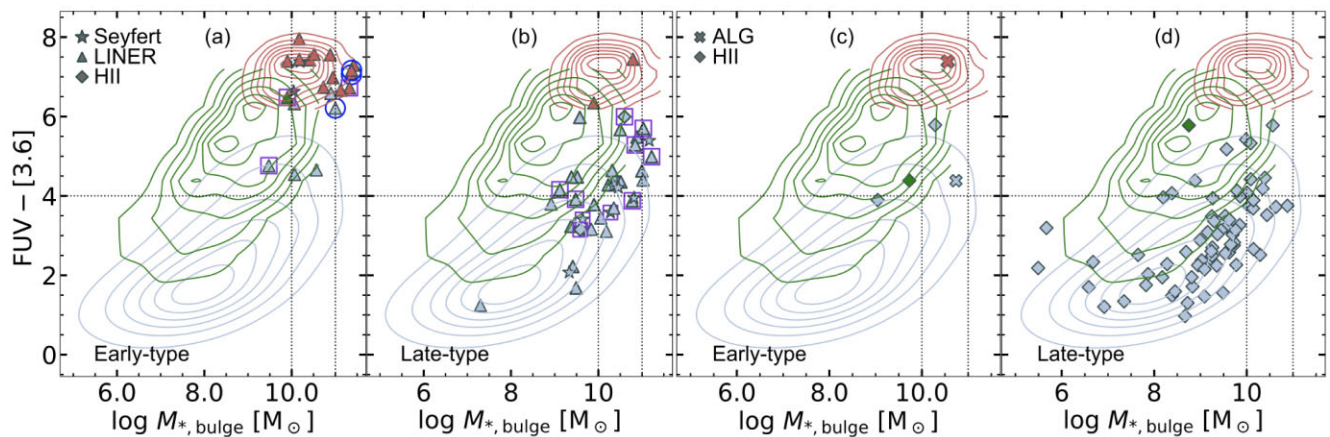


Figure 6. $(FUV-[3.6])$ galaxy colour versus bulge mass relation for 140 LeMMINGs galaxies that are in common with the sample of 1931 nearby galaxies from Bouquin et al. (2018), who published *GALEX* NUV, FUV, and *Spitzer* 3.6 μm asymptotic galaxy magnitudes. We divide the sample based on their optical spectral class (active: 12 Seyferts + 28 LINERs + 2 jetted H II galaxies, panels (a) and (b) and inactive: 2 ALGs plus 76 H II galaxies, panels (c) and (d)) and on morphology (27 early-type and 113 late-type). Of the 140 galaxies, 85 are in our sample and have accurate bulge mass measurements used here (Table A1). The bulge masses for the remaining 55 galaxies have been computed from the 3.6 μm magnitudes (Bouquin et al. 2018) and are not well constrained, see the text for further detail (Section 2.3). Red-sequence (RS), blue-sequence (BS), and green valley (GV) galaxies are shown in red, light-blue, and green contours which trace the *GALEX/S⁴G* results from the sample of 1931 (early- and late-type) galaxies, after converting the galaxies’ 3.6 μm magnitudes (Bouquin et al. 2018) into bulge masses using the equations in Dullo et al. (2023, their table 5), Section 2.3. The vertical lines delineate the low-, intermediate-, and high-(bulge mass) boundaries that we adopted in this work (see Section 5.3). Filled stars, triangles, and diamonds denote the Seyfert, LINER, and H II galaxies, while the filled ‘x’ symbols represent ALGs. ‘Jetted’ radio AGN hosts and core-Sérsic galaxies are enclosed in magenta squares and open blue circles, respectively. In general, the hosts of active galaxies (a and b) typically have $FUV-[3.6]$ colours > 4.0 , and lie above the blue, star-forming main sequence defined by inactive, star forming galaxies (d).

are drawn from the same distributions at P -values of < 0.05 . The evaluation of the γ distributions for RQ and RL galaxies with $P \sim 0.05$ is a borderline case, although there is a mild tendency for RL galaxies to have shallower inner slopes than RQ galaxies. Having performed KS tests on the remaining galaxy properties, we cannot reject the null hypothesis that the RQ and RL galaxies are drawn from identical distributions in n , ellipticity, B_4 , ν_{10} , and M_{halo} (P -values $\sim 0.10 - 0.54$).

Note that the only significant trend between nuclear activity and environment from our work is the tendency for RL galaxies to have high values of ν_3 , thus they preferentially reside in the highest local densities, however other environmental measures (ν_{10} and M_{halo}) do not corroborate the trend (see Fig. 5). Also, we have not ruled out whether the bulge mass is driving the trend between radio loudness and ν_3 . In summary, our results again suggest AGN and radio loudness are not environmentally driven and thus agree with what we found in Sections 3.3.1 and 3.3.2.

3.5 Active and inactive galaxies across the $(FUV-[3.6])$ – $M_{*,\text{bulge}}$ plane

In a continued effort to better examine the relationship between AGN activity and bulge growth, in Fig. 6 we show the $(FUV-[3.6])$ galaxy colour, which is a good proxy for the global star-formation per unit galaxy stellar mass (Bouquin et al. 2018; Dullo et al. 2020), against bulge stellar mass (M_{bulge}) (e.g. Baldry et al. 2004; Schawinski et al. 2014) for 140 LeMMINGs galaxies, 85 of which are in our sample (Table A1, see Section 2.3). We divide the sample based on their optical spectral class and morphology (27 early-type and 113 late-type). Also shown in Fig. 6 are red, light-blue, and green contours which trace the *GALEX/S⁴G* red-sequence (RS), blue-sequence (BS), and green valley (GV) defined by the sample of 1931 galaxies of Bouquin et al. (2018). We find that the vast majority of active early-type galaxies lie on the RS, while the remaining ones, with

intermediate-mass bulges, appear on the GV (Fig. 6a). These results suggest that the star formation in massive bulges was quenched by the AGN feedback on short time-scales ($\Delta t \lesssim 1$ Gyr; Bower, Lucey & Ellis 1992; Thomas, Greggio & Bender 1999; Wake et al. 2006). Active late-type galaxies reside preferentially in the red end of the blue sequence and they appear to define a transitioning sequence, where the bulges become more massive and redder as they march gradually on the RS (see also Faber et al. 2007; Westoby, Mundell & Baldry 2007; Schawinski et al. 2010; Vulcani et al. 2015; Belfiore et al. 2018). There is a caveat here. Fig. 6 plots integrated galaxy colours, while we actually seek to examine the bulge-SMBH co-evolution. In the case of disc galaxies, the use of galaxy colours likely bias the bulge colours bluewards, therefore most active late-type bulges would actually lie on the GV (Fig. 6).

Overall, the hosts of active galaxies (Figs 6a and b), typically have $FUV-[3.6]$ colours > 4.0 , and sit above the blue, star-forming main sequence defined by inactive, star forming galaxies (Fig. 6d). We also find that radio-loud LINERs lie on the RS. The ‘jetted’ radio AGN hosts (Figs 6 a and b) are predominantly (85 per cent) BS galaxies, co-spatial with the massive GV hosts or lie on the red end of the BS. These support the notion that AGN feedback shuts off or suppresses star formation in galaxies. We also find that all the three core-Sérsic galaxies in the subsample (Fig. 6, blue circles) are located on the red contour, this is expected since massive bulges are thought to form via gas-poor major merger events involving massive SMBHs.

The key question as to whether the AGN feedback and suppression of star formation in bulges are strictly coincidental is still being debated (e.g. Davies et al. 2007). Tackling this issue and addressing the time-scale of the AGN and its duty cycle (e.g. Shabala et al. 2008; Schawinski et al. 2015) is beyond the scope of this paper. For low-mass galaxies in clusters and groups the effects of the (weak) AGN and/or stellar feedback events may be limited to the central regions and thus less efficient in quenching the galaxies globally. Instead, for such galaxies, quenching is likely and maybe largely driven by

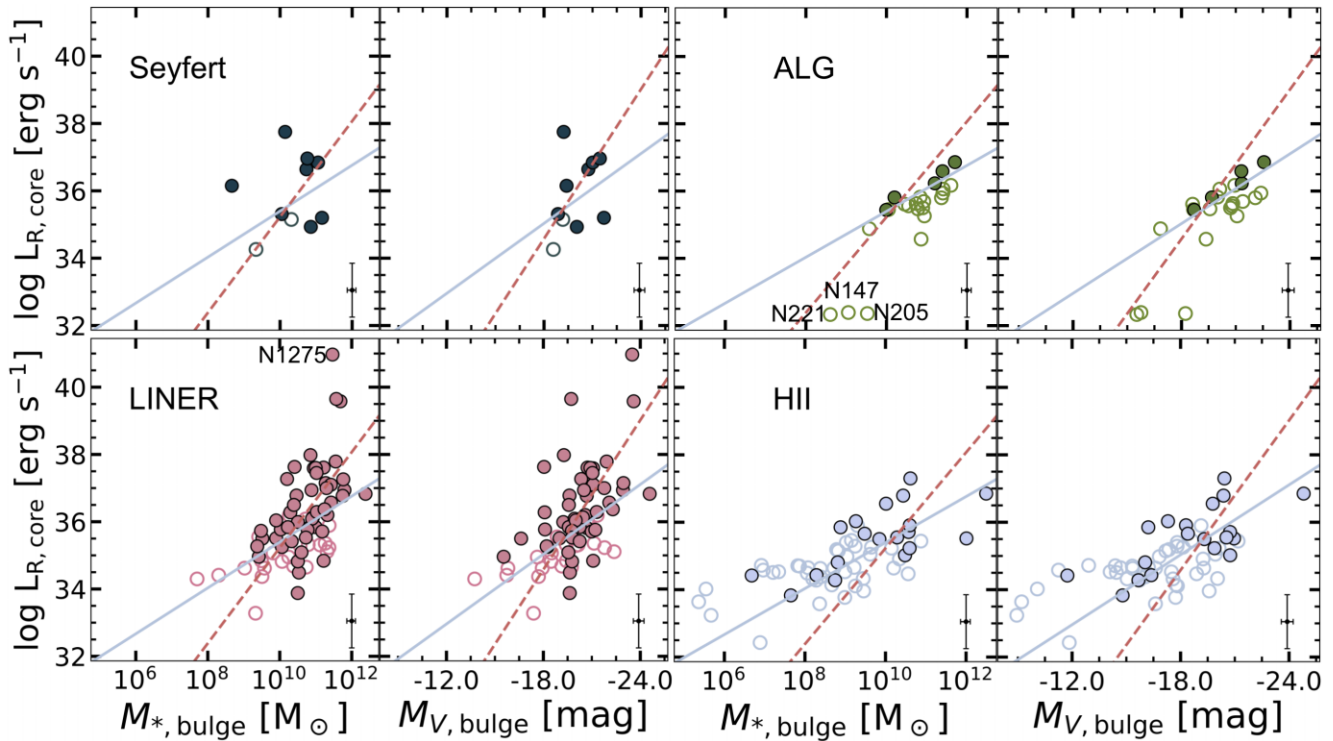


Figure 7. Correlations between the *e*-MERLIN 1.5 GHz radio core luminosity ($L_{R, \text{core}}$) and bulge stellar mass ($M_{*, \text{bulge}}$) and absolute *V*-band bulge magnitude ($M_{V, \text{bulge}}$) for our sample of 173 galaxies, separated by spectral classes. Filled circles show the galaxies in our sample that are radio-detected with *e*-MERLIN at 1.5 GHz, whereas open circles are for the undetected sources. Our $L_{R, \text{core}}$ values for the undetected sources are 3σ upper limits. The dashed and solid lines are OLS bisector regressions for the active galaxies (Seyferts (dark-green circles) and LINERs (pink circles)) and inactive galaxies (ALGs (green circles) and H IIs (light-blue circles)), respectively. NGC 147, NGC 205, and NGC 221, which are all ALGs and dwarf satellites of the Andromeda Galaxy, deviate significantly from the relations defined by inactive galaxies. A typical error bar associated with the data points is shown at the bottom of each panel.

environmental processes such as ram pressure stripping (Gunn & Gott 1972), galaxy–galaxy harassment (Moore et al. 1996), and/or strangulation (Larson, Tinsley & Caldwell 1980; Peng, Maiolino & Cochrane 2015).

3.6 Nuclear radio activity and kinematic morphology

In Dullo et al. (2023), we use a sample of 30 early-type galaxies in common with the ATLAS^{3D} sample (Emsellem et al. 2011) consisting of 4 slow rotators (SRs) and 26 fast rotators (FRs) to investigate the link between kinematics, central structure, and nuclear radio detection. The low number statistics in that work prohibited us from drawing conclusions, therefore we expand our sample here to 48 early-type galaxies (11 SRs + 37 FRs) by adding 8 galaxies that are in common between us and Veale et al. (2017b) plus 10 galaxies from the full LeMMINGs sample with no *HST* data (thus excluded in Dullo et al. 2023) that are in common with Emsellem et al. (2011). Of the 48 early-type galaxies, 38 (10 SRs + 28 FRs) have *HST* data and these are thus classified as Sérsic and core-Sérsic galaxies; we find 9 out of 10 (90 per cent) SRs are core-Sérsic galaxies, whereas 23/28 (82 per cent) FRs are Sérsic galaxies. It is apparent that the vast majority of SRs and FRs are core-Sérsic and Sérsic galaxies, respectively, consistent with the work of Krajnović et al. (2013); Veale et al. (2017a). The results can be naturally reconciled under the scenario that SRs are largely a consequence of experiencing predominantly gas-poor (‘dry’) mergers, whereas FRs are associated with wet mergers and gas-rich processes. For the 48 overlapping early-type galaxies (Emsellem et al. 2011; Veale et al. 2017b), we find

that, while SRs have a slightly higher radio detection rate than FRs, the radio detection fraction for the two kinematic classes are broadly consistent within the errors: 19/37 FRs (0.51 ± 0.15) and 7/11 SRs (0.64 ± 0.31) are radio detected with *e*-MERLIN at 1.5 GHz.

4 SCALING RELATIONS BETWEEN RADIO CORE LUMINOSITY AND BULGE PROPERTIES

Bulge prominence, a high bulge Sérsic index, and a large bulge mass are preferentially associated with nuclear radio activity (see Section 3.1, Dullo et al. 2023). Scaling relations between the central galaxy properties (such as bulge mass, bulge luminosity, SMBH mass, and velocity dispersion) and the radio luminosity provide insight into the origin of nuclear radio emissions and they can help constrain galaxy formation models (Ulvestad & Ho 2001a; Nagar et al. 2002; Filho et al. 2004; Nagar et al. 2005; Heckman & Best 2014; Baldi et al. 2018; Panessa et al. 2019; Baldi et al. 2021a, b). Taking advantage of the bulge masses and luminosities of LeMMINGs galaxies, accurately measured through our multicomponent decompositions, we investigate several radio core luminosity $L_{R, \text{core}}$ scaling relations. These are displayed in Figs 7, 8, 9, 10, and 11.

4.1 $L_{R, \text{core}} - M_{*, \text{bulge}}$ and $L_{R, \text{core}} - M_{V, \text{bulge}}$

Figs 7 and 8 show the relation between the radio core luminosity ($L_{R, \text{core}}$) and the bulge’s stellar mass $M_{*, \text{bulge}}$ and absolute *V*-band magnitude $M_{V, \text{bulge}}$, colour-coded based on the optical emission-line class. Separating the sample into active (Seyferts, LINERs, and two

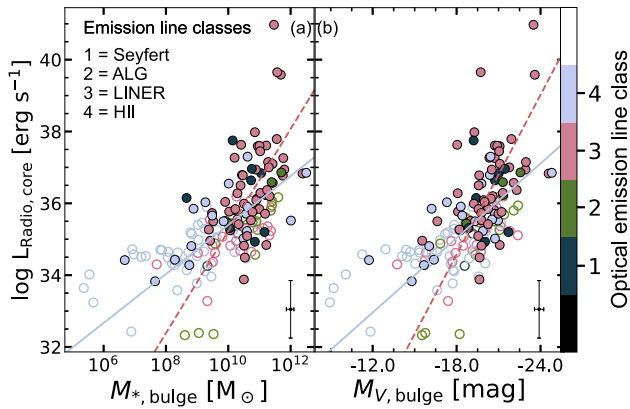


Figure 8. Similar to Fig. 7 but now showing the spectral classes together.

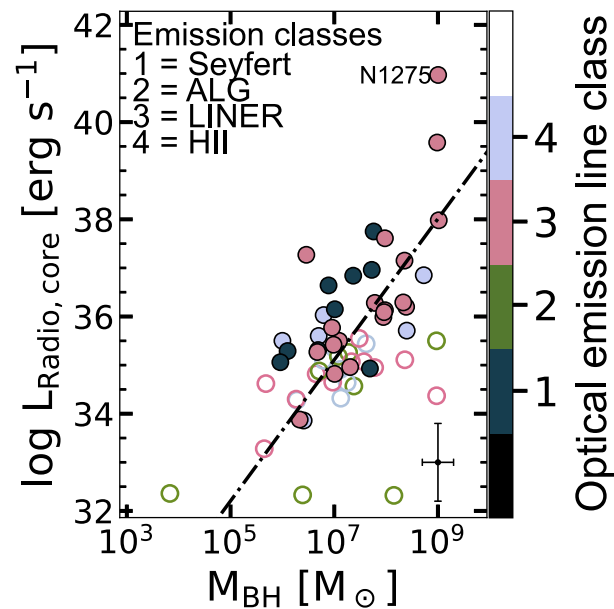


Figure 9. The radio core luminosity ($L_{R,core}$) as a function of the SMBH mass (M_{BH}) for all 59 LeMMINGS galaxies with measured M_{BH} . The dashed-dotted line is the OLS bisector regression fit to the data. A typical error bar associated with the data points is shown at the bottom.

jetted HII) and inactive (ALGs and HII) galaxies, we fit each type separately, and find strong correlations between $L_{R,core}$ and $M_{*,bulge}$ and $M_{V,bulge}$. Note that the sample spans more than six orders of magnitude in stellar mass and over a dozen in absolute magnitude. The OLS bisector regressions that we fit to the $(L_{R,core}, M_{*,bulge})$ and $(L_{R,core}, M_{V,bulge})$ data set reveal that the $L_{R,core} - M_{*,bulge}$ and $L_{R,core} - M_{V,bulge}$ relations are not log-linear but instead active and inactive galaxies follow two distinct relations with markedly different slopes. The OLS bisector regression of our active galaxies yields $L_{R,core} \propto M_{*,bulge}^{1.42 \pm 0.18}$ and $L_{R,core} \propto L_{V,bulge}^{1.85 \pm 0.23}$, while we see substantial flattening of the trend for inactive galaxies $L_{R,core} \propto M_{*,bulge}^{0.68 \pm 0.08}$ and $L_{R,core} \propto L_{V,bulge}^{0.88 \pm 0.13}$. Note that our regression analyses did not take into account (accurately measured) $L_{R,core}$ and bulge properties, therefore we opted for a symmetrical bisector regression, rather than an OLS(X|Y) or OLS(Y|X) regression. The results of the regression fits are presented in Table 3. The transition from an inactive (i.e. star-formation driven) to an active optical AGN seems to

occur at $M_{*,bulge} \sim 10^{9.8 \pm 0.3} M_{\odot}$ and $M_{V,bulge} \sim -18.5 \pm 0.3$ mag. To assess the strength of the correlations, we use the Spearman and Pearson correlation coefficients (r_s , r_p , see Table 3). For the $L_{R,core} - M_{*,bulge}$ relations we find $r_s \sim 0.56 - 0.73$ and $r_p \sim 0.54 - 0.64$ and the pertaining P -values for a null hypothesis that two sets of data are uncorrelated are very low ($P \sim 10^{-14} - 10^{-7}$). The tight $L_{R,core} - M_{V,bulge}$ relations are such that $-r_s \sim 0.53 - 0.70$ and $-r_p \sim 0.53 - 0.64$ and $P \sim 10^{-13} - 10^{-7}$.

Given that 52 per cent of our sample do not have radio emission detected with e -MERLIN at 1.5 GHz and that our $L_{R,core}$ values for such undetected sources are upper limits, we performed a statistical censored analysis of the $L_{R,core} - M_{*,bulge}$ and $L_{R,core} - M_{V,bulge}$ relations using the ASURV package (Feigelson & Nelson 1985; Isobe, Feigelson & Nelson 1986) accounting for upper limits. The slopes from the censored and uncensored analyses are consistent within the errors ($L_{R,core} \propto M_{*,bulge}^{1.19 \pm 0.22}$ and $L_{R,core} \propto L_{V,bulge}^{1.33 \pm 0.30}$, for active galaxies, censored; $L_{R,core} \propto M_{*,bulge}^{0.74 \pm 0.17}$ and $L_{R,core} \propto L_{V,bulge}^{0.85 \pm 0.20}$, for inactive galaxies, censored). The slopes of the $L_{R,core} - M_{*,bulge}$ and $L_{R,core} - L_{V,bulge}$ relations for active and inactive galaxies are different, irrespective of the applied statistical method. There are however marked discrepancies between intercepts of the relations from the censored and uncensored analyses, in which the former intercepts have large errors and are markedly offset towards lower values. Despite the high level scatter at the low radio core luminosity end, the undetected radio sources which are mostly HII galaxies appear to be simply luminosity scaled-down versions of the radio detected inactive galaxies. However, three dwarf satellites of M31, the Andromeda Galaxy (NGC 147, NGC 205, and NGC 221, e.g. Ibata et al. 2013), which are all ALGs at a distance of 0.8 Mpc with $L_{R,core}$ upper limits (Baldi et al. 2018, 2021a), deviate notably from the inactive $L_{R,core} - M_{*,bulge}$ and $L_{R,core} - L_{V,bulge}$ relations. With the assumption that all ALGs follow the inactive $L_{R,core} - M_{*,bulge}$ and $L_{R,core} - L_{V,bulge}$ relations, a plausible interpretation is that the very low $L_{R,core}$ upper limit values of these low mass galaxies arise from an observational bias associated with their close proximity to us, which allowed very low $L_{R,core}$ values to be measured. An alternative interpretation for the lack of radio emission may be that the gravitational interaction of these three satellites with M31 has stripped them of their gas (see e.g. Putman et al. 2021), subsequently quenching star formation in the galaxies.

4.2 $L_{R,core} - M_{BH}$ and $L_{R,core} - \sigma$

We next examine the correlations between the radio core luminosity and the SMBH mass (M_{BH}) for those 59 LeMMINGS galaxies with measured M_{BH} (van den Bosch 2016; Nguyen et al. 2019, see Table A1), and the central stellar velocity dispersion (σ) for all 276 LeMMINGS galaxies with σ available from Ho et al. (2009); see Figs 9, 10, see Table A1. To measure the central velocity dispersions, Ho et al. (2009) used long-slit optical spectra placed across the nucleus of their galaxies with a rectangular aperture of size $2 \text{ arcsec} \times 4 \text{ arcsec}$ (Ho et al. 1995). The measured SMBH masses are based on the methods of gas dynamics, stellar dynamics, and megamasers, except for three galaxies (NGC 3516, NGC 5273, and NGC 5548) with reverberation mapping SMBH masses.

The $L_{R,core} - M_{BH}$ relation is regarded as a good diagnostic to separate star-forming and AGN galaxies (e.g. Nagar et al. 2002; Baldi et al. 2018; Saikia et al. 2018). Brighter and more massive galaxies which host massive BHs are associated with radio emission from the AGN as reflected by the trend of increasing AGN fraction with SMBH mass, whereas at low luminosities/masses the radio

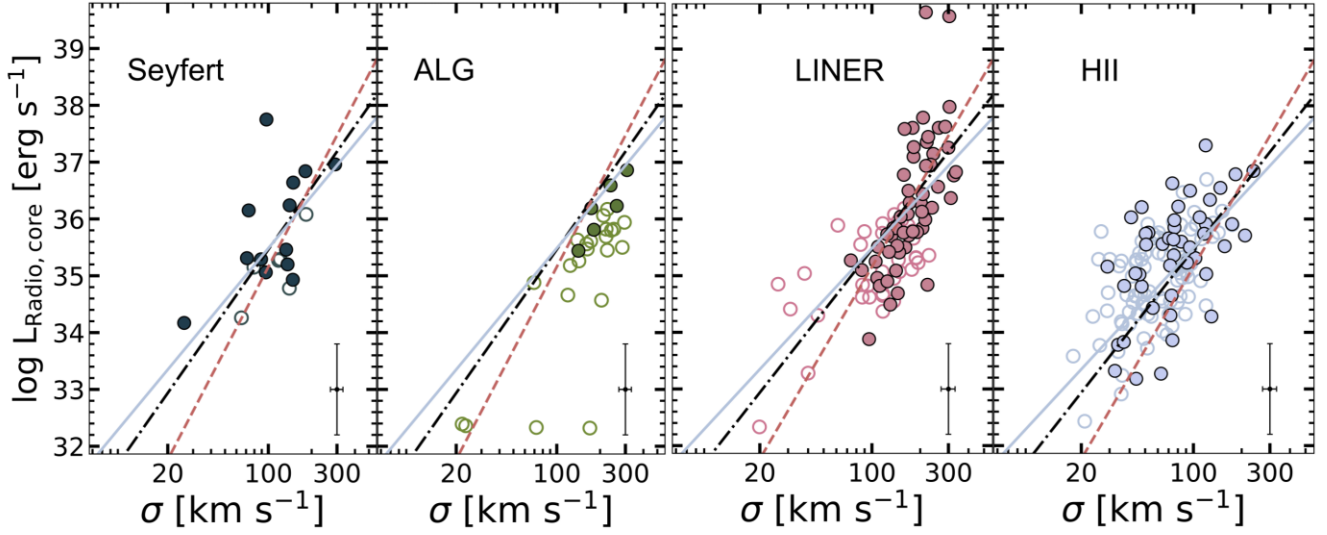


Figure 10. The radio core luminosity ($L_{R, \text{core}}$) as a function of the central stellar velocity dispersion (σ) for all 276 LeMMINGs galaxies with σ available from Ho et al. (2009). Symbolic representations are as in Fig. 7. The dashed, solid, and dashed-dotted lines are OLS bisector fits for the active, inactive, and full sample of galaxies under consideration. NGC 1275 falls outside the range radio core luminosity shown here. A typical error bar associated with the data points is shown at the bottom of each panel.

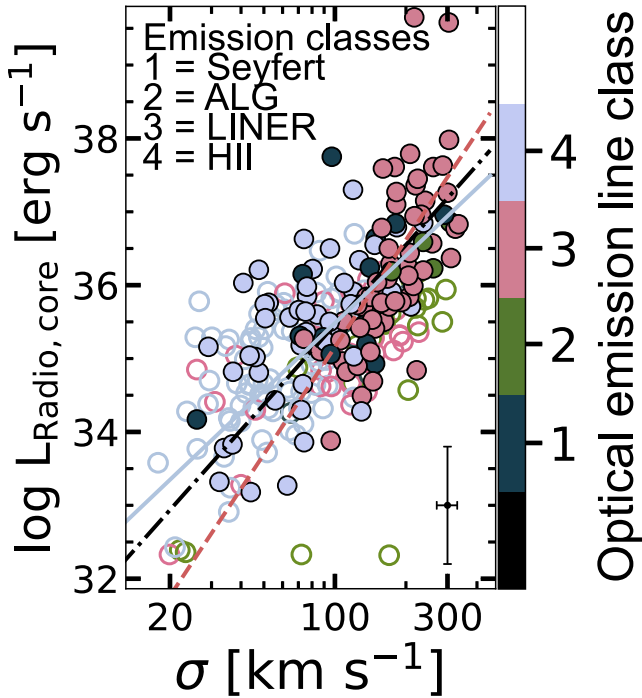


Figure 11. Similar to Fig. 10 but now showing the spectral classes together for ease of comparison. A typical error bar is shown at the bottom right.

emission is primarily due to star formation. The 59 SMBH masses, although securely measured, are fairly high. With only 12/59 SMBHs less massive than $M_{\text{BH}} \sim 10^{6.5} M_{\odot}$, the presence of two distinct relations for active and inactive galaxies is not evident from the $L_{R, \text{core}} - M_{\text{BH}}$ diagram (Fig. 9), therefore we have not sought to separate the galaxies into these two groups. In Baldi et al. (2018, 2021a) we reported ‘broken’ scaling relations involving L_{core} and M_{BH} with distinct slopes which correspond to non-jetted star-forming ($\sim L_{\text{core}} \propto M_{\text{BH}}^{0.61}$) and active galaxies ($\sim L_{\text{core}} \propto M_{\text{BH}}^{1.65}$), the break occurring at $M_{\text{BH}} \sim 10^{6.5} M_{\odot}$; the bulk (221/280) of the Baldi et al.

(2018, 2021a) galaxies had their SMBH masses predicted using the $M - \sigma$ relation. In Fig. 9 we refrain from using SMBH masses predicted with well-known SMBH scaling relations (e.g. $M_{\text{BH}} - \sigma$, $M_{\text{BH}} - L_{\text{bulge}}$, and $M_{\text{BH}} - M_{*, \text{bulge}}$) because departures from a single power-law relation between M_{BH} and host galaxy properties have been reported to exist particularly at the low- and high-mass ends (e.g. Greene, Ho & Barth 2008; McConnell & Ma 2013; Bower et al. 2017; Martín-Navarro & Mezcua 2018; Dullo, Gil de Paz & Knapen 2021). We find that the OLS bisector fit gives the relation between $L_{R, \text{core}}$ and M_{BH} as $L_{R, \text{core}} \propto M_{\text{BH}}^{1.45 \pm 0.20}$ ($r_s/P \sim 0.52/2.6 \times 10^{-5}$ and $r_p \sim 0.57/2.3 \times 10^{-6}$), Table 3.

In the $L_{R, \text{core}} - \sigma$ diagram (Figs 10, 11), H II galaxies, galaxies with LINER, Seyferts nuclei, and ALGs cleanly separate into two sequences. For a given radio core luminosity, H II galaxies seem to possess lower central velocity dispersions than LINERs, Seyferts, and ALGs. We note that H II galaxies are likely to contain a low-dispersion disc component which may reduce the measured σ values. However, Ho et al. (2009) measured σ using the spectra of the central regions of the galaxies typically dominated by the bulge. Furthermore, Marsden et al. (2022) reported weak dependence of σ on disc component. On the other hand, we find ALGs do not deviate from the best-fitting inactive $L_{R, \text{core}} - \sigma$ relation defined by the H II+ALG subsample, but they reside almost exclusively under this relation.

We therefore fit OLS bisector regressions first by splitting the sample into active and inactive galaxies and then using the sample of 276 LeMMINGs galaxies. The OLS fits yield the relations between $L_{R, \text{core}}$ and σ such that $L_{R, \text{core}} \propto \sigma^{4.85 \pm 0.58}$ ($r_s/P \sim 0.72/7.9 \times 10^{-19}$ and $r_p \sim 0.66/2.8 \times 10^{-15}$), $L_{R, \text{core}} \propto \sigma^{3.06 \pm 0.23}$ ($r_s/P \sim 0.59/7.9 \times 10^{-16}$ and $r_p \sim 0.56/1.2 \times 10^{-14}$) and $L_{R, \text{core}} \propto \sigma^{3.61 \pm 0.24}$ ($r_s/P \sim 0.65/7.2 \times 10^{-35}$ and $r_p \sim 0.64/2.9 \times 10^{-33}$) for active, inactive, and combined sample galaxies, respectively (Table 3). Our censored $L_{R, \text{core}} - \sigma$ relations are $L_{R, \text{core}} \propto \sigma^{5.10 \pm 0.60}$, $L_{R, \text{core}} \propto \sigma^{2.75 \pm 0.48}$, and $L_{R, \text{core}} \propto \sigma^{3.97 \pm 0.34}$ for active, inactive, and combined sample galaxies, respectively (Table 3). As noted above, while the slopes from the censored and uncensored analyses agree within the errors, the intercepts of the relations are

different. The transition from a steep $L_{R, \text{core}} - \sigma$ relation for optical AGN galaxies to the less steep, inactive $L_{R, \text{core}} - \sigma$ relation happens at $\sigma \sim 85 \pm 5 \text{ km s}^{-1}$.

Figs 7, 9, and 10 reveal an outstanding outlier NGC 1275. This LINER galaxy is 2.5–3.8 dex (in the $\log L_{R, \text{core}}$ direction) above the $L_{R, \text{core}} - M_{*, \text{bulge}}$, $L_{R, \text{core}} - L_{V, \text{bulge}}$, $L_{R, \text{core}} - \sigma$, and $L_{R, \text{core}} - M_{\text{BH}}$ best-fitting lines. Given that NGC 1275 is offset upward in several $L_{R, \text{core}}$ scaling diagrams, the most favoured interpretation is that the radio core luminosity is higher than expected. We note the level of scatter pertaining to the $L_{R, \text{core}}$ scaling relations of 0.80–1.0 dex (in the $\log L_{R, \text{core}}$ direction). For comparison, the typical uncertainty on $\log L_{R, \text{core}}$ is ~ 1 dex.

5 DISCUSSION

5.1 Is the $L_{R, \text{core}} - M_{\text{BH}}$ relation broken?

We have shown previously unreported breaks in the slopes of the observed $L_{R, \text{core}} - M_{*, \text{bulge}}$, $L_{R, \text{core}} - M_{V, \text{bulge}}$, and $L_{R, \text{core}} - \sigma$ relations when the sample includes active and inactive galaxies (Sections 4.1, 4.2, and Table 3). The slopes of these $L_{R, \text{core}}$ scaling relations for galaxies whose radio emission is dominated by AGN are steeper than those for star formation dominated galaxies, with the breaks occurring at $M_{*, \text{bulge}} \sim 10^{9.8 \pm 0.3} M_{\odot}$, $M_{V, \text{bulge}} \sim -18.5 \pm 0.3$ mag, and $\sigma \sim 85 \pm 5 \text{ km s}^{-1}$. We have interpreted the broken $L_{R, \text{core}}$ scaling relations as being due to differences in the origin of nuclear radio emissions for AGN and star forming galaxies (Fiore et al. 2017; Baldi et al. 2018, 2021a, b). Our motivation here is twofold: (i) examine if the single (log-linear) $L_{R, \text{core}} - M_{\text{BH}}$ relation (Fig. 9) is internally consistent with other $L_{R, \text{core}}$ scaling relations and (ii) examine if it holds for all galaxies. As noted above, Baldi et al. (2021b) reported a break in the $L_{R, \text{core}} - M_{\text{BH}}$ relation at $M_{\text{BH}} \sim 10^{6.5} M_{\odot}$ for the full sample of 280 LeMMINGs galaxies, analogous to the aforementioned breaks (Sections 4.1 and 4.2); in that work the SMBH mass for 221 LeMMINGs galaxies were predicted from the $M_{\text{BH}} - \sigma$ relation (Tremaine et al. 2002). Combining our single (log-linear) $L_{R, \text{core}} - M_{\text{BH}}$ relation constructed using 59 measured M_{BH} with the $L_{R, \text{core}} - M_{*, \text{bulge}}$, $L_{R, \text{core}} - L_{V, \text{bulge}}$, and $L_{R, \text{core}} - \sigma$ relations (Table 3), we find the mass, luminosity, and velocity dispersion turnovers given above (that marks the transition from star formation to AGN) correspond to an SMBH mass of $M_{\text{BH}} \sim 10^{6.8 \pm 0.3} M_{\odot}$. This suggests that breaks in the different $L_{R, \text{core}}$ scaling relations are related and that the break we identified in the $L_{R, \text{core}} - M_{\text{BH}}$ relation (Baldi et al. 2021b) may be a consequence of a broken $L_{R, \text{core}} - \sigma$ relation. As such a single $L_{R, \text{core}} - M_{\text{BH}}$ relation can hold over the entire radio core luminosity range, although our results do not preclude a broken $L_{R, \text{core}} - M_{\text{BH}}$ relation. To ascertain the universality of the $L_{R, \text{core}} - M_{\text{BH}}$ relation more directly measured SMBHs for our sample with $M_{\text{BH}} \lesssim 10^{6.5} M_{\odot}$ are needed.

5.2 The influence of environment on AGN activity and the importance of bulge mass

Our results have revealed no evidence for environmental effects on the AGN activity. Across a small range in bulge mass, we find no significant dependence of the radio core luminosity, radio loudness, nuclear radio activity, or AGN fraction (both optical and radio) on environmental metrics and halo mass (Fig. 4). Our work is consistent with a growing body of literature (Laurikainen & Salo 1995; Carter et al. 2001; Miller et al. 2003; Knapen 2004; von der Linden et al. 2010; Pimblet et al. 2013; Amiri et al. 2019; Man et al. 2019; Mishra, Dai & Guerras 2021), and the results favour a scenario

in which the AGN activity is largely bulge mass dependent (see Section 5.3; also Miller et al. 2003; Bluck et al. 2014; Magliocchetti et al. 2020). We recall that radio loudness, the radio detection fraction, and the fraction of galaxies hosting optical (emission-line) AGN and/or radio AGN are strong functions of the bulge stellar mass and luminosity, $M_{*, \text{bulge}}$, $M_{V, \text{bulge}}$ (see Sections 3.2–3.6; also Dunlop et al. 2003; Best et al. 2005; Pimblet et al. 2013). We have also shown that the radio core luminosity scales strongly with $M_{*, \text{bulge}}$ and $M_{V, \text{bulge}}$. These observed relations are ascribed here to a formation scenario in which bulges and their SMBHs evolve together in lockstep (e.g. Ho 2002; Nagar et al. 2002; Nagar et al. 2005; Heckman & Best 2014). Galaxies with more massive bulges harbour massive SMBHs efficient at generating strong AGN-driven outflows and radio emissions, which consequently blow away gas and produce lower star formation efficiencies (e.g. Silk & Rees 1998; Croton et al. 2006; Hopkins et al. 2006; Lagos, Cora & Padilla 2008). The very deep central potential in the bulges of massive galaxies also help retain the hot X-ray-emitting interstellar medium (ISM) that is being kept hot by the energy from the radio jet (e.g. Tabor & Binney 1993; McNamara & Nulsen 2007; Cattaneo et al. 2009; Kormendy et al. 2009; Fabian 2012; Heckman & Best 2014). In contrast, low-mass bulges with a shallow potential well likely undergo a weak AGN activity and stellar feedback (Silk 2005). Finally, we note that the so-called morphology–density relation (Dressler 1980) is such that elliptical and early-type disc galaxies, apart from hosting more powerful AGN, live in denser environments. Therefore this relation could give rise to an apparent link between the AGN and host galaxy environment.

5.3 Implications for host galaxy formation mechanisms

We now discuss the observed connections between the stellar mass, optical spectral line and radio continuum emission, and the potential implications for the formation of core-Sérsic, Sérsic, Seyfert, LINER and H II galaxies, and ALGs. We focus on the bulge mass $M_{*, \text{bulge}}$ which is a powerful predictor of galaxy properties such as Hubble type, n , B/T , σ , and M_{BH} .

5.3.1 Core-Sérsic galaxies

Core-Sérsic galaxies have depleted cores (Graham et al. 2003; Trujillo et al. 2004; Ferrarese et al. 2006; Kormendy et al. 2009; Dullo & Graham 2012, 2013; Rusli et al. 2013; Dullo & Graham 2014; Dullo, Graham & Knapen 2017; Dullo 2019; Krajnović et al. 2020) and are thought to be built up through one or more successive ‘dry’ (gas-poor) mergers involving SMBHs (Begelman et al. 1980; Ebisuzaki et al. 1991; Faber et al. 1997; Milosavljević & Merritt 2001; Merritt 2006). They have high radio luminosities ($L_{R, \text{core}} \gtrsim 10^{35} \text{ erg s}^{-1}$) and represent 11.6 per cent (20/173) of our sample. They are massive ($M_{*, \text{bulge}} \gtrsim 10^{11} M_{\odot}$) and bulge-dominated early-type galaxies hosting either LINER- or ALG-type nuclear emission, although one exception which has an H II nucleus is the S0 NGC 3665. Most (65 per cent) of the core-Sérsic galaxies in the sample are radio-detected. In Dullo et al. (2023) we revealed that core-Sérsic galaxies tend to be systematically radio-loud and round ($\epsilon = 0.21 \pm 0.08$). They also show a tendency to have ‘boxy’ distorted or pure elliptical (i.e. neutral) isophotes ($B_4 = (-0.007 \pm 0.08) \times 10^{-2}$), confirming past work (e.g. Sandage 1965; Hummel, Kotanyi & Ekers 1983; Disney, Sparks & Wall 1984; Wrobel & Heeschen 1991; Sadler et al. 1995; Faber et al. 1997; Capetti & Balmaverde 2005; Balmaverde & Capetti 2006; Richings et al. 2011; Dullo & Graham

2015; Dullo et al. 2018). Our results here also confirm that most (90 per cent) slow-rotators are core-Sérsic galaxies (see Krajnović et al. 2013; Veale et al. 2017a).

Despite both core-Sérsic LINERs and ALGs having large bulge masses, high bulge luminosities, high n values ($\gtrsim 4$) and similar inner profile slopes ($\gamma \lesssim 0.3$) and B_4 values, there is a significant difference in the radio detection fraction for the two types, i.e. 9/11 (82 per cent) and 3/8 (38 per cent), respectively. We attribute these results as being associated with the level of gas accretion onto the SMBH (or lack thereof). In light of the *HST* structural analysis and radio emission analysis, we postulate that core-Sérsic galaxies with LINER nuclei likely involve fuelling gas for the AGN (in hot accretion mode, e.g. Best et al. 2007; Cattaneo et al. 2009; Gendre et al. 2013) and some low-level, residual star formation (see Fig. 6), whereas the growth of core-Sérsic ALGs (most of which are ellipticals and thus do not have a supply of cold gas) may largely involve a simple addition of stars and little gas (e.g. Faber et al. 1997; Hopkins et al. 2009b). The cooling of hot gas and/or accretion of a gas-rich satellite are mechanisms through which massive early-type galaxies and brightest cluster galaxies (BCGs) can acquire cold gas, allowing for episodes of low-level star formation (e.g. Salomé & Combes 2003; O’Dea et al. 2008; Kaviraj 2010; Young et al. 2011; Russell et al. 2014; Smith & Edge 2017). An alternative interpretation compatible with the lack of nuclear activity in massive ALGs is an intermittent gas accretion of the AGN that leads to short-lived AGN episodes, namely the recurrence scenario (e.g. Schawinski et al. 2015; Morganti 2017).

For core-Sérsic LINER galaxies, the stronger AGN feedback from their massive SMBHs can generate high nuclear radio emission, explaining why they trace the high-mass end of the steeper $L_{R,\text{core}}$ scaling relations, in contrast to core-Sérsic ALGs which lie below their LINER counterparts on the inactive relations. In Dullo et al. (2020) we have demonstrated such core-Sérsic galaxies are red but not strictly dead (see de La Rosa et al. 2011; Davis et al. 2019). With UV fluxes being detectable by *GALEX* (Fig. 6), core-Sérsic LINER galaxies fall on the high-mass end of the tight (SMBH mass)-(UV-[3.6] colour) red sequence which is populated by older bulges with more massive SMBHs. Within the core-Sérsic LINER galaxy formation scenario, any residual star formation has to be kept at low level by the AGN feedback, otherwise a substantial late-time gas inflow and subsequent starburst events would regenerate a Sérsic galaxy after having replenished any pre-existing depleted core scoured by binary SMBHs. Radio jets are invoked to inject energy as an additional source of heating to prevent the hot X-ray gas from cooling and to maintain radio-mode feedback episodes (e.g. Best et al. 2006; Croton et al. 2006; McNamara & Nulsen 2007; Sijacki et al. 2007; Somerville et al. 2008; Cattaneo et al. 2009; McNamara et al. 2009, 2011; Fabian 2012; Heckman & Best 2014; Venturi et al. 2021) in the most massive early-type galaxies and BCGs which reside in groups and clusters (e.g. O’Dea et al. 2008; Russell et al. 2014; Smith & Edge 2017; Russell et al. 2019). Of the 20 core-Sérsic galaxies in our sample, four (20 per cent) indeed display clear evidence for such radio jets.

5.3.2 Sérsic galaxies

Sérsic galaxies make up ~ 88 per cent (153/173) of our sample. They are core-less and span a wide range in radio luminosities ($L_{R,\text{core}} \sim 10^{32} - 10^{40}$ erg s $^{-1}$). Sérsic bulges exhibit a large γ range, from 0.01 to 0.70, and the vast majority (~ 87 per cent) of them have $M_{*,\text{bulge}} \lesssim 10^{11} M_{\odot}$. They are associated with all optical emission classes and have a radio detection fraction (46 per cent) lower than their core-Sérsic counterparts (65 per cent), unsurprising given that

radio detection increases with increasing bulge stellar mass. The fraction of Sérsic galaxies that are jetted is ~ 12 per cent, lower than that for core-Sérsic galaxies (20 per cent). All but one of the Seyferts and H II hosts are Sérsic galaxies; the only exception, NGC 3665, is mentioned above. Sérsic bulges grow primarily via gas-rich processes (gas-rich mergers and secular evolution), accompanied by cold gas dissipation and starbursts in the nuclear region (Faber et al. 1997; Hopkins et al. 2009a). Their stellar populations are formed over a protracted period of time (Thomas et al. 2005; Tolstoy, Hill & Tosi 2009; Thomas et al. 2010; de La Rosa et al. 2011; McDermid et al. 2015).

5.3.3 Seyferts

All ten Seyferts in the sample are Sérsic galaxies and overall have intermediate-mass bulges ($10^{10} - 10^{11} M_{\odot}$) which are similar to those for the Sérsic ALGs and intermediate-mass Sérsic LINERs. Over this mass range, 88 per cent of Seyferts and 75 per cent of Sérsic LINER galaxies have radio detections, in contrast with the low detection rate found for ALGs (9 per cent). Having their $M_{*,\text{bulge}}$, $M_{V,\text{bulge}}$, and σ correlated well with $L_{R,\text{core}}$, Seyfert galaxies unite with LINERs to jointly define the active $L_{R,\text{core}} - M_{*,\text{bulge}}$, $L_{R,\text{core}} - M_{V,\text{bulge}}$, and $L_{R,\text{core}} - \sigma$ sequences. These results suggest an AGN origin for the radio emission in Seyfert galaxies. The key difference between Seyferts and intermediate-mass Sérsic LINERs is their Hubble type; most (70 per cent) Seyferts are spiral galaxies, while the latter bifurcate into 57 per cent spirals and 43 per cent S0s. Our observations suggest that, in their late evolution, Seyfert bulges probably have undergone major, gas-rich mergers, and possibly gas-rich accretion events (e.g. Hopkins & Hernquist 2009; Hopkins et al. 2009a; Shankar et al. 2012), which are gentler than the very violent major merger events that core-Sérsic and massive Sérsic galaxies are formed (e.g. Naab, Khochfar & Burkert 2006; Hopkins et al. 2009b). Hopkins & Hernquist (2006, 2009) suggested the accretion of cold gas stochastically onto a central SMBH for fuelling low mass ($M_{*,\text{bulge}} \lesssim 10^{10} M_{\odot}$ and $M_{\text{BH}} \lesssim 10^7 M_{\odot}$) Seyferts. The same cold accretion mode may account for our intermediate-mass Seyfert galaxies (Hopkins & Hernquist 2006). In Dullo et al. (2020) we highlighted that early- and late-type galaxies define a red and blue (SMBH mass)-colour sequence, attributed to two distinct channels of SMBH growth for the two Hubble types (e.g. Chen et al. 2020). Within this picture, the formation and SMBH growth of Seyfert galaxies, most of which are late-type galaxies, are likely to involve a higher level of nuclear activity than their LINER counterparts due to the increased gas availability for enhanced feeding of their SMBHs. This is also evident from their high radio detection rate.

5.3.4 Absorption line galaxies

ALGs are commonly regarded to lack nuclear activity (Baldi et al. 2018, and references therein). While a full understanding of their nature is lacking, the inactivity in some ALGs can be due to a strong, internal dust obscuration that diminishes a weakly active SMBH (Goulding & Alexander 2009; Aalto et al. 2015). Of the 23 ALGs in the sample, eight are core-Sérsic galaxies and the remaining 15 are Sérsic galaxies. As noted in Section 5.3.1, our core-Sérsic ALGs have large bulge masses ($M_{*,\text{bulge}} \gtrsim 10^{11} M_{\odot}$). This implies massive SMBHs ($M_{\text{BH}} \gtrsim 5 \times 10^8 M_{\odot}$), considering the mutual growth of SMBHs and galaxies, i.e. the $M_{\text{BH}} - M_{*,\text{bulge}}$ correlation (e.g. McLure & Dunlop 2002) but core-Sérsic ALGs appear to have low radio detection rates (38 per cent) for their large bulge and SMBH masses. Sérsic ALGs consist of low mass, local dwarfs ($M_{*,\text{bulge}} \lesssim 10^{10} M_{\odot}$), and intermediate mass

($M_{*,\text{bulge}} \sim 10^{10} - 10^{11} M_{\odot}$) lenticular and elliptical galaxies. Together with H II bulges, not only do the ALG bulges define the inactive $L_{R,\text{core}} - M_{*,\text{bulge}}$, $L_{R,\text{core}} - M_{V,\text{bulge}}$, and $L_{R,\text{core}} - \sigma$ sequences, but they also typically populate the high mass end of the relations. Note that all 23 ALGs are early-type galaxies, the bulk (13/23) of which are elliptical galaxies. They appear to have lower radio emission than Seyferts and LINERs over the same $M_{*,\text{bulge}}$, $M_{V,\text{bulge}}$, and σ ranges. Therefore, it seems reasonable to posit a gas-poor formation origin for ALGs, gas dissipation being less important for them than for any other emission line class. One ALG (NGC 3348) clearly exhibits a radio jet suggestive of an active AGN, conflicting with the optical emission-line classification. ALG bulges, when treated as a whole, their early-type morphology and the position on the $L_{R,\text{core}}$ scaling relations points towards growth being dominated by gas-poor processes. For the massive and intermediate-mass ALGs, our observations favour gas-poor mergers as the formation path, which starve the massive SMBHs and give rise to very weak AGN accretion activity (Baldi et al. 2018, 2021a, b), whereas for the low mass ALGs, environmental processes such as tidal stripping (Gunn & Gott 1972) could account for the removal of gas from the galaxy (Ricotti & Gnedin 2005) explaining the low nuclear radio emissions from the low mass BHs. As noted above, massive ALGs may be due to an intermittent gas accretion of the AGN.

5.3.5 LINERs

LINERs are among the most massive galaxies in the sample. They have high incidence of radio detection and brighter radio core luminosities. They split nearly evenly between early-type (51 per cent) and late-type (49 per cent) morphologies and show a large range in mass. As noted above, they unite with Seyfert galaxies and jointly follow the active $L_{R,\text{core}}$ scaling relations. Of the 71 LINERs in our sample, 12 are core-Sérsic galaxies ($M_{*,\text{bulge}} \gtrsim 10^{11} M_{\odot}$), 14 massive Sérsic galaxies ($M_{*,\text{bulge}} \gtrsim 10^{11} M_{\odot}$), 31 intermediate-mass Sérsic galaxies ($M_{*,\text{bulge}} \sim 10^{10} - 10^{11} M_{\odot}$), and 15 low-mass Sérsic galaxies ($M_{*,\text{bulge}} \lesssim 10^{10} M_{\odot}$). As discussed above, the properties of the core-Sérsic LINER galaxies are reproduced by gas-poor major merger events that involve low-level, residual star formation, and gas fuelling for the AGN. We find radio-loud LINERs, which are known to behave like radio galaxies (e.g. Baldi et al. 2018, 2021a, b), typically sit on the red-sequence in the (FUV-[3.6])– $M_{*,\text{bulge}}$ plane. Massive Sérsic LINERs and core-Sérsic LINERs show similar $M_{*,\text{bulge}}$, $L_{R,\text{core}}$, σ and radio detection fractions, and the Sérsic index values for the two types agree within the errors ($n_{\text{Massive_Ser_LINER}} = 3.22 \pm 0.84$, $n_{\text{coreSer_LINER}} = 4.23 \pm 1.22$). Furthermore, the former are hosted mainly by S0s (40 per cent) and spiral galaxies (43 per cent), while the latter are largely associated with elliptical galaxies (82 per cent). Although our analysis supports a dissipative major merger scenario as a formation path for Sérsic LINERs with massive bulges (Faber et al. 1997; Hopkins et al. 2009a), an alternative mechanism is the rejuvenation of a core-Sérsic galaxy by recent nuclear star formation which erases the depleted core (e.g. Thomas et al. 2010; Chauke et al. 2019).

Our results indicate that intermediate-mass Sérsic LINERs which exhibit similarities with Seyfert galaxies are a lower mass extension of the Sérsic LINERs populating the massive end. Collectively, our observations are well reconciled with predominantly AGN-driven radio emission for LINER galaxies with intermediate-to-massive bulges. Low-mass LINER and H II galaxies appear indistinguishable in terms of $L_{R,\text{core}}$, n , and Hubble type, although the former show slightly higher radio detection fraction (40 ± 19 per cent) than

the latter (21 ± 7 per cent) within the errors. Consequently, the formation of low-mass, LINER bulges, akin to their H II analogues, likely involves non-merger mechanisms, e.g. secular processes driven by non-axisymmetric stellar structures (e.g. Schawinski et al. 2011; Simmons et al. 2013).

5.3.6 H II galaxies

Of the 69 H II galaxies in the sample, 68 are Sérsic, the only core-Sérsic H II galaxy is NGC 3665. The majority (80 per cent) of the H II galaxies have low-mass bulges ($M_{*,\text{bulge}} \lesssim 10^{10} M_{\odot}$). The remaining 20 per cent possess intermediate-mass bulges ($M_{*,\text{bulge}} \sim 10^{10} - 10^{11} M_{\odot}$), except for one galaxy (NGC 3665) whose bulge is extremely massive ($M_{*,\text{bulge}} \sim 10^{12.5} M_{\odot}$). In fact, NGC 3665 and NGC 4217 are the two H II galaxies in our sample having a clear ‘jet-like’ radio structure, while for another two H II galaxies with intermediate masses (NGC 2782, and NGC 3504) their jet morphology is less secure. As expected, all our bulge-less galaxies harbour H II nuclei. The low-mass H II galaxies (98 per cent of which are late-type galaxies) exhibit a low radio detection fraction of 12/55 (21.8 per cent), compared with a higher detection fraction of 10/15 (64 per cent) for the higher mass bin (which consists of 79 per cent late-types and 21 per cent early-types). H II galaxies and ALGs are described jointly by the inactive $L_{R,\text{core}} - M_{*,\text{bulge}}$, $L_{R,\text{core}} - M_{V,\text{bulge}}$ and $L_{R,\text{core}} - \sigma$ correlations, although upper limit $L_{R,\text{core}}$ values are used for 67.6 per cent of the H II galaxies. Despite both being categorized as inactive, ALGs and H II galaxies have a crucial distinction: ALGs are associated with gas-poor processes and weakly active (or fully switched off) AGN, while the H II galaxies, particularly at the low-mass end, which likely contain high molecular gas fractions, are consistent with their nuclear radio emission being generated mainly by star formation (Baldi et al. 2018, 2021a, b).

Intermediate-mass H II bulges appear indistinguishable from similar-mass Seyfert and LINER bulges in terms of radio detection fraction, $L_{R,\text{core}}$, $M_{V,\text{bulge}}$, n , and location on the $L_{R,\text{core}}$ scaling diagrams, but the former contain slightly more late-type galaxies (85 ± 35 per cent) than the latter two (70 ± 40 per cent and 57 ± 17 per cent, respectively). At intermediate masses, the growth of H II bulges might be dominated by gas-rich major merger events, but it is unclear whether the nuclear radio emission has an AGN or a star formation origin. For the low-mass H II galaxies, the high-level of star formation is generally the main source of energy for the nuclear radio emission, dominating over the low-mass BH activity (e.g. Anglés-Alcázar et al. 2017). For such galaxies, the bulge growth scenario is through secular evolution (e.g. Kormendy 1993; Kormendy & Kennicutt 2004; Kormendy & Ho 2013), where gravitational torques induced by non-axisymmetric stellar structures such as bars and spirals drive the rearrangement of disc material by channeling it from the large-scale disc into the nuclear region (Shlosman et al. 1989; Athanassoula 1992; Knapen et al. 1995; Englmaier & Shlosman 2000; García-Burillo et al. 2005; Anglés-Alcázar et al. 2021), fuelling star formation at the centre and slowly feeding the low mass BH, $M_{\text{BH}} \sim 10^4 - 10^6 M_{\odot}$ (Greene et al. 2010; Jiang, Greene & Ho 2011; Schawinski et al. 2011; Kocevski et al. 2012; Simmons et al. 2013). Indeed, 41 (59 per cent) of our H II galaxies are classified as barred in the Third Reference Catalogue, RC3 (de Vaucouleurs et al. 1991).

6 SUMMARY AND CONCLUSIONS

The main goal of this work has been to investigate the nuclear activity in 173 LeMMINGS galaxies (23 Es, 42 S0s, 102 Ss, and

6 Irrs) both in the optical and radio at sub-arcsec resolutions, and in so doing highlight the role of the bulge in dictating the AGN activity and star formation events in nearby galaxies. Given that most LeMMINGs galaxies are low-luminosity AGN, we use our 1.5 GHz, high-sensitivity and high angular resolution *e*-MERLIN radio observations (Baldi et al. 2018, 2021a, b). These allowed for accurate identification of the AGN, singling out any potential contamination from star formation. This is coupled with accurate photometric and structural parameters, luminosities, and stellar masses for the bulge components and the full galaxies, which we determined from detailed, multicomponent decompositions of high-resolution *HST* surface brightness profiles, fitting simultaneously up to six galaxy components, e.g. bulges, discs, depleted core, AGN, nuclear star clusters, bars, spiral arms, rings, and stellar haloes (Dullo et al. 2023). These complementary LeMMINGs studies provided bulge stellar masses and radio core luminosities that span wide ranges of $M_{*,\text{bulge}} \sim 10^6 - 10^{12.5} M_{\odot}$ and $L_{R,\text{core}} \sim 10^{32} - 10^{40} \text{ erg s}^{-1}$. They represent, to date, the most comprehensive radio and optical view of the connection between galactic nuclei and bulges in the nearby Universe. We have also quantified the galaxy environment using two approaches: halo mass and local luminosity surface densities measured within the 3rd and 10th nearest neighbour of the target galaxy (ν_3 and ν_{10}). There are 140 galaxies in common between the full LeMMINGs and *GALEX/S*⁴G (Bouquin et al. 2018) samples. We first separate these overlapping galaxies into red sequence, blue sequence, and green valley objects using the *GALEX/S*⁴G colour-colour diagrams (Bouquin et al. 2018) and then located them on the (FUV-[3.6])– $M_{*,\text{bulge}}$ diagrams.

We find the following:

(1) The radio detection fraction increases with bulge mass $M_{*,\text{bulge}}$ and Sérsic index n . At $M_{*,\text{bulge}} \gtrsim 10^{11} M_{\odot}$, the radio detection fraction is 77 per cent, declining to 24 per cent for $M_{*,\text{bulge}} < 10^{10} M_{\odot}$. Radio-jetted sources are hosted by the more massive galaxies over a mass range of $M_{*,\text{bulge}} \sim 3.0 \times 10^9 - 3.2 \times 10^{12} M_{\odot}$ and a median mass of $M_{*,\text{bulge}} \sim 6.0 \times 10^{10} M_{\odot}$.

(2) We confirm that the fraction of galaxies harbouring emission-line AGN and/or radio AGN is a strong function of $M_{*,\text{bulge}}$ and $M_{V,\text{bulge}}$, although the correlations are less constrained for the radio AGN. The majority of AGN (80 per cent) and radio AGN (90 per cent) hosts have $M_{\text{bulge}} \gtrsim 10^{10} M_{\odot}$ ($M_{\text{glxy}} \gtrsim 10^{10.5} M_{\odot}$). None of our 10 bulge-less galaxies host an AGN. The fraction of AGN galaxies is such that $f_{\text{optical,AGN}} \propto M_{*,\text{bulge}}^{0.24 \pm 0.06}$ and $f_{\text{optical,AGN}} \propto M_{*,\text{glxy}}^{0.30 \pm 0.05}$. The radio AGN fraction scales as $f_{\text{radio,AGN}} \propto M_{*,\text{bulge}}^{0.24 \pm 0.05}$ and $f_{\text{radio,AGN}} \propto M_{*,\text{glxy}}^{0.41 \pm 0.06}$, markedly different from that reported for the host of radio-loud galaxies by Best et al. (2005, $f_{\text{radio,loud}} \propto M_{*,\text{glxy}}^{2.5}$). For low-mass galaxies ($M_{*,\text{glxy}} \lesssim 5 \times 10^9 M_{\odot}$), we find an AGN fraction of 9.4 per cent in agreement with the 10 per cent reported by Penny et al. (2018).

(3) Overall, there are only weak correlations between the radio core luminosity ($L_{R,\text{core}}$) and luminosity surface density (ν) ($r_s \sim 0.13 - 0.20$, $P \sim 0.01231 - 0.0924$). The relation between $L_{R,\text{core}}$ and halo mass (M_{halo}) is consistent with the null hypothesis of no correlation ($r_s \sim -0.07$, $P \sim 0.3811$). While the median radio core luminosities for our sample appear to increase slightly as a function of ν , our galaxies reside in all environments, regardless of their $L_{R,\text{core}}$.

(4) At fixed bulge mass, our results are compatible with no significant dependence of the radio core luminosity, radio loudness, nuclear radio activity, and AGN (both optical and radio) fraction on environmental metrics (i.e. including halo mass).

(5) Compared to RQ hosts, RL hosts preferentially possess an early-type morphology and inhabit a denser environment as defined

by ν_3 . While there is a mild tendency for RL galaxies to have shallower inner logarithmic slopes (γ) than RQ galaxies, the KS test on the γ distributions for RQ and RL galaxies with $P \sim 0.05$ is a borderline case. Having performed KS tests on the data sets for galaxy properties n , ellipticity, B_4 , ν_{10} , and M_{halo} , the null hypothesis that the RQ and RL galaxies are drawn from identical distributions cannot be rejected (P -values $\sim 0.10 - 0.54$).

(6) $L_{R,\text{core}}$ scales with $M_{*,\text{bulge}}$, $L_{V,\text{bulge}}$, σ , and M_{BH} . We find hitherto unreported breaks in the $L_{R,\text{core}} - M_{*,\text{bulge}}$, $L_{R,\text{core}} - L_{V,\text{bulge}}$, and $L_{R,\text{core}} - \sigma$ relations for data sets including upper limits. These turnovers, which separate AGN and star formation dominated radio emissions occur at $M_{*,\text{bulge}} \sim 10^{9.8 \pm 0.3} M_{\odot}$ and $M_{V,\text{bulge}} = -18.5 \pm 0.3 \text{ mag}$, $\sigma = 85 \pm 5 \text{ km s}^{-1}$ and $M_{\text{BH}} = 10^{6.8 \pm 0.3} M_{\odot}$. Separating the sample into active (LINERs+Seyferts) and inactive (ALG+H II) galaxies, an OLS regression analysis yields a relation $L_{R,\text{core}} \propto M_{*,\text{bulge}}^{1.42 \pm 0.18}$ for active galaxies with a slope that is double that for the inactive galaxies $L_{R,\text{core}} \propto M_{*,\text{bulge}}^{0.68 \pm 0.08}$. This trend of steepening slope for the AGN galaxies is echoed in the $L_{R,\text{core}} - L_{V,\text{bulge}}$ and $L_{R,\text{core}} - \sigma$ relations. Whether a single log-linear $L_{R,\text{core}} - M_{\text{BH}}$ relation holds over the entire radio core luminosity range is unclear.

(7) The hosts of active galaxies in general sit above the blue sequence defined by inactive, star-forming galaxies. Similarly, the ‘jetted’ radio AGN hosts are predominantly (85 per cent) blue sequence galaxies; co-spatial with the massive green valley hosts or lie on the red end of the blue sequence. These results reinforce the notion that AGN feedback shuts off or suppresses star formation in galaxies.

(8) Core-Sérsic galaxies, which represent ~ 12 per cent (20/173) of our sample, have high radio luminosities ($L_{R,\text{core}} \gtrsim 10^{35} \text{ erg s}^{-1}$) and are, in general, bulge-dominated early-type galaxies hosting either a LINER- or an ALG-type nuclear emission. We conclude that core-Sérsic galaxies with LINER nuclei likely involve AGN fuelling in hot gas accretion mode and some low level, residual star formation, whereas the growth of core-Sérsic ALGs may largely involve simple addition of stars and little gas. On the other hand, Sérsic galaxies, which have $L_{R,\text{core}} \sim 10^{32} - 10^{40} \text{ erg s}^{-1}$, are associated with all optical emission classes.

(9) All Seyferts are Sérsic galaxies, typically having intermediate mass bulges ($10^{10} - 10^{11} M_{\odot}$). Our observations suggest that Seyfert bulge formation and SMBH growth are likely to involve higher level of nuclear activity than their LINER analogues due to increased gas availability. LINERs are among the most massive galaxies in the sample having the highest incidence of radio detection and brightest radio core luminosities. ALGs have lower radio emissions than Seyferts and LINERs over the same $M_{*,\text{bulge}}$, $M_{V,\text{bulge}}$, and σ ranges. Our observations suggest gas-poor formation origin for ALGs. The vast majority (80 per cent) of the H II galaxies have low mass bulges ($M_{*,\text{bulge}} \lesssim 10^{10} M_{\odot}$) and a plausible scenario is that such bulges grow in a secular fashion where non-axisymmetric stellar structures fuel star formation at the centre, slowly feeding their SMBHs. All 10 bulge-less galaxies in the sample harbour H II nuclei.

ACKNOWLEDGEMENTS

We thank the referee for valuable comments which improved the presentation of this paper. BTD acknowledges support from grant ‘Ayudas para la realización de proyectos de I+D para jóvenes doctores 2019.’ for the HiMAGC (High-resolution, Multi-band Analysis of Galaxy Centres) project funded by Comunidad de Madrid and Universidad Complutense de Madrid under grant number PR65/19-22417. BTD and AGdP acknowledge financial support from the

Spanish Ministry of Science, Innovation and Universities (MCIUN) under grant No. RTI2018-096188-B-I00. JHK acknowledges financial support from the State Research Agency (AEI-MCINN) of the Spanish Ministry of Science and Innovation under the grant ‘The structure and evolution of galaxies and their central regions’ with reference PID2019-105602GB-I00/10.13039/501100011033, from the ACIISI, Consejería de Economía, Conocimiento y Empleo del Gobierno de Canarias and the European Regional Development Fund (ERDF) under grant with reference PROID2021010044, and from IAC project P/300724, financed by the Ministry of Science and Innovation, through the State Budget and by the Canary Islands Department of Economy, Knowledge and Employment, through the Regional Budget of the Autonomous Community. AA thanks the Spanish Ministerio de Ciencia e Innovación (grant PID2020-117404GB-C21) and the State Agency for Research of the Spanish MCIN through the ‘Center of Excellence Severo Ochoa’ award for the Instituto de Astrofísica de Andalucía (SEV-2017-0709). We would like to acknowledge the support the *e*-MERLIN Legacy project ‘LeMMINGs’, upon which this study is based. *e*-MERLIN and formerly, MERLIN, is a National Facility operated by the University of Manchester at Jodrell Bank Observatory on behalf of the STFC. We acknowledge Jodrell Bank Centre for Astrophysics, which is funded by the STFC. This research has made use of the NASA/IPAC Extragalactic Database (NED), which is operated by the Jet Propulsion Laboratory, California Institute of Technology, under contract with the National Aeronautics and Space Administration.

This work has made use of NUMPY (van der Walt, Colbert & Varoquaux 2011), MATPLOTLIB (Hunter 2007), and CORNER (Foreman-Mackey 2016) and ASTROPY, a community-developed core PYTHON package for Astronomy (Astropy Collaboration 2013, 2018), CUBEHELIX (Green 2011), JUPYTER (Kluyver et al. 2016), SCIPY (Virtanen et al. 2020), and of TOPCAT (i.e. ‘Tool for Operations on Catalogues And Tables’, Taylor 2005).

DATA AVAILABILITY

The data underlying this article are available in the article.

REFERENCES

- Aalto S. et al., 2015, *A&A*, 584, A42
 Amiri A., Tavasoli S., De Zotti G., 2019, *ApJ*, 874, 140
 Anglés-Alcázar D., Faucher-Giguère C.-A., Quataert E., Hopkins P. F., Feldmann R., Torrey P., Wetzel A., Kereš D., 2017, *MNRAS*, 472, L109
 Anglés-Alcázar D. et al., 2021, *ApJ*, 917, 53
 Astropy Collaboration, 2013, *A&A*, 558, A33
 Astropy Collaboration, 2018, *AJ*, 156, 123
 Athanassoula E., 1992, *MNRAS*, 259, 345
 Baldi R. D. et al., 2010, *ApJ*, 725, 2426
 Baldi R. D. et al., 2018, *MNRAS*, 476, 3478
 Baldi R. D. et al., 2021a, *MNRAS*, 500, 4749
 Baldi R. D. et al., 2021b, *MNRAS*, 508, 2019
 Baldry I. K., Glazebrook K., Brinkmann J., Ivezić Ž., Lupton R. H., Nichol R. C., Szalay A. S., 2004, *ApJ*, 600, 681
 Baldry I. K., Balogh M. L., Bower R. G., Glazebrook K., Nichol R. C., Bamford S. P., Budavari T., 2006, *MNRAS*, 373, 469
 Balmaverde B., Capetti A., 2006, *A&A*, 447, 97
 Barišić I. et al., 2017, *ApJ*, 847, 72
 Barnes J. E., Hernquist L. E., 1991, *ApJ*, 370, L65
 Barnes J. E., Hernquist L., 1996, *ApJ*, 471, 115
 Begelman M. C., Blandford R. D., Rees M. J., 1980, *Nature*, 287, 307
 Belfiore F. et al., 2018, *MNRAS*, 477, 3014
 Best P. N., Kauffmann G., Heckman T. M., Brinchmann J., Charlot S., Ivezić Ž., White S. D. M., 2005, *MNRAS*, 362, 25
 Best P. N., Kaiser C. R., Heckman T. M., Kauffmann G., 2006, *MNRAS*, 368, L67
 Best P. N., von der Linden A., Kauffmann G., Heckman T. M., Kaiser C. R., 2007, *MNRAS*, 379, 894
 Beswick R., Argo M. K., Evans R., McHardy I., Williams D. R. A., Westcott J., 2014, in Proceedings of the 12th European VLBI Network Symposium and Users Meeting (EVN 2014), 7–10 October 2014. Cagliari, p. 10
 Bluck A. F. L., Mendel J. T., Ellison S. L., Moreno J., Simard L., Patton D. R., Starkeburg E., 2014, *MNRAS*, 441, 599
 Blumenthal G. R., Faber S. M., Primack J. R., Rees M. J., 1984, *Nature*, 311, 517
 Bonanos A. Z. et al., 2006, *ApJ*, 652, 313
 Bouquin A. Y. K. et al., 2018, *ApJS*, 234, 18
 Bower R. G., Lucey J. R., Ellis R. S., 1992, *MNRAS*, 254, 601
 Bower R. G., Schaye J., Frenk C. S., Theuns T., Schaller M., Crain R. A., McAlpine S., 2017, *MNRAS*, 465, 32
 Buttigione S., Capetti A., Celotti A., Axon D. J., Chiaberge M., Macchetto F. D., Sparks W. B., 2010, *A&A*, 509, A6
 Capetti A., Balmaverde B., 2005, *A&A*, 440, 73
 Capetti A., Balmaverde B., 2007, *A&A*, 469, 75
 Cappellari M. et al., 2011, *MNRAS*, 416, 1680
 Carter B. J., Fabricant D. G., Geller M. J., Kurtz M. J., McLean B., 2001, *ApJ*, 559, 606
 Cattaneo A., Dekel A., Devriendt J., Guiderdoni B., Blaizot J., 2006, *MNRAS*, 370, 1651
 Cattaneo A. et al., 2009, *Nature*, 460, 213
 Chauke P. et al., 2019, *ApJ*, 877, 48
 Chen Z. et al., 2020, *ApJ*, 897, 102
 Cisternas M. et al., 2011, *ApJ*, 726, 57
 Crook A. C., Huchra J. P., Martimbeau N., Masters K. L., Jarrett T., Macri L. M., 2007, *ApJ*, 655, 790
 Croton D. J. et al., 2006, *MNRAS*, 365, 11
 Davies R. I., Müller Sánchez F., Genzel R., Tacconi L. J., Hicks E. K. S., Friedrich S., Sternberg A., 2007, *ApJ*, 671, 1388
 Davis T. A., Greene J. E., Ma C.-P., Blakeslee J. P., Dawson J. M., Pandya V., Veale M., Zabel N., 2019, *MNRAS*, 486, 1404
 de La Rosa I. G., La Barbera F., Ferreras I., de Carvalho R. R., 2011, *MNRAS*, 418, L74
 de Ruiter H. R., Parma P., Capetti A., Fanti R., Morganti R., Santantonio L., 2005, *A&A*, 439, 487
 de Vaucouleurs G., 1959, *Handb. Phys.*, 53, 275
 de Vaucouleurs G., de Vaucouleurs A., Corwin H. G., Jr, Buta R. J., Paturel G., Fouqué P., 1991, Third Reference Catalogue of Bright Galaxies. Volume I: Explanations and references. Volume II: Data for galaxies between 0^h and 12^h. Volume III: Data for galaxies between 12^h and 24^h. Springer, Berlin
 Disney M. J., Sparks W. B., Wall J. V., 1984, *MNRAS*, 206, 899
 Dopita M. A., Sutherland R. S., 1995, *ApJ*, 455, 468
 Dosopoulou F., Greene J. E., Ma C.-P., 2021, *ApJ*, 922, 40
 Dressler A., 1980, *ApJ*, 236, 351
 Dressler A., 1984, *ARA&A*, 22, 185
 Dullo B. T., 2019, *ApJ*, 886, 80
 Dullo B. T., Graham A. W., 2012, *ApJ*, 755, 163
 Dullo B. T., Graham A. W., 2013, *ApJ*, 768, 36
 Dullo B. T., Graham A. W., 2014, *MNRAS*, 444, 2700
 Dullo B. T., Graham A. W., 2015, *ApJ*, 798, 55
 Dullo B. T., Graham A. W., Knapen J. H., 2017, *MNRAS*, 471, 2321
 Dullo B. T. et al., 2018, *MNRAS*, 475, 4670
 Dullo B. T. et al., 2019, *ApJ*, 871, 9
 Dullo B. T., Bouquin A. Y. K., Gil de Paz A., Knapen J. H., Gorgas J., 2020, *ApJ*, 898, 83
 Dullo B. T., Gil de Paz A., Knapen J. H., 2021, *ApJ*, 908, 134
 Dullo B. T. et al., 2023, preprint (arXiv:2303.11154)
 Dunlop J. S., McLure R. J., Kukula M. J., Baum S. A., O’Dea C. P., Hughes D. H., 2003, *MNRAS*, 340, 1095
 Ebisuzaki T., Makino J., Okumura S. K., 1991, *Nature*, 354, 212
 Emsellem E. et al., 2011, *MNRAS*, 414, 888
 Englmaier P., Shlosman I., 2000, *ApJ*, 528, 677

- Faber S. M. et al., 1997, *AJ*, 114, 1771
 Faber S. M. et al., 2007, *ApJ*, 665, 265
 Fabian A. C., 2012, *ARA&A*, 50, 455
 Fall S. M., Efstathiou G., 1980, *MNRAS*, 193, 189
 Feigelson E. D., Babu G. J., 1992, *ApJ*, 397, 55
 Feigelson E. D., Nelson P. I., 1985, *ApJ*, 293, 192
 Ferland G. J., Netzer H., 1983, *ApJ*, 264, 105
 Ferrarese L., Ford H., 2005, *Space Sci. Rev.*, 116, 523
 Ferrarese L., Merritt D., 2000, *ApJ*, 539, L9
 Ferrarese L. et al., 2006, *ApJS*, 164, 334
 Filho M. E., Fraternali F., Markoff S., Nagar N. M., Barthel P. D., Ho L. C., Yuan F., 2004, *A&A*, 418, 429
 Filho M. E., Barthel P. D., Ho L. C., 2006, *A&A*, 451, 71
 Filippenko A. V., Sargent W. L. W., 1985, *ApJS*, 57, 503
 Fiore F. et al., 2017, *A&A*, 601, A143
 Foreman-Mackey D., 2016, *J. Open Source Softw.*, 1, 24
 Förster Schreiber N. M. et al., 2014, *ApJ*, 787, 38
 Freedman W. L. et al., 2019, *ApJ*, 882, 34
 Galloway M. A. et al., 2015, *MNRAS*, 448, 3442
 Gao F. et al., 2020, *A&A*, 637, A94
 García-Burillo S., Combes F., Schinnerer E., Boone F., Hunt L. K., 2005, *A&A*, 441, 1011
 Gebhardt K. et al., 2000, *ApJ*, 539, L13
 Gendre M. A., Best P. N., Wall J. V., Ker L. M., 2013, *MNRAS*, 430, 3086
 Gómez P. L. et al., 2003, *ApJ*, 584, 210
 Goulding A. D., Alexander D. M., 2009, *MNRAS*, 398, 1165
 Graham A. W., Worley C. C., 2008, *MNRAS*, 388, 1708
 Graham A. W., Erwin P., Trujillo I., Asensio Ramos A., 2003, *AJ*, 125, 2951
 Green D. A., 2011, *Bull. Astron. Soc. India*, 39, 289
 Greene J. E., Ho L. C., Barth A. J., 2008, *ApJ*, 688, 159
 Greene J. E. et al., 2010, *ApJ*, 721, 26
 Gunn J. E., Gott J. Richard I., 1972, *ApJ*, 176, 1
 Häring N., Rix H.-W., 2004, *ApJ*, 604, L89
 Heckman T. M., 1980, *A&A*, 500, 187
 Heckman T. M., Best P. N., 2014, *ARA&A*, 52, 589
 Heisler J., Tremaine S., Bahcall J. N., 1985, *ApJ*, 298, 8
 Hernquist L., 1989, *Nature*, 340, 687
 Ho L. C., 2002, *ApJ*, 564, 120
 Ho L. C., 2008, *ARA&A*, 46, 475
 Ho L. C., Filippenko A. V., Sargent W. L., 1995, *ApJS*, 98, 477
 Ho L. C., Filippenko A. V., Sargent W. L. W., 1997a, *ApJS*, 112, 315
 Ho L. C., Filippenko A. V., Sargent W. L. W., Peng C. Y., 1997b, *ApJS*, 112, 391
 Ho L. C., Filippenko A. V., Sargent W. L. W., 1997c, *ApJ*, 487, 568
 Ho L. C., Greene J. E., Filippenko A. V., Sargent W. L. W., 2009, *ApJS*, 183, 1
 Hopkins P. F., Hernquist L., 2006, *ApJS*, 166, 1
 Hopkins P. F., Hernquist L., 2009, *ApJ*, 694, 599
 Hopkins P. F., Quataert E., 2011, *MNRAS*, 415, 1027
 Hopkins P. F., Hernquist L., Cox T. J., Di Matteo T., Robertson B., Springel V., 2006, *ApJS*, 163, 1
 Hopkins P. F., Cox T. J., Dutta S. N., Hernquist L., Kormendy J., Lauer T. R., 2009a, *ApJS*, 181, 135
 Hopkins P. F., Lauer T. R., Cox T. J., Hernquist L., Kormendy J., 2009b, *ApJS*, 181, 486
 Hubble E. P., 1926, *ApJ*, 64, 321
 Hummel E., Kotanyi C. G., Ekers R. D., 1983, *A&A*, 125, 205
 Hunter J. D., 2007, *Comput. Sci. Eng.*, 9, 90
 Ibañez R. A. et al., 2013, *Nature*, 493, 62
 Isobe T., Feigelson E. D., Nelson P. I., 1986, *ApJ*, 306, 490
 Jiang Y.-F., Greene J. E., Ho L. C., 2011, *ApJ*, 737, L45
 Karachentsev I. D., Karachentseva V. E., Huchtmeier W. K., Makarov D. I., 2004, *AJ*, 127, 2031
 Kauffmann G., Haehnelt M., 2000, *MNRAS*, 311, 576
 Kauffmann G. et al., 2003a, *MNRAS*, 341, 54
 Kauffmann G. et al., 2003b, *MNRAS*, 346, 1055
 Kauffmann G., White S. D. M., Heckman T. M., Ménard B., Brinchmann J., Charlot S., Tremonti C., Brinkmann J., 2004, *MNRAS*, 353, 713
 Kauffmann G., Heckman T. M., Best P. N., 2008, *MNRAS*, 384, 953
 Kaviraj S., 2010, *MNRAS*, 406, 382
 Kaviraj S., Schawinski K., Silk J., Shabala S. S., 2011, *MNRAS*, 415, 3798
 Kaviraj S., Martin G., Silk J., 2019, *MNRAS*, 489, L12
 Kewley L. J., Groves B., Kauffmann G., Heckman T., 2006, *MNRAS*, 372, 961
 King A., Pounds K., 2015, *ARA&A*, 53, 115
 Kluyver T. et al., 2016, in *IOS Press*, p. 87
 Knapen J. H., 2004, in Block D. L., Puerari I., Freeman K. C., Groess R., Block E. K., eds, *Penetrating Bars Through Masks of Cosmic Dust*, Vol. 319 (Astrophysics and Space Science Library). Springer, Berlin, p. 189
 Knapen J. H., Beckman J. E., Heller C. H., Shlosman I., de Jong R. S., 1995, *ApJ*, 454, 623
 Kocevski D. D. et al., 2012, *ApJ*, 744, 148
 Kormendy J., 1982, *ApJ*, 257, 75
 Kormendy J., 1993, in Dejonghe H., Habing H. J. eds, *Galactic Bulges*, Vol. 153. Springer, Berlin, p. 209
 Kormendy J., Bender R., 2012, *ApJS*, 198, 2
 Kormendy J., Ho L. C., 2013, *ARA&A*, 51, 511
 Kormendy J., Kennicutt Robert C. J., 2004, *ARA&A*, 42, 603
 Kormendy J., Richstone D., 1995, *ARA&A*, 33, 581
 Kormendy J., Fisher D. B., Cornell M. E., Bender R., 2009, *ApJS*, 182, 216
 Krajnović D. et al., 2013, *MNRAS*, 433, 2812
 Krajnović D. et al., 2020, *A&A*, 635, A129
 Lagos C. D. P., Cora S. A., Padilla N. D., 2008, *MNRAS*, 388, 587
 Laine S., van der Marel R. P., Lauer T. R., Postman M., O’Dea C. P., Owen F. N., 2003, *AJ*, 125, 478
 Larson R. B., Tinsley B. M., Caldwell C. N., 1980, *ApJ*, 237, 692
 Laurikainen E., Salo H., 1995, *A&A*, 293, 683
 Laurikainen E., Salo H., Buta R., 2005, *MNRAS*, 362, 1319
 Lin L. et al., 2020, *MNRAS*, 499, 1406
 Madau P., Dickinson M., 2014, *ARA&A*, 52, 415
 Magliocchetti M. et al., 2020, *MNRAS*, 493, 3838
 Magorrian J. et al., 1998, *AJ*, 115, 2285
 Makarov D., Prugniel P., Terekhova N., Courtois H., Vauglin I., 2014, *A&A*, 570, A13
 Man Z.-y., Peng Y.-j., Kong X., Guo K.-x., Zhang C.-p., Dou J., 2019, *MNRAS*, 488, 89
 Mandelbaum R., Li C., Kauffmann G., White S. D. M., 2009, *MNRAS*, 393, 377
 Marconi A., Hunt L. K., 2003, *ApJ*, 589, L21
 Marsden C., Shankar F., Bernardi M., Sheth R. K., Fu H., Lapi A., 2022, *MNRAS*, 510, 5639
 Martín-Navarro I., Mezcuá M., 2018, *ApJ*, 855, L20
 McConnell N. J., Ma C.-P., 2013, *ApJ*, 764, 184
 McDermid R. M. et al., 2015, *MNRAS*, 448, 3484
 McLure R. J., Dunlop J. S., 2002, *MNRAS*, 331, 795
 McNamara B. R., Nulsen P. E. J., 2007, *ARA&A*, 45, 117
 McNamara B. R., Kazemzadeh F., Rafferty D. A., Birzan L., Nulsen P. E. J., Kirkpatrick C. C., Wise M. W., 2009, *ApJ*, 698, 594
 McNamara B. R., Rohanizadegan M., Nulsen P. E. J., 2011, *ApJ*, 727, 39
 Meidt S. E. et al., 2014, *ApJ*, 788, 144
 Méndez-Abreu J. et al., 2017, *A&A*, 598, A32
 Merloni A., Heinz S., 2008, *MNRAS*, 388, 1011
 Merritt D., 2006, *ApJ*, 648, 976
 Mezcuá M., Suh H., Civano F., 2019, *MNRAS*, 488, 685
 Miller C. J., Nichol R. C., Gómez P. L., Hopkins A. M., Bernardi M., 2003, *ApJ*, 597, 142
 Milosavljević M., Merritt D., 2001, *ApJ*, 563, 34
 Miraghaei H., Best P. N., 2017, *MNRAS*, 466, 4346
 Mishra H. D., Dai X., 2020, *AJ*, 159, 69
 Mishra H. D., Dai X., Guerras E., 2021, *ApJ*, 922, L17
 Moore B., Katz N., Lake G., Dressler A., Oemler A., 1996, *Nature*, 379, 613
 Morganti R., 2017, *Nat. Astron.*, 1, 596
 Muldrew S. I. et al., 2012, *MNRAS*, 419, 2670
 Naab T., Khochfar S., Burkert A., 2006, *ApJ*, 636, L81
 Nagar N. M., Falcke H., Wilson A. S., Ulvestad J. S., 2002, *A&A*, 392, 53

- Nagar N. M., Falcke H., Wilson A. S., 2005, *A&A*, 435, 521
- Nasim I., Gualandris A., Read J., Dehnen W., Delorme M., Antonini F., 2020, *MNRAS*, 497, 739
- Nasim I. T., Gualandris A., Read J. I., Antonini F., Dehnen W., Delorme M., 2021, *MNRAS*, 502, 4794
- Nguyen D. D. et al., 2019, *ApJ*, 872, 104
- Nyland K. et al., 2016, *MNRAS*, 458, 2221
- O'Dea C. P. et al., 2008, *ApJ*, 681, 1035
- Panessa F., Baldi R. D., Laor A., Padovani P., Behar E., McHardy I., 2019, *Nat. Astron.*, 3, 387
- Peng Y.-j. et al., 2010, *ApJ*, 721, 193
- Peng Y., Maiolino R., Cochrane R., 2015, *Nature*, 521, 192
- Penny S. J. et al., 2018, *MNRAS*, 476, 979
- Pimblett K. A., Shabala S. S., Haines C. P., Fraser-McKelvie A., Floyd D. J. E., 2013, *MNRAS*, 429, 1827
- Planck Collaboration VI, 2020, *A&A*, 641, A6
- Putman M. E., Zheng Y., Price-Whelan A. M., Grcevich J., Johnson A. C., Tollerud E., Peek J. E. G., 2021, *ApJ*, 913, 53
- Rantala A., Johansson P. H., Naab T., Thomas J., Frigo M., 2018, *ApJ*, 864, 113
- Richings A. J., Uttley P., K rding E., 2011, *MNRAS*, 415, 2158
- Richstone D. et al., 1998, *Nature*, 395, A14
- Ricotti M., Gnedin N. Y., 2005, *ApJ*, 629, 259
- Riess A. G., Casertano S., Yuan W., Macri L. M., Scolnic D., 2019, *ApJ*, 876, 85
- Rusli S. P., Erwin P., Saglia R. P., Thomas J., Fabricius M., Bender R., Nowak N., 2013, *AJ*, 146, 160
- Russell H. R. et al., 2014, *ApJ*, 784, 78
- Russell H. R. et al., 2019, *MNRAS*, 490, 3025
- Sabater J., Best P. N., Argudo-Fern andez M., 2013, *MNRAS*, 430, 638
- Sabater J. et al., 2019, *A&A*, 622, A17
- Sadler E. M., Slee O. B., Reynolds J. E., Roy A. L., 1995, *MNRAS*, 276, 1373
- Saikia P., K rding E., Falcke H., 2015, *MNRAS*, 450, 2317
- Saikia P., K rding E., Coppejans D. L., Falcke H., Williams D., Baldi R. D., McHardy I., Beswick R., 2018, *A&A*, 616, A152
- Salo H. et al., 2015, *ApJS*, 219, 4
- Salom  P., Combes F., 2003, *A&A*, 412, 657
- Sandage A., 1965, *ApJ*, 141, 1560
- Sanders D. B., Soifer B. T., Elias J. H., Neugebauer G., Matthews K., 1988, *ApJ*, 328, L35
- Sarzi M. et al., 2010, *MNRAS*, 402, 2187
- Schawinski K. et al., 2010, *ApJ*, 711, 284
- Schawinski K., Treister E., Urry C. M., Cardamone C. N., Simmons B., Yi S. K., 2011, *ApJ*, 727, L31
- Schawinski K. et al., 2014, *MNRAS*, 440, 889
- Schawinski K., Koss M., Berney S., Sartori L. F., 2015, *MNRAS*, 451, 2517
- Seyfert C. K., 1943, *ApJ*, 97, 28
- Shabala S. S., Ash S., Alexander P., Riley J. M., 2008, *MNRAS*, 388, 625
- Shankar F., Marulli F., Mathur S., Bernardi M., Bournaud F., 2012, *A&A*, 540, A23
- Shlosman I., 1994, *Mass-Transfer Induced Activity in Galaxies*. Cambridge Univ. Press, Cambridge
- Shlosman I., Frank J., Begelman M. C., 1989, *Nature*, 338, 45
- Sijacki D., Springel V., Di Matteo T., Hernquist L., 2007, *MNRAS*, 380, 877
- Silk J., 2005, *MNRAS*, 364, 1337
- Silk J., Rees M. J., 1998, *A&A*, 331, L1
- Simmons B. D. et al., 2013, *MNRAS*, 429, 2199
- Singh R. et al., 2013, *A&A*, 558, A43
- Skrutskie M. F. et al., 2006, *AJ*, 131, 1163
- Smith R. J., Edge A. C., 2017, *MNRAS*, 471, L66
- Somerville R. S., Hopkins P. F., Cox T. J., Robertson B. E., Hernquist L., 2008, *MNRAS*, 391, 481
- Tabor G., Binney J., 1993, *MNRAS*, 263, 323
- Taylor M. B., 2005, in Shopbell P., Britton M., Ebert R. eds, *ASP Conf. Ser. Vol. 347, Astronomical Data Analysis Software and Systems XIV*. Astron. Soc. Pac., San Francisco, p. 29
- Thomas D., Greggio L., Bender R., 1999, *MNRAS*, 302, 537
- Thomas D., Maraston C., Bender R., Mendes de Oliveira C., 2005, *ApJ*, 621, 673
- Thomas D., Maraston C., Schawinski K., Sarzi M., Silk J., 2010, *MNRAS*, 404, 1775
- Tolstoy E., Hill V., Tosi M., 2009, *ARA&A*, 47, 371
- Toomre A., Toomre J., 1972, *ApJ*, 178, 623
- Tremaine S. et al., 2002, *ApJ*, 574, 740
- Trujillo I., Erwin P., Asensio Ramos A., Graham A. W., 2004, *AJ*, 127, 1917
- Ulvestad J. S., Ho L. C., 2001a, *ApJ*, 558, 561
- Ulvestad J. S., Ho L. C., 2001b, *ApJ*, 562, L133
- Urrutia T., Lacy M., Becker R. H., 2008, *ApJ*, 674, 80
- van den Bosch R. C. E., 2016, *ApJ*, 831, 134
- van der Walt S., Colbert S. C., Varoquaux G., 2011, *Comput. Sci. Eng.*, 13, 22
- Veale M. et al., 2017a, *MNRAS*, 464, 356
- Veale M., Ma C.-P., Greene J. E., Thomas J., Blakeslee J. P., McConnell N., Walsh J. L., Ito J., 2017b, *MNRAS*, 471, 1428
- Venturi G. et al., 2021, *A&A*, 648, A17
- Virtanen P. et al., 2020, *Nat. Methods*, 17, 261
- von der Linden A., Wild V., Kauffmann G., White S. D. M., Weinmann S., 2010, *MNRAS*, 404, 1231
- Vulcani B., Poggianti B. M., Fritz J., Fasano G., Moretti A., Calvi R., Paccagnella A., 2015, *ApJ*, 798, 52
- Wake D. A. et al., 2006, *MNRAS*, 372, 537
- Weinberger R. et al., 2017, *MNRAS*, 465, 3291
- Westoby P. B., Mundell C. G., Baldry I. K., 2007, *MNRAS*, 382, 1541
- White S. D. M., Frenk C. S., 1991, *ApJ*, 379, 52
- White S. D. M., Rees M. J., 1978, *MNRAS*, 183, 341
- Williams D. R. A. et al., 2022, *MNRAS*, 510, 4909
- Willmer C. N. A., 2018, *ApJS*, 236, 47
- Wrobel J. M., Heeschen D. S., 1991, *AJ*, 101, 148
- Young L. M. et al., 2011, *MNRAS*, 414, 940

MEASURES OF GALAXY ENVIRONMENTS

We employ four local density estimators based on the nearest neighbour method as measures of the galaxy environment (ρ_{10} , ρ_3 , ν_{10} , and ν_3 , see e.g. Cappellari et al. 2011; Muldrew et al. 2012; Veale et al. 2017b). We choose the number of nearest neighbours to be $N_{\text{gal}} = 3$ and 10 which generally are suitable to probe different scales of the galaxy local environment at the distances of our sample (Muldrew et al. 2012).

The mathematical expression for the local surface density of a galaxy ρ_{10} is

$$\rho_{10} = \frac{N_{\text{gal}}}{\pi R_{10}^2}, \quad (\text{A1})$$

where R_{10} is the radius, which is centred on the target galaxy and

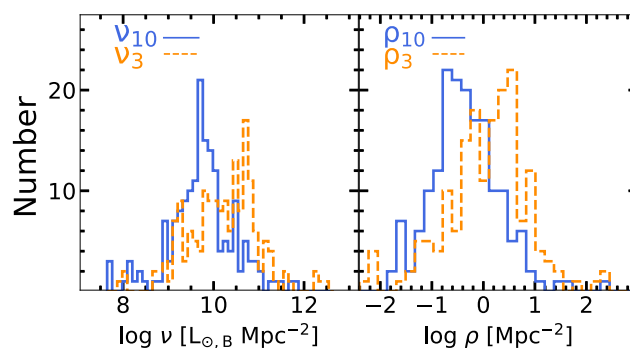


Figure A1. Histogram of the luminosity surface densities (ν_{10} and ν_3) and surface densities (ρ_{10} and ρ_3) for our sample of 173 LeMMINGS galaxies.

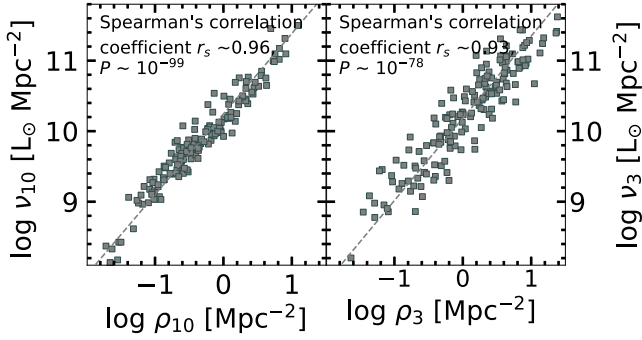


Figure A2. Correlations between luminosity surface density (ν) and surface density (ρ) for our sample.

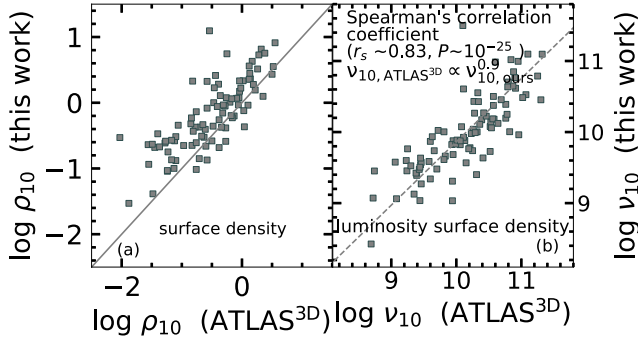


Figure A3. (a) Comparison of our local surface density values with those from the ATLAS^{3D} (Cappellari et al. 2011) for 91 overlapping galaxies. The solid line shows a one-to-one relation. (b) Our B -band luminosity surface density values are plotted as a function of the ATLAS^{3D} K -band luminosity surface density values. The dashed line is the least-squares fit to the luminosity surface density data ($\nu_{10, \text{ATLAS}^{3D}} \propto \nu_{10, \text{ours}}^{0.9}$).

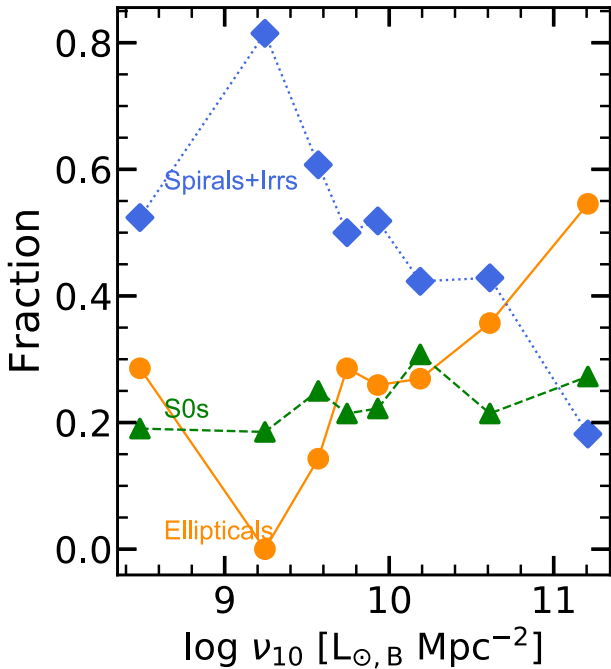


Figure A4. Morphology–density relation. The fraction of elliptical (circles), S0 (triangles), and spiral+Irr galaxies (diamonds) plotted against our B -band luminosity surface density ν_{10} for 205 (=173+32) nearby galaxies (Dullo & Graham 2014; Dullo 2019, plus this work).

defines a cylinder that encloses the nearest $N_{\text{gal}} (=10)$ neighbours. We use a B -band magnitude cut of $M_B \lesssim -18.0$ mag for the neighbours, which are selected to be within a velocity cylinder of ± 300 km s^{-1} around the target galaxy (i.e. a relative heliocentric velocity $|V_{\text{hel, target}} - V_{\text{hel, neighbour}}| < 300$ km s^{-1} , see Cappellari et al. 2011, their Section 3.1). We note that N_{gal} does not include the target galaxy.

The surface density ρ_3 is similar to ρ_{10} but the former is defined by a cylinder containing three nearest neighbours with $M_B \lesssim -18.0$ mag and a velocity cut of $\Delta V_{\text{hel}} < 300$ km s^{-1} and it can be written as

$$\rho_3 = \frac{N_{\text{gal}}}{\pi R_3^2}, \quad (\text{A2})$$

where R_3 is the radius centred on the target galaxy enclosing the third nearest neighbour.

The quantity ν_{10} is the luminosity surface density of a galaxy inside a cylinder containing its 10 nearest neighbours and it can be written as

$$\nu_{10} = \frac{\sum_{i=1}^{10} 10^{-0.4(M_{i,B} - M_{\odot,B})}}{\pi R_{10}^2}, \quad (\text{A3})$$

where the B -band solar luminosity is $M_{\odot,B} = 5.44$ mag (Willmer 2018). The index i runs from 1 to 10, indicating the 10 nearest neighbours of the target galaxy and R_{10} is defined in the same manner as in ρ_{10} (equation A1). Similarly, the luminosity surface density ν_3 is defined as

$$\nu_3 = \frac{\sum_{i=1}^3 10^{-0.4(M_{i,B} - M_{\odot,B})}}{\pi R_3^2}, \quad (\text{A4})$$

where R_3 is defined as in ρ_3 (equation A2).

The B -band absolute magnitudes of the galaxies are from Hyperleda (Makarov et al. 2014). We use NED for an automated search of the nearest neighbours around a target galaxy and for obtaining their radial velocities. NED represents the most current and comprehensive assimilation of extragalactic objects and their radial velocities. That is, it offers the most complete available data to define the environment of a galaxy using its radial velocity and the radial velocities of other galaxies typically observed along and around that same line of sight. The maximum search radius for a nearest neighbour allowed by NED is 10 Mpc. The luminosity surface densities ν_{10} and ν_3 are listed in see Table A1.

Fig. A1 plots the distribution of the values of ρ_{10} , ρ_3 , ν_{10} , and ν_3 (see Table A1) for our sample of 173 galaxies. We note that for the sample galaxies at distances $D \lesssim 5$ Mpc (23/173) our values of ρ_{10} , ρ_3 , ν_{10} , and ν_3 are upper limits. These local galaxy density estimates span roughly five orders of magnitude, suitable to test the influence of the local environment of galaxies on their evolution.

Fig. A2 explores which local density method results in a better measurement of the galaxy environment by comparing our values of the surface density ρ and luminosity surface density ν for a given number of neighbours. We find strong correlations between the two local density estimators ρ and ν (Spearman's correlation coefficient $r_s \sim 0.93 - 0.96$, $P \sim 10^{-99} - 10^{-78}$), revealing that they provide a comparable measure of the galaxy environment.

We next compare our ρ_{10} , ρ_3 , ν_{10} , and ν_3 values with those from Cappellari et al. (2011, their tables 2 and 3) who tabulated local galaxy density estimates for the ATLAS^{3D} parent sample of 871 nearby galaxies in the ATLAS^{3D} volume with $M_K \leq -21.5$ mag drawn from the Two Micron All Sky Survey (2MASS; Skrutskie et al. 2006). Comparing the data, we find that their K -band magnitude cut of $M_K \leq -21.5$ mag approximately corresponds to our B -band magnitude cut of $M_B \lesssim -18.0$ mag. There are 91 galaxies

Table A1. LeMMINGs data.

Galaxy	Type	D (Mpc)	Class	σ (km s ⁻¹)	$M_{V, \text{bulge}}$ (mag)	$M_{V, \text{galxy}}$ (mag)	$\log M_{*}^{\text{bulge}}$ (M _⊙)	$\log M_{*}^{\text{galxy}}$ (M _⊙)	$\log M_{\text{BH}}$ (M _⊙)	$\log L_{\text{K, core}}$ (erg s ⁻¹)	ϵ	Med (B_4)	γ	Det	AGN Sequence	\log^{10} (L _⊙ Mpc ⁻²)	\log^{13} (L _⊙ Mpc ⁻²)	$\log M_{\text{halo}}$ (M _⊙)	
(1)	(2)	(3)	(4)	(5)	(6)	(7)	(8)	(9)	(10)	(11)	(12)	(13)	(14)	(15)	(16)	(17)	(18)	(19)	(20)
I0239	SAB(rs)c	9.9	H II	92.3	-16.82 ± 0.29	-18.80	9.04 ± 0.14	9.84	-	<35.0	0.18	0.003	0.03	U	-	9.5	11.2	13.1	
I0356	SA(s)abp	11.7	H II	156.6	-16.63 ± 0.41	-19.03	10.57 ± 0.29	11.53	-	35.5	0.18	0.006	0.40	I	A	9.6	11.0	14.6	
I0520	SAB(rs)a	50.9	L	138.1	-20.74 ± 0.52	-22.62	10.71 ± 0.21	11.47	-	<36.1	0.07	0.005	0.62	U	-	10.3	10.7	13.6	
I2574 [†]	SAB(s)m	2.1	H II	33.9	-	-19.87	-	9.46	-	<33.7	-	-	-	U	-	BS	<10.7	12.3	
N0147	E5 pec	0.8 ^k	ALG	22.0	-15.76 ± 0.17	-15.76	9.05 ± 0.12	9.05	-	<32.4	0.30	0.002	0.00	U	-	<7.7	<7.3	13.6	
N0205	E5 pec	0.8 ^k	ALG	23.3	-18.22 ± 0.27	-18.22	9.53 ± 0.13	9.53	3.83 ^{+1.18} _{-1.83}	<32.4	0.16	0.001	0.07	U	-	<7.7	<7.1	11.2	
N0221	compact E2	0.8 ^k	ALG	72.1	-15.52 ± 0.18	-16.48	8.61 ± 0.11	8.99	-	<32.3	0.24	0.006	0.24	U	-	<7.7	<7.2	11.2	
N0266	SB(rs)ab	62.9	L	229.6	-22.93 ± 0.20	-23.36	11.80 ± 0.12	11.97	-	36.9	0.08	0.003	0.39	I	A	11.8	12.3	13.6	
N0278	SAB(rs)b	5.3	H II	47.6	-16.04 ± 0.21	-17.65	8.82 ± 0.12	9.46	-	34.8	0.10	0.001	0.15	I	A	<9.4	<9.1	12.5	
N0315	cD	67.0	L/RL	303.7	-23.59 ± 0.27	-23.79	11.69 ± 0.14	11.77	8.99 ^{+0.32} _{-0.32}	39.6	0.29	-0.021	0.03	I	A	10.5	10.5	13.5	
N0404	SA0-(s)	3.1 ^k	L	40.0	-17.39 ± 0.23	-17.40	9.33 ± 0.13	9.33	5.65 ^{+0.25} _{-0.25}	<33.3	0.14	0.005	0.31	U	-	<8.1	<8.0	14.4	
N0410	cD	72.4	L	299.7	-20.72 ± 0.13	-21.51	11.76 ± 0.10	12.09	-	37.3	0.17	-0.020	-0.02	I	A	12.7	12.5	14.4	
N0507	SA00(r)	63.7	ALG	292.0	-22.56 ± 0.27	-23.48	11.70 ± 0.13	12.07	-	36.9	0.25	0.002	0.07	I	A	10.9	11.3	14.4	
N0598	SA(s)cd	1.0 ^b	H II	21.0	-11.84 ± 0.21	-18.59	6.89 ± 0.12	9.58	-	<32.4	0.20	0.001	1.21	U	-	<8.1	<7.9	13.0	
N0672 [†]	SB(s)cd	7.2 ^k	H II	64.3	-	-19.51	-	9.76	-	<34.6	-	-	-	U	-	9.6	9.1	13.7	
N0777	E1	68.8	L/RL	324.1	-20.68 ± 0.22	-20.68	11.75 ± 0.12	11.75	-	36.8	0.14	-0.073	0.07	I	A	10.2	10.8	13.5	
N0784 [†]	SBdm	5.0 ^k	H II	35.5	-	-16.73	-	8.65	-	<34.2	-	-	-	U	-	<8.2	<9.0	12.9	
N0841	(R')SAB(s)ab	62.2	L	159.2	-21.34 ± 0.22	-22.23	10.27 ± 0.12	10.62	-	<36.2	0.42	0.005	0.01	U	-	9.7	11.3	13.2	
N0890	SAB0-(r)?	54.0	ALG	210.9	-20.12 ± 0.19	-20.46	11.41 ± 0.12	11.55	-	<36.0	0.31	-0.013	0.50	U	-	9.2	10.4	14.4	
N0959	Sdm?	5.4	H II	43.6	-14.68 ± 0.14	-16.12	8.08 ± 0.09	8.65	-	<34.7	0.07	0.016	0.12	U	-	>10.0	<10.5	13.7	
N1003	SA(s)cd	6.1	H II	-	-11.25 ± 0.02	-18.12	6.97 ± 0.08	9.72	-	<34.6	0.77	-0.185	0.16	U	-	9.5	11.2	14.0	
N1023	SB0-(rs)	6.2	ALG	204.5	-19.35 ± 0.26	-19.94	10.86 ± 0.13	11.10	7.38 ^{+0.04} _{-0.04}	<34.6	0.26	0.007	0.52	U	-	9.4	11.1	13.8	
N1058	SA(rs)c	4.5	L	31.0	-13.36 ± 0.34	-16.34	7.36 ± 0.15	8.55	-	<34.4	0.16	0.006	0.01	U	-	<9.7	<10.9	14.0	
N1156 [†]	IB(s)m	2.5	H II	35.9	-	-16.81	-	8.51	-	<34.2	-	-	-	U	-	<9.4	<9.3	12.9	
N1161	S0	25.6	L/RL	258.4	-22.08 ± 0.07	-22.25	11.43 ± 0.10	11.49	-	36.6	0.35	0.006	0.13	I	A	8.0	9.3	13.6	
N1167	SA0-	68.0	L/RL	216.9	-19.72 ± 0.27	-20.39	11.57 ± 0.12	11.84	-	39.7	0.08	-0.001	0.23	I	A	10.0	10.8	13.1	
N1275	cDpec	73.9	L/RL	258.9	-23.50 ± 0.43	-23.77	11.47 ± 0.18	11.57	9.00 ^{+0.20} _{-0.20}	41.0	0.23	-0.006	0.24	I	A	9.5	11.2	13.1	
N1961	SAB(rs)c	56.4	L/RL	241.3	-22.96 ± 0.47	-23.49	11.28 ± 0.20	11.49	8.35 ^{+0.35} _{-0.35}	37.2	0.21	0.014	0.30	I	A	9.7	11.4	13.4	
N2273	SB(r)l?	26.9	S	148.9	-20.74 ± 0.35	-21.27	10.73 ± 0.16	10.94	6.89 ^{+0.04} _{-0.04}	36.6	0.37	0.005	0.32	I	E	9.0	10.3	13.9	
N2276	SAB(rs)c	34.3	H II	83.5	-19.13 ± 0.08	-21.43	9.30 ± 0.09	10.22	-	<35.9	0.39	-0.017	0.17	U	-	9.2	9.2	13.9	

Table A1 – continued

Galaxy	Type	D (Mpc)	Class	σ (km s ⁻¹)	$M_{V, \text{bulge}}$ (mag)	$M_{V, \text{glxy}}$ (mag)	$\log M_{*, \text{bulge}}$ (M _⊙)	$\log M_{*, \text{glxy}}$ (M _⊙)	$\log M_{\text{BH}}$ (M _⊙)	$\log L_{\text{R, core}}$ (erg s ⁻¹)	ϵ	Med (B_4)	γ	Det	AGN	Sequence	$\log \nu_{10}$ (L _⊙ Mpc ⁻²)	$\log \nu_3$ (L _⊙ Mpc ⁻²)	$\log M_{\text{halo}}$ (M _⊙)
(1)	(2)	(3)	(4)	(5)	(6)	(7)	(8)	(9)	(10)	(11)	(12)	(13)	(14)	(15)	(16)	(17)	(18)	(19)	(20)
N3319	SB(rs)cd	14.1	L	87.4	-19.43 ± 0.74	-20.56	9.49 ± 0.30	9.94	-	<34.8	0.47	0.007	0.05	U	-	BS	9.7	9.9	14.0
N3344	(R)SAB(r)	12.3	H II	73.6	-17.83 ± 0.79	-20.82	9.25 ± 0.32	10.45	-	<34.1	0.07	0.004	0.56	U	-	BS	9.7	9.3	13.1
N3348	E0	41.8	ALG	236.4	-21.31 ± 0.24	-21.31	11.39 ± 0.11	11.39	-	36.6	0.07	0.002	0.04	I	C	-	9.7	10.1	12.5
N3414	S0pec	24.4	L	236.8	-20.59 ± 0.15	-20.77	11.33 ± 0.07	11.39	8.39 ^{+0.07} _{-0.07}	36.2	0.20	0.002	0.64	I	C	RS	10.0	9.9	13.0
N3448	I0	21.0	H II	50.7	-20.54 ± 0.26	-21.39	10.29 ± 0.11	10.63	-	35.5	0.37	-0.016	0.04	I	A	BS	9.8	9.7	14.0
N3486	SAB(r)c	14.1	S	65.0	-18.58 ± 0.47	-20.27	9.33 ± 0.19	10.01	-	<34.3	0.14	-0.002	0.37	U	-	BS	9.3	9.4	13.2
N3504	(R)SAB(s)	26.2	H II	119.3	-20.43 ± 0.38	-20.90	10.62 ± 0.16	10.81	-	37.3	0.17	0.005	0.44	I	A	BS	9.8	9.8	13.2
N3516	(R)SB00	37.5	S	181.0	-21.01 ± 0.39	-22.36	11.05 ± 0.16	11.59	7.37 ^{+0.16} _{-0.16}	36.8	0.17	-0.003	0.47	I	C	-	9.8	10.1	13.5
N3600	Sa?	13.2	H II	49.8	-16.23 ± 0.56	-17.57	9.22 ± 0.23	9.76	-	<34.7	0.56	-0.010	0.05	U	-	BS	10.0	9.8	12.3
N3610	E5?	25.6	ALG	161.2	-20.79 ± 0.64	-20.88	10.55 ± 0.26	10.59	-	<35.6	0.33	0.003	0.38	U	-	-	10.0	10.8	14.0
N3613	E6	31.7	ALG	220.1	-21.39 ± 0.34	-21.99	10.93 ± 0.14	11.17	-	<35.7	0.27	-0.002	0.09	U	-	-	9.8	10.2	14.0
N3631	SA(s)c	19.2	H II	43.9	-20.13 ± 0.22	-20.32	10.15 ± 0.10	10.23	-	<35.2	0.05	0.002	0.27	U	-	BS	10.1	10.4	13.1
N3642	SA(r)bc?	24.9	L	85.0	-18.85 ± 0.03	-20.63	9.41 ± 0.05	10.12	7.48 ^{+0.04} _{-0.04}	<35.5	0.14	0.000	0.61	U	-	BS	10.0	10.7	14.0
N3665	SA00(s)	32.1	H II/RL	236.8	-24.81 ± 0.69	-25.12	12.50 ± 0.28	12.60	8.73 ^{+0.09} _{-0.09}	36.8	0.23	0.001	-0.02	I	B	-	9.0	10.4	12.3
N3675	SA(s)b	13.8	L	108.0	-15.54 ± 0.71	-20.93	9.42 ± 0.29	11.57	7.31 ^{+0.29} _{-0.29}	35.0	0.30	-0.022	0.61	I	A	-	10.2	9.9	13.5
N3718	SB(s)a	16.9	L/RL	158.1	-19.62 ± 0.31	-20.15	10.47 ± 0.13	10.68	-	36.8	0.28	-0.020	0.18	I	A	-	10.7	10.8	13.1
N3729	SB(r)ape	17.8	H II	76.2	-16.22 ± 0.37	-18.86	8.88 ± 0.15	9.94	-	35.8	0.24	0.006	0.21	I	A	BS	10.6	10.7	13.1
N3756	SAB(rs)b	21.4	H II	47.6	-17.81 ± 0.78	-20.57	9.25 ± 0.32	10.35	-	<35.3	0.19	0.015	0.33	U	-	BS	10.7	10.6	13.9
N3838	SA0a?	21.0	ALG	141.4	-18.69 ± 0.39	-22.11	10.00 ± 0.16	11.36	-	35.4	0.36	0.019	0.74	unl	-	-	10.4	10.5	12.7
N3884	SA(r)0/a	107.0	L	208.3	-21.92 ± 0.29	-23.11	11.55 ± 0.13	12.03	-	37.8	0.15	0.005	0.43	I	A	-	10.9	10.9	14.9
N3898	SA(s)ab	19.2	L	206.5	-20.25 ± 0.59	-20.59	11.00 ± 0.24	11.13	-	35.8	0.28	0.004	0.44	I	A	BS	10.5	10.3	11.7
N3900	SA0+(r)	30.2	ALG	139.2	-20.83 ± 0.04	-21.61	10.74 ± 0.07	11.05	-	<35.6	0.33	0.006	0.72	U	-	BS	9.0	8.9	13.0
N3945	(R)SB0+(rs)	20.3	L	191.5	-17.68 ± 0.38	-20.20	10.03 ± 0.16	11.04	6.96 ^{+0.47} _{-0.47}	35.8	0.20	0.018	0.53	I	C	-	10.1	10.5	13.4
N3949	SA(s)bc?	14.5	H II	82.0	-19.92 ± 0.29	-20.43	9.62 ± 0.13	9.82	-	<35.0	0.35	-0.004	0.06	U	-	BS	11.0	10.8	15.2
N3982	SAB(r)b?	18.3	S	73.0	-19.40 ± 0.34	-20.77	8.66 ± 0.15	9.21	7.01 ^{+0.26} _{-0.26}	36.2	0.15	-0.005	0.27	I	A	-	10.8	10.8	11.7
N3992	SB(rs)bc	17.6	L	148.4	-18.50 ± 0.39	-21.11	9.82 ± 0.16	10.86	7.57 ^{+0.28} _{-0.28}	<35.1	0.19	0.004	0.54	U	-	-	10.7	10.8	11.7
N3998	SA00(r)	17.4	L/RL	304.6	-19.27 ± 0.47	-20.04	10.85 ± 0.19	11.16	9.02 ^{+0.05} _{-0.05}	38.0	0.12	0.003	0.36	I	A	-	10.8	10.9	11.7
N4026	S0edge-on	16.9	L	177.2	-22.37 ± 0.41	-23.11	11.32 ± 0.17	11.61	8.36 ^{+0.12} _{-0.12}	<35.1	0.28	0.017	0.43	U	-	-	11.1	11.1	13.6
N4036	S0-	21.7	L	215.1	-19.23 ± 0.08	-21.45	10.50 ± 0.09	11.39	7.95 ^{+0.36} _{-0.36}	36.0	0.28	0.007	0.15	I	C	-	10.1	10.5	13.4
N4041	SA(rs)bc	19.5	H II	95.0	-19.32 ± 0.11	-20.14	9.85 ± 0.09	10.18	6.00 ^{+0.20} _{-0.20}	35.5	0.34	-0.006	0.01	I	E	BS	10.4	10.5	12.7
N4062	SA(s)c	14.9	H II	93.2	-15.35 ± 0.22	-20.31	8.38 ± 0.10	10.36	-	<34.6	0.32	0.004	0.00	U	-	BS	10.2	9.9	13.3
N4096	SAB(rs)c	11.1	H II	79.5	-17.49 ± 0.49	-20.94	8.99 ± 0.20	10.37	-	<34.5	0.36	-0.006	0.04	U	-	-	10.9	11.0	15.2
N4102	SAB(s)b?	14.7	H II	174.3	-18.30 ± 0.44	-18.77	10.60 ± 0.21	10.79	-	35.9	0.13	0.008	0.36	I	E	BS	11.1	11.1	13.6
N4125	E6pec	21.0	L	226.7	-21.14 ± 0.23	-21.14	11.26 ± 0.10	11.26	-	<35.4	0.24	0.006	0.28	U	-	-	10.0	10.2	12.7
N4138	SA0+(r)	16.0	L	120.9	-20.01 ± 0.39	-20.58	10.56 ± 0.16	10.79	-	<35.3	0.37	0.003	0.41	U	-	BS	10.5	10.8	14.5
N4143	SAB00(s)	16.9	L	204.9	-20.45 ± 0.34	-21.22	10.92 ± 0.14	11.23	7.98 ^{+0.37} _{-0.37}	36.1	0.16	0.005	0.52	I	B	-	10.2	10.5	14.5

Table A1 – continued

Galaxy	Type	<i>D</i> (Mpc)	Class	σ (km s ⁻¹)	<i>M_V</i> (mag)	<i>M_{V, galaxy}</i> (mag)	<i>logM_*, bulge</i> (M _⊙)	<i>logM_*, galaxy</i> (M _⊙)	<i>log M_{BH}</i> (M _⊙)	<i>logL_{R, core}</i> (erg s ⁻¹)	ϵ	Med (<i>B₄</i>)	γ	Det	AGN Sequence	<i>log v₁₀</i> (L _⊙ Mpc ⁻²)	<i>log v₃</i> (L _⊙ Mpc ⁻²)	<i>log M_{halo}</i> (M _⊙)	
(1)	(2)	(3)	(4)	(5)	(6)	(7)	(8)	(9)	(10)	(11)	(12)	(13)	(14)	(15)	(16)	(17)	(18)	(19)	(20)
N4144	SAB(s)cd	6.8	H II	64.3	-10.08 ± 1.10	-19.38	5.54 ± 0.44	9.26	-	<34.0	0.46	0.017	0.57	U	-	BS	9.9	10.5	15.2
N4150	SA00(r)	7.1	L	87.0	-15.80 ± 0.14	-17.77	9.03 ± 0.08	9.81	5.68 ^{+0.44} _{-0.44}	<34.6	0.33	-0.008	0.07	U	-	-	9.4	9.6	12.7
N4151	(R')SAB(17.8	S	97.0	-19.22 ± 0.84	-20.85	10.14 ± 0.34	10.79	7.76 ^{+0.08} _{-0.08}	37.8	0.11	0.000	0.81	I	C	-	10.0	10.0	14.1
N4183 [†]	SA(s)cd?	16.6	H II	34.4	-	-20.54	-	9.84	-	<35.2	-	-	-	U	-	BS	9.3	10.2	14.5
N4203	SAB0 ⁻	19.5	L	167.0	-19.59 ± 0.27	-20.44	10.90 ± 0.11	11.24	-	36.1	0.07	0.005	0.36	I	A	BS	9.9	9.3	13.9
N4217	Sb-edge on	17.7	H II	91.3	-19.88 ± 0.18	-21.16	10.60 ± 0.08	11.24	-	35.2	0.58	0.009	0.01	I	C	BS	10.3	9.9	13.8
N4220	SA0 ⁺ (r)	16.0	L	105.5	-18.25 ± 0.14	-19.96	10.06 ± 0.08	10.75	-	35.2	0.44	-0.008	0.38	I	A	BS	10.6	10.5	13.8
N4242	SAB(s)dm	10.3	H II	-	-11.74 ± 0.19	-18.80	6.68 ± 0.09	9.50	-	34.4	0.71	-0.012	1.68	unl	-	BS	10.7	10.7	13.8
N4244	SA(s)cd?	7.1	H II	36.8	-14.79 ± 0.09	-21.99	7.65 ± 0.06	10.53	-	33.8	0.40	0.018	0.78	I	A	BS	10.0	9.9	14.1
N4245	SB0a?(r)	16.7	H II	82.7	-19.30 ± 0.33	-20.18	10.20 ± 0.14	10.57	7.25 ^{+0.48} _{-0.48}	<34.6	0.11	-0.014	0.16	U	-	BS	10.5	11.6	13.2
N4258	SAB(s)bc	9.4	S	148.0	-20.03 ± 0.31	-21.69	10.85 ± 0.13	11.53	7.69 ^{+0.03} _{-0.03}	34.9	0.26	0.011	0.39	I	A	BS	10.0	10.8	13.8
N4274	(R)SB(r)	17.4	L	96.6	-17.93 ± 0.16	-20.10	9.58 ± 0.10	10.44	-	<34.6	0.45	0.004	0.05	U	-	BS	10.3	11.2	13.2
N4278	E1-2	15.6	L/R/L	237.0	-20.91 ± 0.27	-20.91	11.00 ± 0.12	11.00	7.98 ^{+0.27} _{-0.27}	37.6	0.16	0.000	0.22	I	A	BS	9.8	10.7	13.2
N4291	E	25.5	ALG	293.0	-20.71 ± 0.19	-20.71	10.90 ± 0.09	10.90	8.97 ^{+0.16} _{-0.16}	<35.5	0.24	-0.006	0.10	U	-	-	10.0	10.6	13.3
N4314	SB(rs)a	17.8	L	117.0	-19.74 ± 0.22	-20.69	10.74 ± 0.10	11.12	6.97 ^{+0.30} _{-0.30}	<34.7	0.19	-0.005	0.16	U	-	BS	9.5	10.9	13.2
N4414	SA(rs)c?	14.2	L	117.0	-19.14 ± 0.79	-20.11	10.39 ± 0.32	10.77	-	<34.7	0.30	0.004	0.42	U	-	BS	10.5	10.7	13.9
N4448	SB(r)ab	13.5	H II	119.8	-18.89 ± 0.02	-19.38	10.56 ± 0.05	10.76	-	<34.5	0.18	0.012	0.19	U	-	BS	10.0	10.7	13.2
N4449	IBm	6.1	H II	17.8	-16.61 ± 0.54	-20.10	8.37 ± 0.22	9.76	-	<33.6	0.26	-0.010	0.46	U	-	-	9.9	10.6	14.1
N4485	IB(s)mpe	10.3	H II	52.2	-17.58 ± 0.32	-18.09	8.72 ± 0.14	8.92	-	<34.3	0.38	-0.018	0.00	U	-	BS	10.7	10.7	14.5
N4490	SB(s)dpe	11.4	H II	45.1	-20.05 ± 0.14	-21.94	9.45 ± 0.07	10.20	-	<34.5	0.33	0.003	0.00	U	-	-	10.3	9.9	14.5
N4559	SAB(rs)c	15.6	H II	49.2	-16.16 ± 0.40	-19.64	8.06 ± 0.15	9.45	-	<34.3	0.13	0.035	0.61	U	-	-	10.5	10.0	14.0
N4565	SA(s)b?e	21.8	S	136.0	-21.71 ± 0.25	-23.62	11.16 ± 0.11	11.93	-	35.2	0.36	-0.002	0.69	I	A	BS	9.4	10.0	14.0
N4589	E2	29.2	L/R/L	224.3	-21.04 ± 0.25	-21.04	11.02 ± 0.11	11.02	-	37.5	0.34	0.003	0.30	I	C	-	9.7	10.0	14.0
N4605	SB(s)epc	3.7	H II	26.1	-17.72 ± 0.29	-18.48	8.99 ± 0.12	9.29	-	<33.8	0.49	0.050	0.00	U	-	BS	<9.7	<9.5	13.2
N4648	E3	21.0	ALG	224.5	-18.66 ± 0.39	-19.58	10.05 ± 0.16	10.42	-	<35.5	0.16	-0.001	0.53	U	-	-	9.5	10.3	14.0
N4656 [†]	SB(s)mpe	13.0	H II	70.4	-	-21.47	-	9.77	-	<34.3	-	-	-	U	-	-	10.5	10.5	14.0
N4736	(R)SA(r)	7.6	L	112.0	-19.78 ± 0.77	-21.35	10.50 ± 0.12	11.13	7.00 ^{+0.12} _{-0.12}	34.8	0.11	-0.007	0.01	I	A	BS	10.4	10.7	13.1
N4750	(R)SA(rs)	24.1	L	136.0	-19.57 ± 0.56	-20.89	10.23 ± 0.23	10.76	-	35.8	0.23	0.010	0.37	I	A	BS	9.7	10.1	13.5
N4800	SA(rs)b	15.6	H II	111.0	-19.24 ± 0.26	-19.41	10.36 ± 0.11	10.41	7.12 ^{+0.53} _{-0.53}	<34.9	0.18	-0.003	0.04	U	-	BS	10.0	9.3	13.6
N4826	(R)SA(rs)	10.0	L	96.0	-19.63 ± 0.33	-21.45	10.50 ± 0.14	11.23	6.33 ^{+0.13} _{-0.13}	33.9	0.28	-0.007	0.25	I	A	BS	9.9	9.5	13.5
N4914	cD	70.8	ALG	224.7	-20.94 ± 0.25	-20.94	11.60 ± 0.11	11.60	-	<36.2	0.31	0.006	-0.01	U	-	-	9.9	10.1	13.1
N5005	SAB(rs)b	16.8	L	172.0	-21.30 ± 0.64	-21.47	11.03 ± 0.26	11.10	8.33 ^{+0.23} _{-0.23}	36.3	0.45	-0.005	0.21	I	D	BS	9.5	10.3	12.7
N5033	SA(s)c	15.8	L	151.0	-20.00 ± 0.44	-22.31	9.90 ± 0.18	10.83	-	36.0	0.31	-0.002	0.40	I	A	BS	9.6	10.8	12.7
N5055	SA(rs)bc	9.9	L	117.0	-17.70 ± 0.33	-21.56	9.51 ± 0.15	11.05	8.97 ^{+0.11} _{-0.11}	<34.4	0.24	0.001	0.06	U	-	BS	10.2	10.2	14.1
N5112 [†]	SB(rs)cd	17.0	H II	60.8	-	-19.51	-	9.51	-	<35.4	-	-	-	U	-	-	9.6	10.8	13.8
N5204	SA(s)m	4.6	H II	39.9	-17.75 ± 0.28	-18.31	8.67 ± 0.12	8.89	-	<34.1	0.45	-0.011	0.01	U	-	BS	<9.7	>10.0	14.2
N5273	SA00(s)	18.6	S	71.0	-18.86 ± 0.09	-20.24	10.05 ± 0.06	10.60	6.69 ^{+0.27} _{-0.27}	35.3	0.11	0.000	0.55	U	-	RS	9.0	9.2	14.1
N5308	S0 ⁻ -edge on	30.1	ALG	249.0	-19.99 ± 0.49	-21.08	10.84 ± 0.20	11.27	-	<35.8	0.46	0.009	0.12	U	-	-	10.4	10.7	13.7

Table A1 – continued

Galaxy	Type	D (Mpc)	Class	σ (km s ⁻¹)	M_V bulge (mag)	M_V galaxy (mag)	$\log M_{*}$ bulge (M_{\odot})	$\log M_{*}$ galaxy (M_{\odot})	$\log M_{\text{BH}}$ (M_{\odot})	$\log L_{\text{R,core}}$ (erg s ⁻¹)	ϵ	Med (B_4)	γ	Det	AGN Sequence	$\log \nu_{10}$ (L_{\odot} Mpc ⁻²)	$\log \nu_3$ (L_{\odot} Mpc ⁻²)	$\log M_{\text{halo}}$ (M_{\odot})	
(1)	(2)	(3)	(4)	(5)	(6)	(7)	(8)	(9)	(10)	(11)	(12)	(13)	(14)	(15)	(16)	(17)	(18)	(19)	(20)
N5322	E3-4	27.0	L/RL	230.0	-21.77 ± 0.24	-22.10	11.30 ± 0.11	11.50	-	37.0	0.32	-0.004	0.17	I	B	-	9.8	10.7	13.7
N5353	S0edge-on	36.1	L/RL	286.4	-18.04 ± 0.23	-19.72	10.41 ± 0.10	11.10	-	37.6	0.37	-0.011	0.11	I	A	RS	11.4	12.3	13.6
N5354	S0edge-on	39.8	L/RL	217.4	-20.51 ± 0.18	-21.34	10.88 ± 0.08	11.21	-	36.9	0.17	-0.005	0.26	I	A	RS	11.3	10.8	13.6
N5377	(R)SB(s)	28.0	L	169.7	-20.99 ± 0.31	-21.77	11.18 ± 0.15	11.49	-	35.7	0.23	-0.008	0.22	I	C	BS	9.9	10.0	14.4
N5448	(R)SAB(r)	31.1	L	124.5	-19.77 ± 0.22	-21.84	9.48 ± 0.10	10.93	-	35.7	0.32	-0.008	0.18	I	C	BS	10.0	10.0	14.4
N5457	SAB(rs)bc	5.2	H II	23.6	-15.72 ± 0.81	-17.42	8.28 ± 0.33	8.96	6.41 ^{+0.08} _{-0.08}	<34.3	0.31	0.002	0.57	U	-	BS	<9.8	<9.6	13.7
N5474	SA(s)cd pec	5.7	H II	29.0	-16.04 ± 0.39	-17.58	8.39 ± 0.16	9.01	-	<34.4	0.29	-0.054	0.00	U	-	BS	9.8	9.9	11.7
N5548	(R')SA0a	77.6	S	291.0	-21.45 ± 0.42	-22.31	10.76 ± 0.17	11.10	7.72 ^{+0.13} _{-0.13}	37.0	0.07	-0.005	0.33	I	B	-	9.7	10.7	13.1
N5557	E1	46.4	ALG	259.0	-22.39 ± 0.32	-22.39	11.40 ± 0.14	11.40	-	<35.0	0.13	0.000	0.19	U	-	-	9.6	10.8	13.4
N5585	SAB(s)d	5.6	H II	42.0	-14.11 ± 0.33	-17.19	7.35 ± 0.13	8.58	-	<34.5	0.24	0.007	0.01	U	-	BS	9.6	9.8	12.8
N5631	SA00(s)	29.3	L	168.1	-20.84 ± 0.19	-20.90	11.37 ± 0.09	11.40	-	<35.9	0.12	0.000	-0.01	U	-	RS	10.1	10.0	12.8
N5866	SA0+edge	11.8	L/RL	169.1	-19.58 ± 0.32	-20.57	10.39 ± 0.14	10.79	-	36.5	0.33	-0.001	0.08	I	D	-	9.4	10.3	12.9
N5879	SA(rs)bc	12.0	L	73.9	-18.20 ± 0.95	-20.29	9.38 ± 0.38	10.21	6.67 ^{+0.28} _{-0.28}	35.3	0.39	0.008	0.40	I	A	BS	9.2	10.7	12.4
N5907†	SA(s)c?e	10.4	H II	120.2	-	-22.12	-	11.16	-	35.0	-	-	-	unl	-	BS	9.4	10.5	12.4
N5982	E3	44.0	ALG	239.4	-22.08 ± 0.27	-22.08	11.37 ± 0.11	11.37	-	<35.8	0.28	0.003	0.09	U	-	-	8.9	10.3	13.7
N5985	SAB(r)b	36.7	L	157.6	-21.22 ± 0.34	-22.70	10.78 ± 0.14	11.37	-	35.8	0.27	0.013	0.32	I	D	BS	8.9	9.7	13.7
N6140	SB(s)cd	12.9	H II	49.4	-17.18 ± 0.19	-18.36	8.83 ± 0.09	9.30	-	<35.2	0.47	0.000	0.00	U	-	BS	9.6	9.5	14.4
N6207	SA(s)c	12.3	H II	92.1	-17.36 ± 0.51	-20.20	8.79 ± 0.21	9.92	-	<35.2	0.28	0.009	0.10	U	-	-	8.4	9.2	14.2
N6217	(R)SB(rs)	19.1	H II	70.3	-18.40 ± 0.71	-19.85	9.48 ± 0.29	10.06	-	35.7	0.18	-0.005	0.02	I	A	-	9.7	9.4	12.4
N6340	SA0a(s)	16.6	L	143.9	-19.78 ± 0.39	-20.20	10.73 ± 0.16	10.90	-	35.5	0.05	0.001	0.60	I	A	RS	9.8	10.6	12.8
N6412	SA(s)c	18.1	H II	49.9	-17.81 ± 0.19	-19.35	9.03 ± 0.09	9.64	-	<35.4	0.34	0.030	0.10	U	-	BS	10.1	10.0	13.2
N6482	E?	55.7	L	310.4	-22.30 ± 0.19	-22.53	11.25 ± 0.09	11.34	-	36.4	0.17	0.006	0.07	I	A	-	8.7	8.8	13.1
N6503	SA(s)cd	4.9	L	46.0	-13.75 ± 0.37	-19.20	7.70 ± 0.15	9.88	6.27 ^{+0.11} _{-0.11}	<34.3	0.31	-0.001	0.45	U	-	-	<9.1	<9.4	13.9
N6654	(R')SB0a	25.0	ALG	172.2	-18.61 ± 0.04	-20.19	10.45 ± 0.05	11.08	-	<35.6	0.12	0.001	0.38	U	-	-	8.5	9.1	13.2
N6946	SAB(rs)c	5.0	H II	55.8	-16.38 ± 0.31	-18.79	8.27 ± 0.13	9.25	-	34.4	0.32	-0.019	0.12	I	E	-	<8.2	<8.7	12.9
N6951	SAB(rs)b	18.2	L	127.8	-20.25 ± 0.55	-21.51	10.33 ± 0.22	10.85	6.99 ^{+0.20} _{-0.20}	35.4	0.15	0.001	0.27	I	C	-	9.3	8.8	13.1
N7217	(R)SA(r)ab	9.0	L	141.4	-19.55 ± 0.18	-19.86	10.60 ± 0.08	10.73	-	35.1	0.08	0.001	0.22	I	C	-	9.7	10.2	13.6
N7331	SA(s)b	7.0	L	137.2	-17.62 ± 0.47	-19.29	10.25 ± 0.19	10.92	7.78 ^{+0.18} _{-0.18}	<35.0	0.34	0.020	0.44	U	-	-	9.3	9.5	14.1
N7457	SA0 ⁻ (rs)	7.2	ALG	69.4	-16.84 ± 0.72	-18.11	9.58 ± 0.30	10.09	6.71 ^{+0.30} _{-0.30}	<34.9	0.24	0.003	0.48	U	-	-	9.5	10.2	13.6
N7640	SB(s)c	0.9	H II	48.1	-14.45 ± 0.33	-16.09	7.21 ± 0.14	7.86	-	<34.5	0.52	0.011	0.01	U	-	-	<8.4	<8.0	13.8
N7741	SB(s)cd	5.8	H II	29.4	-15.33 ± 0.37	-16.00	7.87 ± 0.15	8.13	-	<34.7	0.77	-0.005	0.00	U	-	BS	9.2	9.2	14.6
error	-	-	-	-	-	0.33	-	0.17 dex	-	1.0 dex	20 per cent	35 per cent	10 per cent	-	-	-	0.6 dex	0.6 dex	0.5 dex

Note. (1) galaxy name. (2) morphological classification from RC3 (de Vaucouleurs et al. 1991). (3) distance (D) are primarily from the NASA/IPAC Extragalactic Data base (NED; <http://nedwww.ipac.caltech.edu>), other sources are Karachentsev et al. (2004, k) and Bonanos et al. (2006, b). (4) optical spectral class from Baldi et al. (2021a); H II, L = LINER, S = Seyfert, and ALG = Absorption Line Galaxy. Radio-loud galaxies (RL) are shown (Section 3.4). (5) the central velocity dispersion (σ) from Ho et al. (2009). (6)–(7) V-band bulge and galaxy magnitudes calculated by integrating the best-fitting Sérsic, Gaussian or core-Sérsic functions. (8)–(9) logarithm of the stellar masses of the bulge and galaxy. (10) logarithm of the SMBH mass (M_{BH}) for galaxies with measured M_{BH} from van den Bosch (2016), except for NGC 205 which is from Nguyen et al. (2019). The BH masses are adjusted here to our distance. (11) logarithm of the radio core luminosity ($L_{\text{R,core}}$). (12) average ellipticity of the galaxy inside R_e , after omitting the PSF-affected region (ϵ). (13) median of the isophote shape parameter inside R_e (Med (B_1)). (14) negative, inner logarithmic slope of the bulge light profile. (15) radio detection of the galaxies based on Baldi et al. (2021a) and following their nomenclature '†' = detected and core identified; 'un†' = detected but core unidentified; 'U' = undetected; '†+un†?' = detected and core identified having additional unknown source(s) in the FOV. Col. (16) radio morphologies following Baldi et al. (2021a); A = core/core-jet; B = one-sided jet; C = triple; D = double-lobed; E = jet+complex. (17) sample galaxies with GALEX NUV, FUV band and *Spitzer* 3.6 μm data in Bouquin et al. (2018) separated into 'red sequence' (RS), 'blue sequence' (BS) and 'green valley' (GV) based on the (FUV–NUV)–(NUV – [3.6]) colour–colour diagram (Bouquin et al. 2018, their eqs. 1–3). (18)–(19) luminosity surface densities of a galaxy inside a cylinder containing 10 and 3 nearest neighbours, ν_{10} and ν_3 . Note that for (23/173) sample galaxies at distances $D \lesssim 5$ Mpc our values of ν_{10} and ν_3 are upper limits. (20) halo mass (M_{halo}) based on the HDC catalogue from Crook et al. (2007), see the text for details.

in common between our sample and the ATLAS^{3D} parent sample. Fig. A3(a) shows how their values of ρ_{10} compare with ours. Although the agreement is good for the bulk (75 per cent) of the overlapping galaxies, our ρ_{10} values are larger by more than a factor of 2 for the remaining 25 per cent. We attribute this discrepancy to differences in the data base and filter (used to identify the nearest neighbours and measure their magnitudes) adopted by us and Cappellari et al. (2011). On average we have identified more neighbours over a given projected radius than Cappellari et al. (2011). As such, their median value of $R_{10} = 3.8$ Mpc is larger than ours $R_{10} \sim 2.9$ Mpc. While we do not find a one-to-one relation between the ρ_{10} values from the two studies, Fig. A3(b) reveals a tight correlation between the K -band luminosity surface density ν_{10} (Cappellari et al. 2011) and our B -band ν_{10} for the 91 overlapping galaxies ($r_s \sim 0.83$, $P \sim 10^{-25}$).

Finally, because galaxy morphology is well known to depend on the local environmental density through the so-called morphology–density relation (Dressler 1980), we go on and check if we can recover this relation. Having expanded our sample of galaxies by adding 32 massive elliptical galaxies from Dullo & Graham (2014); Dullo (2019), in Fig. A4 we display the fraction of elliptical, S0

and spiral+Irr galaxies as a function of ν_{10} for 205 (=173+32) nearby galaxies. We reproduce the traditional morphology–density relation reasonably well, see Cappellari et al. (2011, their fig. 9), although we caution that our sample, which is representative of the statistically complete full LeMMINGs sample, suffers from incompleteness (see Dullo et al. 2023). The trend in Fig. A4 is that the fraction of late-type (spiral+Irr) galaxies declines with increasing local environmental density, and correspondingly the early-type (E+S0) fraction increases.

DATA TABLES

Table A1 provides global and central properties of the sample galaxies including distance, morphological classification, velocity dispersion, bulge, and galaxy stellar masses, optical and radio luminosities, ellipticity, isophote shape parameter and logarithmic slope of the inner light profiles of our sample galaxies.

This paper has been typeset from a $\text{\TeX}/\text{\LaTeX}$ file prepared by the author.